Dynamics of the Galactic Bulge using Planetary Nebulæ

by

Sylvie F. Beaulieu

A thesis submitted for the degree of

Doctor of Philosophy
of the Australian National University

Mount Stromlo and Siding Spring Observatories
Institute of Advanced Studies
Australian National University
Canberra, Australia

May 1996

To my family and friends.

Thesis supervisor: Professor Kenneth C. Freeman

Thesis advisors: Professor Michael A. Dopita
Dr. Agris J. Kalnajs

Declaration of Authorship

The work in this thesis is that of the candidate alone, except where indicated below, and where indicated in the main text.

Chapter 5: The *Best Parameters Search* code was developed by Prasenjit Saha.

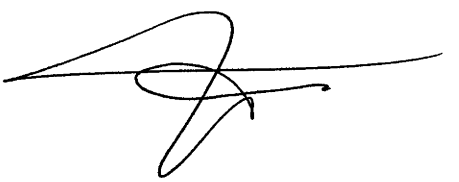

Sylvie F. Beaulieu
3rd May 1996

Acknowledgements

I wish to acknowledge funding from The Australian Government through an Australian National University Scholarship and an Overseas Postgraduate Research Scholarship.

I am indebted to MSSSO for giving me the opportunity to conduct this research and for the use of their excellent facilities.

I also wish to thank the Anglo-Australian Observatory for lending us the LDSS.

I am grateful to Jerry Sellwood, Roger Fux, Agris Kalnajs and HongSheng Zhao for providing me with their N-body simulations.

I wish to thank the team who helped publish the Strasbourg-ESO Catalogue of Galactic Planetary Nebulæ (Acker *et al.*, 1992). This Catalogue has been of great help throughout this thesis.

To my supervisor, Ken Freeman, I am most grateful for his patience, insights, advice and good humour. But most of all, for his friendship, something I will treasure all my life. Thank you very much Ken!

To my two advisers, Mike Dopita, for sharing his knowledge on Planetary Nebulæ and on good wine, and Agris Kalnajs, for being very patient with me. I have learned more programming from Agris in three months that I will probably every learn in the remaining of my career.

I wish to thank Dr Gilles Fontaine for giving me my first astronomy summer job as an undergraduate student. I am indebted to Dr Claude Carignan who, for so many years, has not only been a great teacher and mentor but also a good friend.

I wish to thank Jayanne English for all her help in my transition from TEX to LATEX and for providing some templates which helped put together this thesis. Thank you also to Maartje Sevenster for interesting discussions about her project on the OH/IR stars survey.

I am grateful to my family, and most of all, to my mother, for her love, care and regular phone calls.

I would like to thank my very best friends, Amy, Diane, Doris, Joanne, Marianne and Véronique for their friendship, encouragement and correspondences during my stay in Australia.

Un gros merci à la gang du Club des Astronomes Amateurs de Verdun, et tout spécialement à Monsieur Lefebvre, notre directeur. Vos encouragements et votre enthousiasme ont toujours été une grande source d'énergie.

I wish to thank the many good friends I have made in Australia over the last four years: the pass and present students and postdocs, my various housemates of house 16, Patricia Dopita, Margaret Freeman, Magda Arnaboldi, Ariane Lançon, Thelma and Clive, Simon Chan (for his driving lessons and famous Friday dinners with the residents of Mount Stromlo) and my two tennis partners Claudia Schmid

and Tracey Parrish. You have all made me feel welcomed and at home.

A big cheer goes to the various pass and present members of the ACT/MSO volunteer bush fire team with whom I have been a member since 1992. I will remember the chopper ride for a long time... Keep up the good work!

And how can I forget to thank the only permanent resident of house 16, Octave, who clearly prefer octopus to Whiskas. I leave you now to the good care of Sung, Martin and Ben.

I am indebted to the staff of Mount Stromlo and Siding Spring Observatories. It is not possible to name everyone here who have contributed directly or indirectly to the success of this thesis but I wish to acknowledge especially the technicians from the workshops, the staff at the SSO lodge, who always maintain a fine place and prepare great dinners, Keith Smith from the photolab and the staff at the ANU Coombs Photolab.

My thanks also goes to Don Matheson, Vince Ford and Bill Roberts for giving up their 1.0m observing run of the 18-22 June 1993, and to Stéphane Vennes (Berkeley, EUVE) for giving up one night at the 74-inch on 22 June 1995. I am also grateful to Peter Conroy for providing the diagram of the LDSS Optical Layout (Figure 2.1).

And finally, this long list of acknowledgements would not be complete without a warm thank you to the Organizers and Artists of the Australian Opera for their superb work and performances. I have spent many enjoyable evenings at the Opera House in Sydney.

Abstract

We present the results of a deep and uniform narrow-band H_α imaging survey for planetary nebulæ (PNe) in the southern galactic bulge. The goal of this survey is to obtain a sample of bulge tracers which we will use to study the dynamics of the Milky Way bulge.

Bulges of spiral galaxies have a range of shapes, from the peanut and X-shaped systems through to spheroidal. The boxiness vs spheroidal structure of bulges is roughly understood in terms of orbital properties but not in terms of origin. Do they form during galaxy collapse or through later accretion events that occur in the evolution of disks?

The Milky Way has an excellent example of a box-shaped bulge. The galactic bulge thus provides a unique opportunity to investigate the detailed pattern of rotation and velocity dispersion in a boxy galactic bulge.

To understand the history and dynamics of our own galactic bulge, we need to answer important specific observational questions such as: What is the pattern of rotation and velocity dispersion in the galactic bulge ? Is the bulge of the Galaxy actually a stellar bar?

Evidence for a bar at the center of the Milky Way triggered a renewed enthusiasm for dynamical modelling of the galactic bar-bulge. Our goal is to compare the kinematics of a sample of tracers widely distributed over the bulge with the corresponding kinematics for a range of N-body models of the inner Galaxy. Three of these models are barred systems arising from the instabilities of a stellar disk (Sellwood, Fux and Kalnajs), and one is a Schwarzschild system constructed to represent the 3D distribution of the COBE/DIRBE near-IR light and then evolved as an N-body system for a few dynamical times (Zhao).

We have chosen PNe as the tracers because they are less affected by metallicity bias than most other tracers and, they are strong emitters in H_α - this make their velocities easy to measure. We have chosen to survey a region of the southern galactic bulge: $l = \pm 20°$ and $b = -5°$ to $-10°$, because of its lower extinction relative to the northern bulge. In our survey, we have found 56 new PNe and have re-discovered 45 known PNe. We have thus doubled the number of known PNe in our surveyed region. We have measured the radial velocities of this uniformly selected sample which is the basis of the comparison with the dynamical models. We have also re-measured radial velocities for a subset of 317 PNe from the Acker *al.* (1992) Catalogue, in the more extended region $l = \pm 30°$ and $b = \pm(3.3°$ and $15°)$: this larger sample is also being used for some dynamical comparisons, although the discovery process for this larger sample is much less homogeneous.

Using the COBE/DIRBE 1.25, 2.2 and 3.5μm images, we show that there is no significant difference between the longitude distribution of the PNe and the COBE light in the zone of our deep survey. Also, we find that the extinction in our surveyed fields is not severe and that its distribution is fairly uniform.

For the comparison of our data with the models, we use a new technique

developed by Prasenjit Saha. The procedure finds the best parameters of each model ie the solar orbit radius R_o in model units, the orientation angle ϕ in degrees, the velocity scale (in km s^{-1} per model unit), and the solar tangential velocity (in km s^{-1}) which best fit the data. The longitude dependence of mean velocity $< V >$ and velocity dispersion σ derived from each model using the best fitting parameters show that Sellwood's and Zhao's models fit the $< V >(l)$ relation well, but are a little cold in σ, while Fux's and Kalnajs's models fit well in σ but rotate a little slowly. But, on the basis of Saha's technique, all four models give an acceptable fit to the data.

Contents

List of Figures

List of Tables

Chapter 1

Introduction

A spiral galaxy consists of a relatively flattened stellar disk in nearly circular rotation and, in most systems, a central bulge. It is estimated that about 30 % of these galaxies also show a central bar; however the real fraction of barred galaxies is probably significantly higher because some apparently normal spirals show a bar feature in the near-IR that was not visible in their optical images (eg Sellwood and Wilkinson, 1993). In addition, barred galaxies often show a lens and/or ring around the bar. The flattened disks contain objects of all ages, from the interstellar gas and very young stars to the old disk stars which in our Galaxy are almost as old as the globular clusters. The bulges appear to be made up mainly of old stars.

The disks of most disk galaxies are relatively thin, with the ratio of their radial to vertical scale heights mostly in the range 5 to 15. In the later-type barred galaxies, the central bar may be no thicker than the host disk. Kormendy (1993) has argued that many of the features identified as bulges from the surface photometry of more face-on galaxies may also be as thin as the disks. However, many edge-on galaxies show bulges which clearly do extend beyond the disk.

The bulges of spiral galaxies show a wide range of shapes, from boxy or peanut shaped bulges through to the more spheroidal systems. The boxy vs spheroidal structure of bulges is roughly understood in terms of their orbital properties but not in terms of origin. Many possibilities have been suggested for the origin of boxiness in bulges, including the formation and dissolution of bars, dissipative processes during the collapse of a rapidly rotating inner region, or later accretion events (see Sellwood, 1993; Pfenniger, 1993; Rowley, 1986; Whitmore and Bell, 1988).

Kormendy and Illingworth (1982) pointed out that the boxy bulges are frequently cylindrical rotators, unlike the more spheroidal bulges. This led to a burst of observational and theoretical studies of these systems (eg Binney and Petrou 1985; Rowley 1986; Shaw 1993), with the growing indication that these boxy or peanut-shaped edge-on systems may be associated with bars (Combes *et al.* 1990; Sellwood and Wilkinson 1993).

Elliptical galaxies have some properties in common with bulges, such as stellar content and the shape of the surface brightness profile for some of the larger spheroidal bulges. In some respects, bulges can be described as small elliptical galaxies sitting at the center of disks. Kormendy and Illingworth (1982) showed that bulges are typically fast rotators compared to the giant ellipticals and are mostly flatter than E4. Davies *et al.* (1983) showed that the lower luminosity ellipticals (luminosities comparable with those of bulges) are frequently rapid rotators, and that it is the giant ellipticals which are primarily the slow rotators. In the light of these studies, it is difficult to conclude whether there is much difference between bulges and ellipticals of comparable luminosity, all the more since many elliptical are now known to have faint disks (eg Franx 1993).

The Milky Way has an excellent example of a box-shaped bulge. This feature was seen in the early 2.4μm balloon scans (Matsumoto *et al.*, 1982), and spec-

tacularly confirmed by the 2.2μm image of the Galaxy from COBE[1]/DIRBE[2,3] (Weiland *et al.*, 1994: Arendt *et al.*, 1994) as seen in Figure 1.1 and from the contours plot of the COBE/DIRBE 2.2μm image (Figure 1.2).

The bulge of the Milky Way provides a unique opportunity to investigate the detailed pattern of rotation and velocity dispersion in a boxy galactic bulge. We can study the structure of the bulge to see if this boxy bulge is really a stellar bar, and we can also see how the bulge and disk are related dynamically.

1.1 The Milky Way

The Milky Way sits in a loose group composed of M31 and several small galaxies and satellites. Our Galaxy is large compared to its neighbors, except for M31. Its type is probably Sb-Sc, with a small central bar. It has a flat disk with a small bulge. If we were to view the Galaxy edge-on from outside, it would look much like NGC891, with probably more bulge than NGC891 but less than NGC4565 (see the Hubble Atlas). This can be seen in the COBE/DIRBE composite images (Figure 1.1).

In a more detailed description, the components of our Galaxy are

- thin disk : its radial scale length is of the order of 4 kpc and its vertical (z) scale height is about 300 pc. It contains most of the stars of our immediate neighborhood. The stellar abundances are approximately solar with an age ranging from nearly zero to the age of the Galaxy. Most stars have nearly circular orbits around the galactic center.
- stellar halo : mainly metal-poor old stars and globular clusters with metal abundances [Fe/H] between about −4 and −1. The density of the stellar halo near the sun is only about 1/1000 of that of the galactic disk near the sun. Recent evidence indicates that this halo may have formed from accreted satellites, including some satellites like Carina with a significant younger component: about 10% of the metal-poor halo stars are relatively young (see Freeman 1996 for a recent review).
- bulge : at the center of the disk, with stellar metal abundances Fe/H = −1 to 1. It is dominated by old stars and shows a small bar.
- thick disk : an old rapidly rotating disk population with a scale height of about 1 kpc.
- interstellar medium : a thin layer of gas and dust in the disk, where present and future stars are forming.
- dark halo : known only by its gravitational effect, extending out to a radius of about 100 kpc, and containing about 90% of the mass of the Galaxy (see Kochanek 1996 for a recent review).

[1]Cosmic Background Explorer

[2]Diffuse Infrared Background Experiment

[3]The COBE datasets were developed by NASA Goddard Space Flight Center under the guidance of the COBE Science Working Group and were provided by the NSSDC.

Figure 1.1: Composite image (in false-color) of the COBE/DIRBE images at 1.25, 2.2 and 3.5μm (blue, green and red). The main contribution to the light comes from the red giants that represent the main population of the galactic bulge and inner disk.

COBE/DIRBE composite image

1.25, 2.2 & 3.5μ (blue, green and red)

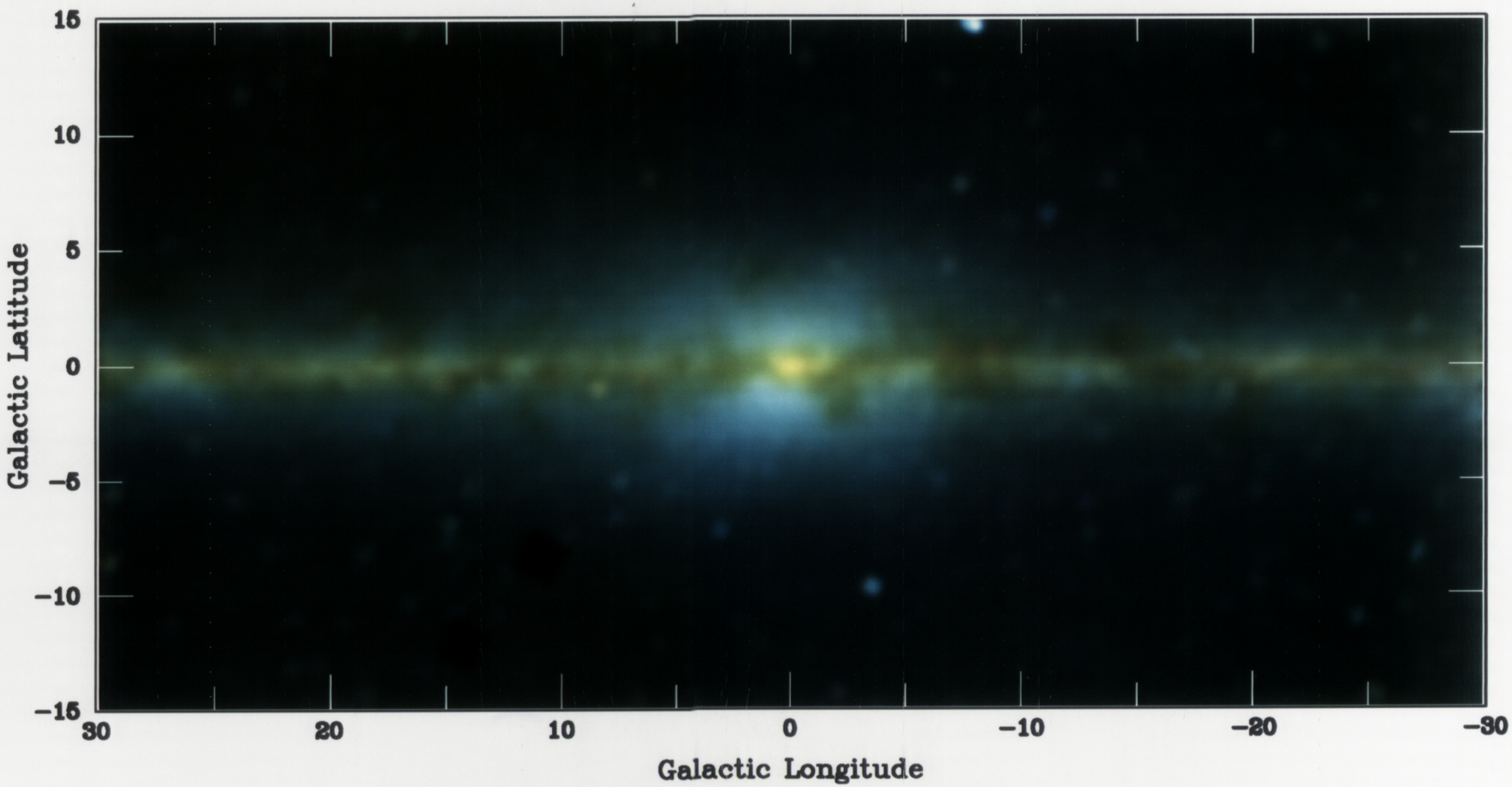

Figure 1.2: Contours of the COBE/DIRBE 2.2μm image.

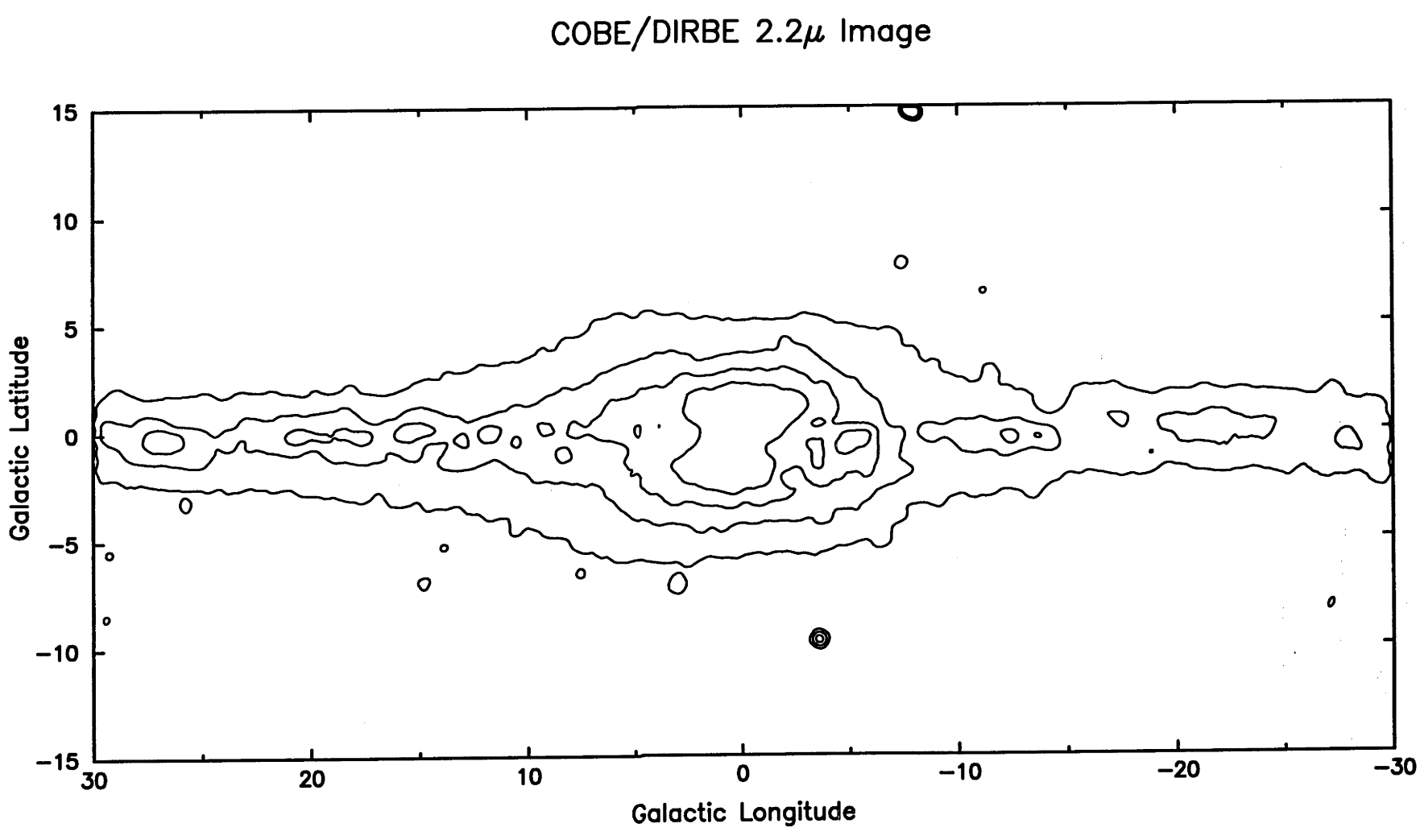
COBE/DIRBE 2.2μ Image
15
10
5
0
−5
−10
−15
Galactic Latitude
30
20
10
0
−10
−20
−30
Galactic Longitude

Figure 1.3: Image of the galactic bulge taken by ESO. The field covers $\approx 70°$ x $50°$.

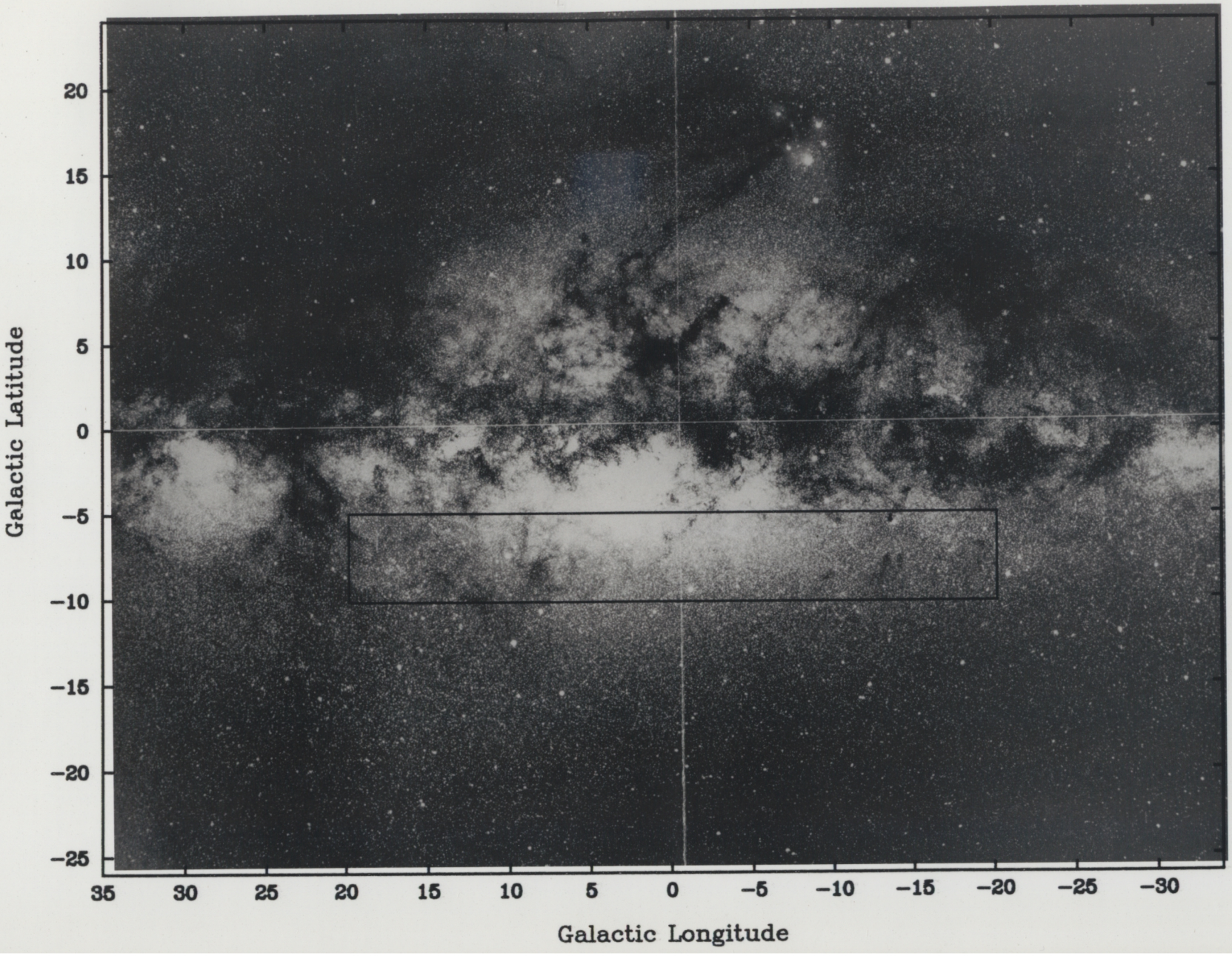
Galactic Latitude
20
15
10
5
0
−5
−10
−15
−20
−25
35
30
25
20
15
10
5
0
−5
−10
−15
−20
−25
−30
Galactic Longitude

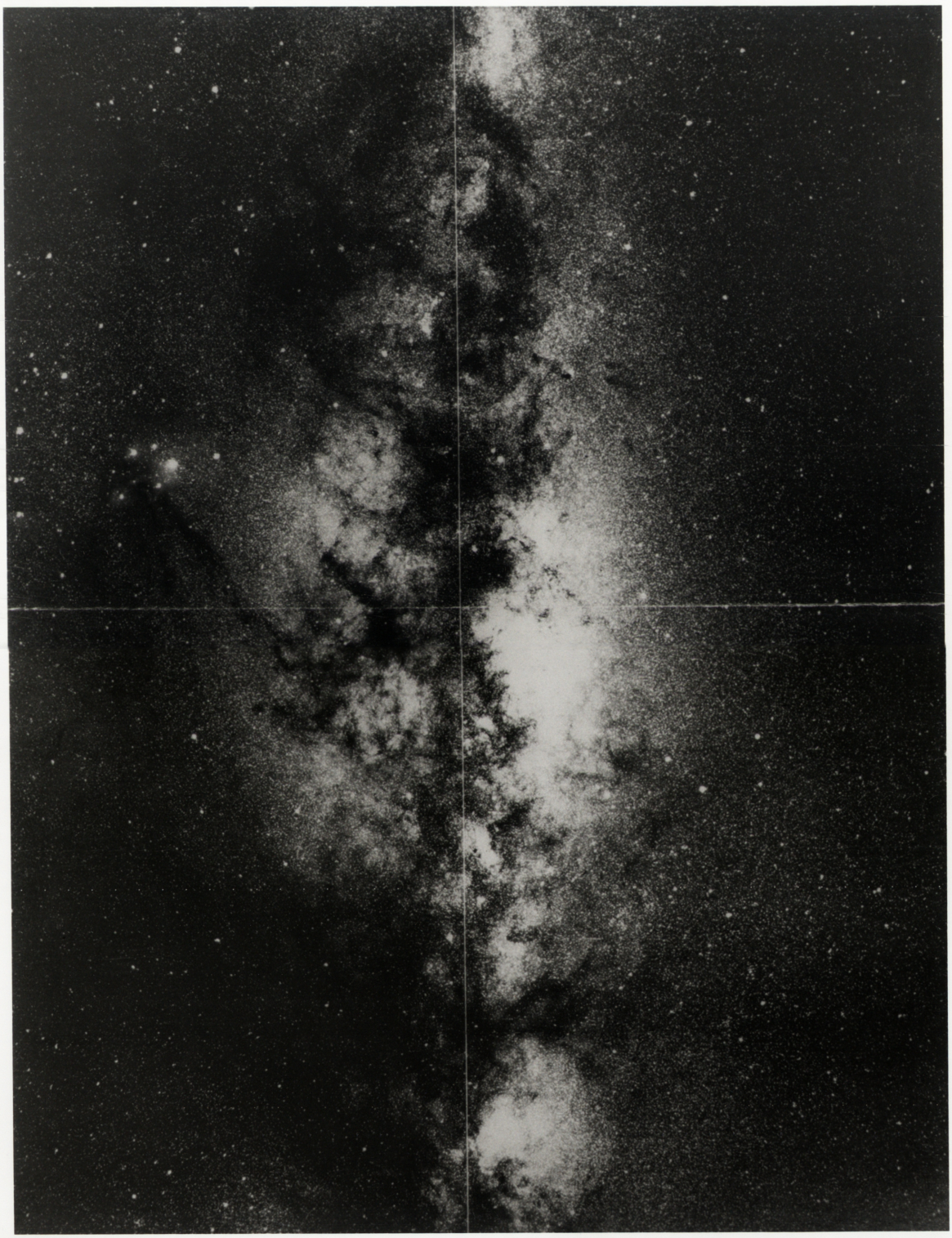

The location of the Sun, near the plane of the Galaxy and at a galactocentric radius of about 8.5 kpc, makes it difficult to get a good view of the central regions of our galaxy. The patchy extinction in the plane of the Galaxy is obvious from Figure 1.3, which is an optical image of the galactic bulge taken at ESO (Madsen and Laustsen, 1986). It is clear that the southern part of the bulge is much less affected by extinction than the northern part. The southern part includes two famous regions of relatively low extinction, Sgr I (l= 1.4°, b = –2.6°) and Baade's Window (BW) (l = 1.0°, b = –3.9°)[4] which are widely used for studies of the stellar population and dynamics of the inner bulge. The distribution of extinction over the bulge is also nicely shown from the work of the COBE/DIRBE group (Arendt *et al.*, 1994, figure 3b, plate L7).

1.2 Dynamics of the Bulge

1.2.1 Bulges and Bars

Evidences is accumulating that the boxy peanut-shaped bars seen in edge-on disk galaxies are associated with bar structures (Combes *et al.*, 1990; Jenkins and Binney, 1994; Blitz and Spergel, 1991; Kuijken and Merrifield, 1995). For the bulge of our Galaxy, the 2.4μm balloon scans and the COBE/DIRBE images show such a boxy peanut shape. An unambiguous direct identification of a bar at the center of the Galaxy is difficult because the sun is located in the plane of the Galaxy and our view of the galactic center is obscured by the dust. Nevertheless, much observational evidence is now pointing to the existence of such a bar. Here, we list only a few: see Gerhard (1995) for a more detailed review.

- de Vaucouleurs (1964) was the first to point out that a central bar is probably responsible for the non-circular motions of the HI in the inner part of the Milky Way. He had already noted that similar non-circular motions were present in the inner parts of barred spiral galaxies.
- The asymmetry in longitude of the distribution of the 2.4μm emission derived from the balloon scans indicated that the stars in the central kpc lie in a bar with its near side at positive galactic longitude and suggested that the bar is tilted relative to the galactic plane (Blitz and Spergel, 1991).
- The COBE/DIRBE images (Weiland *et al.*, 1994) confirm the asymmetry in the surface brightness distribution of the bulge in the near-IR, but show no evidence for an out-of-plane tilt of the bar.
- Weinberg (1992) reports that the distribution of variables in the IRAS Point Source Catalogue (PSC) is consistent with a bar with semi-major axis of 5 kpc and position angle of 36° $\pm$ 10° (where position angle is the angle between the major axis of the bar and the sun-center line and is taken as positive for a bar pointing into the positive galactic latitude quadrant).

[4]Throughout this thesis, (l, b) represent the new system (l^{II}, b^{II}), where the center (0°, 0°) is at $\alpha_{1950} = 17^h42^m.4$ and $\delta_{1950} = -28°55'$.

- Rohlfs and Kampmann (1993) show that the HI terminal velocities indicate the presence of a bar with a semi-major axis of 2-3 kpc and a position angle of about 45°.
- Gerhard and Binney (1993) used CO kinematics in the inner parts of the Galaxy to show the presence of a bar with a pattern speed of 63 km s^{-1} kpc^{-1}, a corotation radius of 2.4 kpc and a position angle of 16° ± 2°.

From some of these studies, and others on the brightnesses of tracer objects like Mira variables and clump giants in the bulge (eg Stanek *et al.* 1994), it seems fairly clear that the bulge objects at positive galactic longitude are brighter than those at negative longitude. This may be an indication that we are viewing the bulge at an angle from its major axis and that the closer end of the bar is at positive longitude. There is still disagreement on the parameters of the bar ie its length, strength, pattern speed and position angle.

1.2.2 Axisymmetric models

Kent (1992) used infrared (2.4 μm) surface photometry from the Spacelab infrared telescope to make an axisymmetric model for the luminosity density distribution in the inner galaxy. For the disk, he modelled the luminosity density L as a double exponential in R and z, and for the bulge he adopted

$$L(R,z) = 3.53K_0(s/667) \quad \text{for } s > 938$$

and

$$L(R,z) = 1.04 \times 10^6 (s/482)^{-1.85} \quad \text{for } s < 938.$$

where K_0 is a modified Bessell function. Here $s^4 = R^4 + (z/0.61)^4$ and the units of s in the equation above are parsecs. This form of the $L(R,z)$ distribution for the bulge leads to box-shaped isophotes.

Kuijken (1995) used a quadratic programming technique on a bilinear tesselation in the energy, angular momentum (E,L) plane to construct a two-integral distribution function $f(E,L)$ for a slightly modified version of Kent's axisymmetric model for the inner Galaxy. The distribution function is forced to give an isotropic velocity dispersion. With Kent's values for the mass to light ratios for the disk and bulge, the predicted line-of-sight velocity distribution in Baade's window is in excellent agreement with the distribution observed for the M giants by Sharples *et al.* (1990). However, the agreement is not so good for the velocity distribution of the K giants in Minniti's (1992) field at $l = 8°$, $b = 7°$: the discrepancy between the data and the prediction from the distribution function $f(E,L)$ is seen in the mean velocity and in the shape of the velocity distribution in this region. Kuijken suggests that the discrepancy might be associated with the triaxiality of the bulge, and points out how remarkable it is that his oblate, isotropic and axisymmetric model gives such a good fit to the velocity distribution in Baade's Window.

Our planetary nebulæ (see §1.4) will provide an opportunity to make further kinematical tests of Kuijken's axisymmetric isotropic two-integral model over a much more extended region of the galactic bulge than has previously been possible. We were not able to make such tests during this thesis program, but hope in the near future to make a more extended comparison of the predictions of Kuijken's model with our PNe data. It will be interesting to see if there are any further discrepancies that could also be attributed to the triaxiality of the bulge.

Durand *et al.* (1995) used a two-integral axisymmetric model with a Kuzmin-Kutuzov Stäckel potential (with a halo-disk structure) to study the dynamics of a sample of 673 PNe taken from the Acker (1992) Catalogue. The method fits the kinematics to the projected moments of a distribution function by means of Quadratic Programming. They conclude that their two-integral model does not adequately characterize the dynamical state of their sample of PNe.

Our particular interest here is in investigating the triaxial structure of the bar-bulge further, so we will not pursue the axisymmetric models in this thesis. The question is about the origin of central bar-bulges: do they arise from instabilities of the disk of galaxies or from other processes like the accretion of satellites or as part of the dissipative collapse of the galaxies. The quantitative study of the formation of bars through disk instabilities is now well advanced through N-body models, which we now discuss briefly.

1.2.3 N-body models

In the last few years, the growing evidence for a bar at the center of our Galaxy initiated much interest in developing detailed dynamical models of the galactic bar-bulge. Different kinds of models are now available, but the observational constraints on their stellar dynamics are not yet well advanced.

N-body models of the bar-forming instabilities of disks provide theoretical predictions of the dynamics of the resulting bar-bulges which can be tested against dynamical data from the galactic bulge and other bulges. For example, Fux (1995), Sellwood (1993) and Kalnajs (1996) have all modelled the instabilities of self-gravitating stellar disks through the formation of the central bar-bulge. As tests of the relevance of these models to the dynamics of the galactic bulge, the detailed kinematics of their models can be compared with the observed kinematics of tracer bulge objects like the planetary nebulæ which are the subject of this thesis.

Another kind of numerical model for the galactic bulge comes from the work of Zhao (1995) who constructed equilibrium Schwarzschild models for the COBE light distribution. Although these models do not provide direct insight into the formation of the bulge, in the way that the studies of disk instabilities can do, the Schwarzschild models are of much interest for evaluating the present dynamical state of the bulge. For this purpose, we can compare the kinematics of N-body realizations of these models with observational data, as above.

It would be most desirable if we could obtain an unbiased spatial distribution and the radial velocities of a subset of bulge objects. Such a database would allow us to distinguish between the various proposed models, and no doubt suggest others. Unfortunately most of the stellar objects have to contend with the high and patchy absorption near the galactic plane.

1.3 Planetary Nebulæ as tracers

To study the kinematics of the galactic bulge, we have access to a wide range of tracers: OH/IR stars (Habing, 1993), Miras (Whitelock, 1993), M giant stars, K giant stars (both individually and through the integrated bulge light) (Walker *et al.*; 1990 : Minniti *et al.*; 1992 : Terndrup, 1993), carbon stars (Whitelock, 1993), RR Lyræ stars (Walker and Terndrup, 1991) and planetary nebulæ (PNe) (Kinman *et al.*, 1988). The highly evolved OH/IR stars, Miras and M giants stars are probably biased towards the metal-rich population: the radial distribution of these objects is significantly steeper than the distribution of integrated light in the bulge (de Zeeuw, 1993), and the kinematics of these objects reflects the kinematics of the metal-rich component of the bulge. The carbon stars are rare and are also an indication of an intermediate age metal-rich population. The K giant stars are found at all metallicities and would be the ideal tracers to use since all bulge stars are likely to go through a K giant phase, but they are relatively faint. The K giants have already provided important dynamical information (eg Terndrup *et al.* 1995; Ibata and Gilmore, 1995a,b), and much more will appear in the future from the large fiber surveys in progress (eg Harding and Morrison, 1993). The RR Lyræ stars are also useful bulge tracers but they are biased toward the metal-poor population and they are fainter than the K giants. The PNe are probably less affected by metallicity bias than most other tracers: recall the presence of PNe in the very metal-poor globular cluster M15. Their spatial distribution and their high velocity dispersion indicate that most of the bulge PNe are old objects. Their strong H_α and [OIII] emission lines make their velocities easy to measure. We have thus decided to use the PNe as probes to study the kinematics and dynamics of the galactic bulge.

A planetary nebula is a shell of gas shed by an old star through radiation pressure. The shell is expanding almost symmetrically with an expansion velocity of about 25 km s^{-1}. We are able to see the nebula because the central star produce enough ultraviolet radiation to ionize the gas within the shell. The nebula may continue to shine for up to a few 10^4 years as the central star evolves toward its final stage, the white dwarf. It is believed that probably all low and intermediate mass stars (0.8 to 8.0 $M_\odot$) eventually go through this phase (Stasińska, 1993). Figure 1.4 show an Hertzsprung-Russell (HR) diagram with the typical evolution of a PN from the asymptotic giant branch (AGB) to its final white dwarf stage (Iben and Kaler 1992, figure 1, page 477).

The spectrum of a PN is very rich in emission lines. Among the most prominent lines in the visual and red part of the spectrum we find H_α λ6562 Å, [NII]

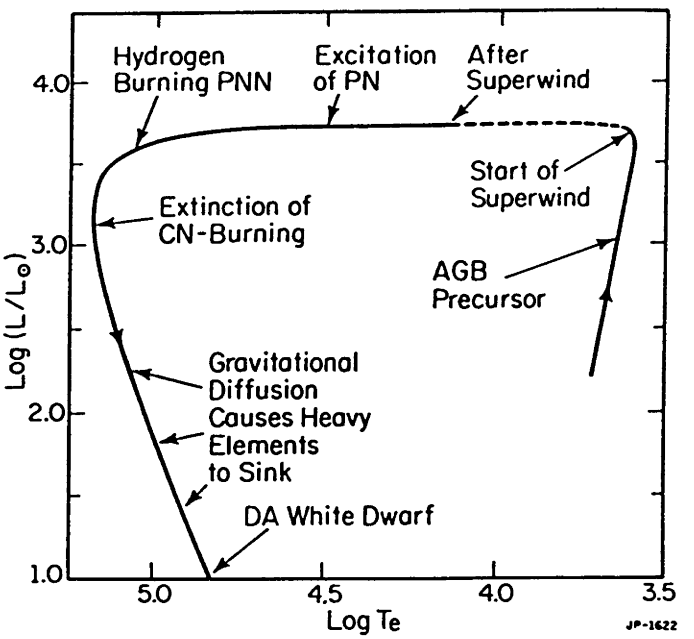

Figure 1. The evolutionary track in the Hertzsprung–Russell diagram of a model star that ejects nebular material during the quiescent hydrogen-burning phase on the asymptotic giant branch (AGB). It has been assumed that ejection occurs via a stellar superwind at a rate of $10^{-5}\ M_{\odot}\ \mathrm{yr}^{-1}$. The star evolves along the dashed portion of the curve. (PN = planetary nebula; PNN = planetary nebula nucleus [central star].) Following the cessation of mass loss, the model then evolves for about 10^4 yr to the point where hydrogen burning by CN-cycle reactions ceases, whereupon the luminosity of the model drops by a factor of 10 in 10^3 yr. From then on dimming occurs at an ever decreasing rate. Gravity at the stellar surface is large enough to cause element segregation: Helium and other heavier elements sink into the interior while hydrogen floats to the top. The surface composition becomes essentially pure hydrogen. In short, the model has become a DA white dwarf.

Figure 1.4: Hertzsprung-Russell diagram of a typical evolutionary track for a model star. This C-M diagram is from figure 1 of Iben and Kaler, 1992, page 477.

$\lambda\lambda$ 6548,6583 Å, [SII] $\lambda\lambda$6731,6717 Å, [OIII] $\lambda\lambda$4959,5007 Å and HeII λ4686 Å. Symbiotic stars, which are late-type giants (G, K, M or carbon) shedding mass on to a more compact companion (Allen, 1984), can also exhibit strong and broad H_α λ6562 Å and sometimes strong [OIII] $\lambda\lambda$4959,5007 Å which can confuse the identification of the object in some cases. Strong [SII] doublet lines indicate high density in the nebula and we can measure the electron density N_e from ratio of [SII] λ6717 / λ6731. Typical electron densities for PNe are of the order of 10^2 (for the old PNe) to 10^5 cm^{-3} (for the young PNe), assuming an electron temperature of T= 10^4 °K (Osterbrock, 1989).

The typical mass of the nebula is in the range of 0.1 to 1.0 $M_\odot$. The apparent diameter of a PN in the bulge is a few arcsec, depending on its age. As a PN gets older, it expands and the density drops to a point where it become optically invisible. Determination of the angular diameter may differ by a factor of two between optical and radio measurement (Stasińska *et al*, 1991a,b).

The distances of PNe are still poorly known. Using the optical diameter as a distance criterion is not adequate because PNe have a wide range of absolute diameters. Nevertheless, using the angular diameters, spatial distribution and radial velocities of a sample of PNe, Gathier (1983) estimated that probably 80% of the small (diameter < 20″) PNe within 10° of the galactic center belong to the bulge. While it is clear that most of the PNe towards the bulge are associated with the bulge, it is also evident that their apparent spatial distribution at low galactic latitudes is affected by the interstellar absorption.

1.4 Existing Surveys

It is estimated that the Galaxy contains between 10^4 and 4×10^4 PNe (Pottasch, 1992). Only a small fraction of these PNe have been detected so far. The Strasbourg-ESO Catalogue of Galactic Planetary Nebulæ (Acker *et al.*, 1992) reports that 1820 objects have been called at least once a PN and that 1143 of those are considered true or probable PN. Figure 1.5 show their distribution in galactic longitude l and galactic latitude b. We clearly see from this picture that the concentration of PNe is towards the galactic plane and bulge. But, there is also a clear deficiency of PNe near the galactic plane caused by the dust extinction.

Apart from a few serendipitous discoveries of PNe, most of them were found through important but incomplete surveys using the objective prism technique (Minkowski, 1965) and photographic plates (ie the Palomar Survey and the ESO Survey). Some surveys were conducted in the radio continuum (Ratag, 1990). Then, the era of the IRAS (InfraRed Astronomical Satellite) in 1984 brought a new way of selecting candidates by using the far infrared (FIR) excess, associated with dust in the nebula, as a selection criterion. This method produced a fair number of new discoveries (Ratag, 1990: Van de Steene, 1995). These surveys will however still be incomplete. In the case of photographic plates and objective prism surveys, faint nebulæ and compact young PNe will not be detected. With IRAS, although it has the capability to detect objects in regions of high extinction,

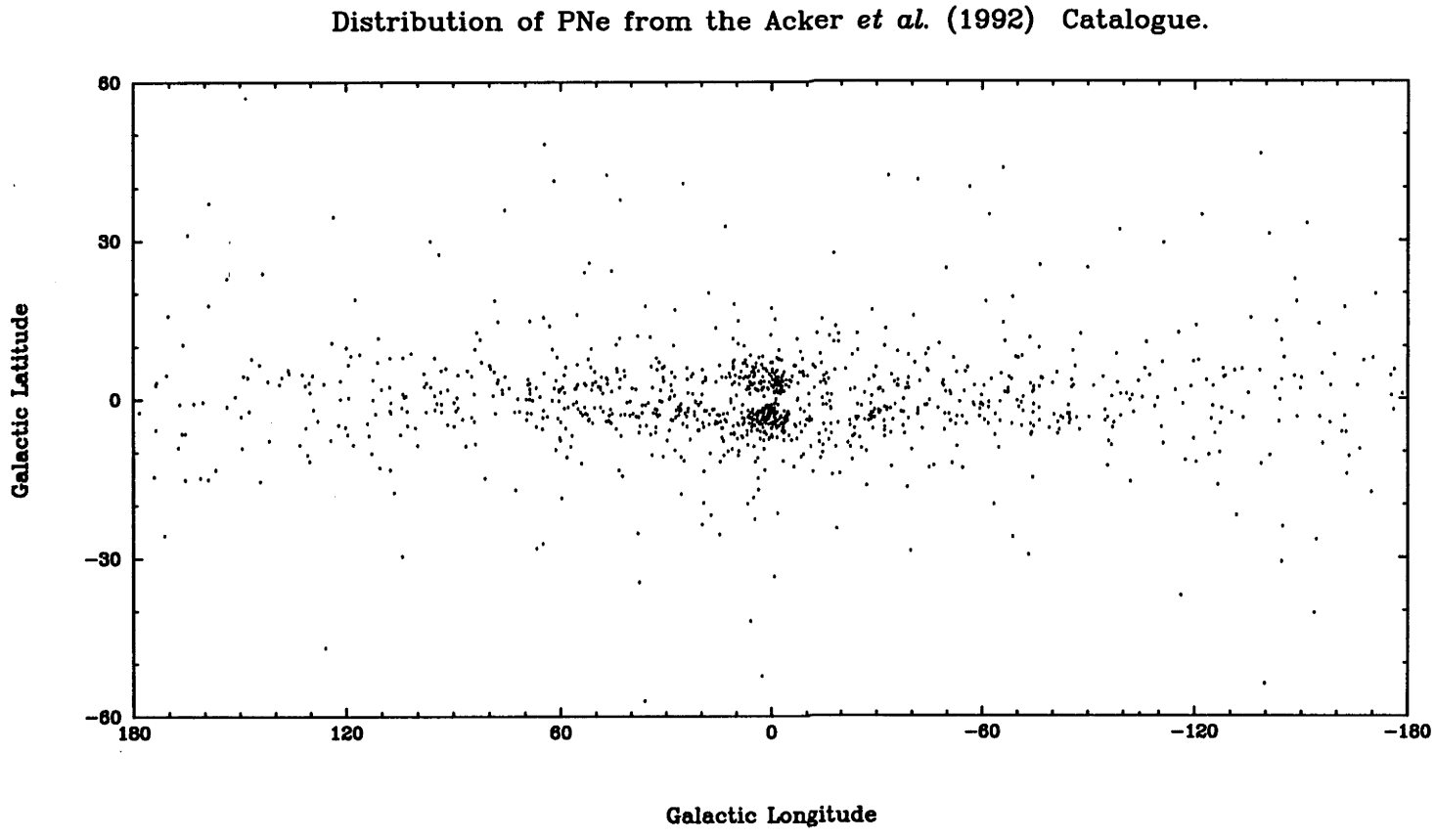

Figure 1.5: Distribution of the Galactic Planetary Nebulæ from Acker *et al.* (1992) in (l, b).

it is more likely to detect the dusty PNe. If a PN has a low dust density (this is more likely for old PNe) it will not be detected by IRAS.

Our goal is to make a deep and uniform survey for PNe in a large region of the bulge, measure their radial velocities and then use the kinematical data to test dynamical models of the bulge. Because PNe are strong emitters in H_α and [OIII], we decided to conduct a deep narrow-band optical imaging survey of an extended region in the southern bulge. Chapters 2 and 3 describe the complete procedure we followed in order to discover new PNe. We start with the data acquisition and reduction of the Optical Imaging Survey (Chapter 2), then follow the Optical Spectroscopy Survey (Chapter 3). The final results for the new discoveries and new data for already known PNe are at the end of Chapter 3. The catalogue is the subject of Chapter 4. We present the H_α and the continuum finding charts, and the spectrum associated with each new object. Chapter 5 contains the analysis and comparison with the dynamical models, and a summary is presented in Chapter 6. The list of references is presented at the end of the thesis.

Chapter 2

Optical Imaging Survey

In our study, we are interested in the PNe of the bulge, and particularly in the PNe at higher galactic latitude because of their importance for investigating the dynamics of the boxy/bar regions. The COBE/DIRBE maps (Weiland *et al.*, 1993) indicate that the galactic bulge covers the regions of galactic longitude l = $\pm 15°$ and galactic latitude b = $\pm 10°$. Because of time restrictions, it was not possible to survey this entire bulge region. We have chosen to survey the southern part: l = $\pm 20°$ and b = $-5°$ to $-10°$ because of its lower extinction relative to the northern bulge. The choice of surveying the longitude region outside the bulge is intended to provide us with data for the transition from the bulge to the disk.

Planetary nebulæ emit strongly in the [OIII] $\lambda\lambda$4959,5007 Å and the H_α λ6562 Å lines. Since an [OIII] line survey would be more affected by the moon (more scattering), the H_α line was chosen because it allowed observing in grey and dark time. We also considered using the [SIII] line at λ9530 Å. Although this line would perform very well in situations of higher interstellar extinction and brighter moonlight, it lies in a region where CCDs have lower quantum efficiency, and this would have significantly increased the time required for our survey.

In this chapter, we describe the entire procedure followed in order to search for candidate PNe. We first discuss the observations, then move on to the data reduction techniques, followed by the search and coordinate search for candidate PNe.

2.1 Observations

In two observing seasons, we conducted our uniform narrow-band imaging survey of this region of the bulge, in H_α and the nearby continuum, to build a database of newly-found planetary nebulæ that will be combined with the already known PNe in this region. The LDSS (Low Dispersion Survey Spectrograph) (Figure 2.1) of the Anglo-Australian Observatory was attached to the 1.0m telescope of Mount Stromlo and Siding Spring Observatories and was used as a focal reducer (without grism). This instrument, with the 100 mm interference filters and a 1024 x 1024 CCD, gives a useful circular field of 30 arcmin at 2.35 arcsec per pixel. Throughout the survey, several CCDs were used depending on their availability. A list of all the CCDs used, with their characteristics, can be found in Table 2.1. Column 1: the MSSSO dewar identification, Column 2: the CCD type, Column 3: the physical size in pixels, Column 4: the pixel size, Column 5: the readout noise and Column 6: the electronic gain.

The H_α filter was designed for a central wavelength at [NII] λ6590 Å . In order to obtain the central wavelength for H_α λ6562 Å , we had to tilt the filter at a 5° angle to the optical axis of the instrument. For the nearby continuum associated with the H_α, we used the Omega 645 filter, which did not require to be tilted. A detailed list of all the filters used can be found in Table 2.2. Column 1: the filter identification, Column 2: the type and size, Column 3: the central wavelength in Å , Column 4: the filter passband in Å , Column 5: the tilt angle, and Column 6: the central wavelength after tilt.

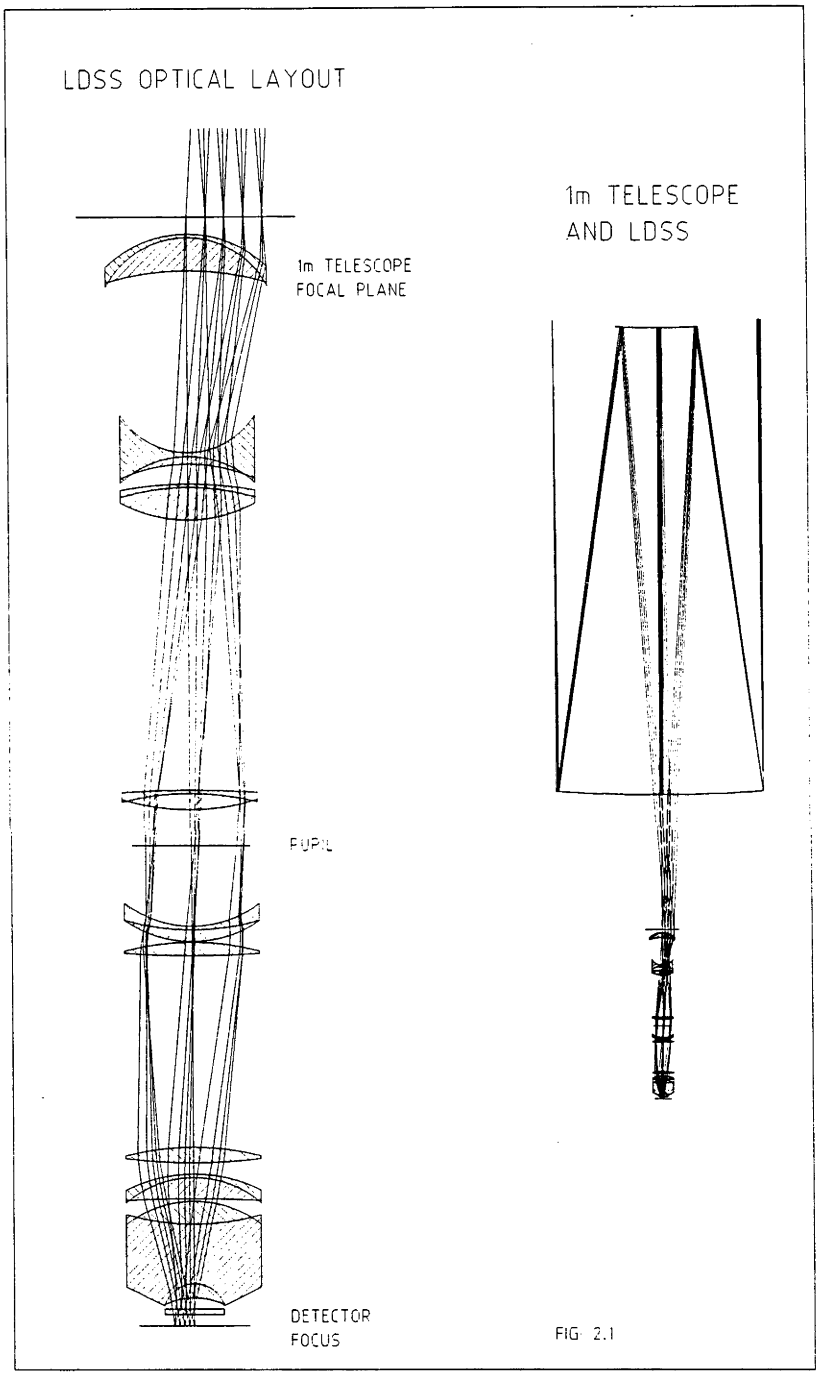

Figure 2.1: Diagram of the LDSS (Low Dispersion Survey Spectrograph) Optical Layout.

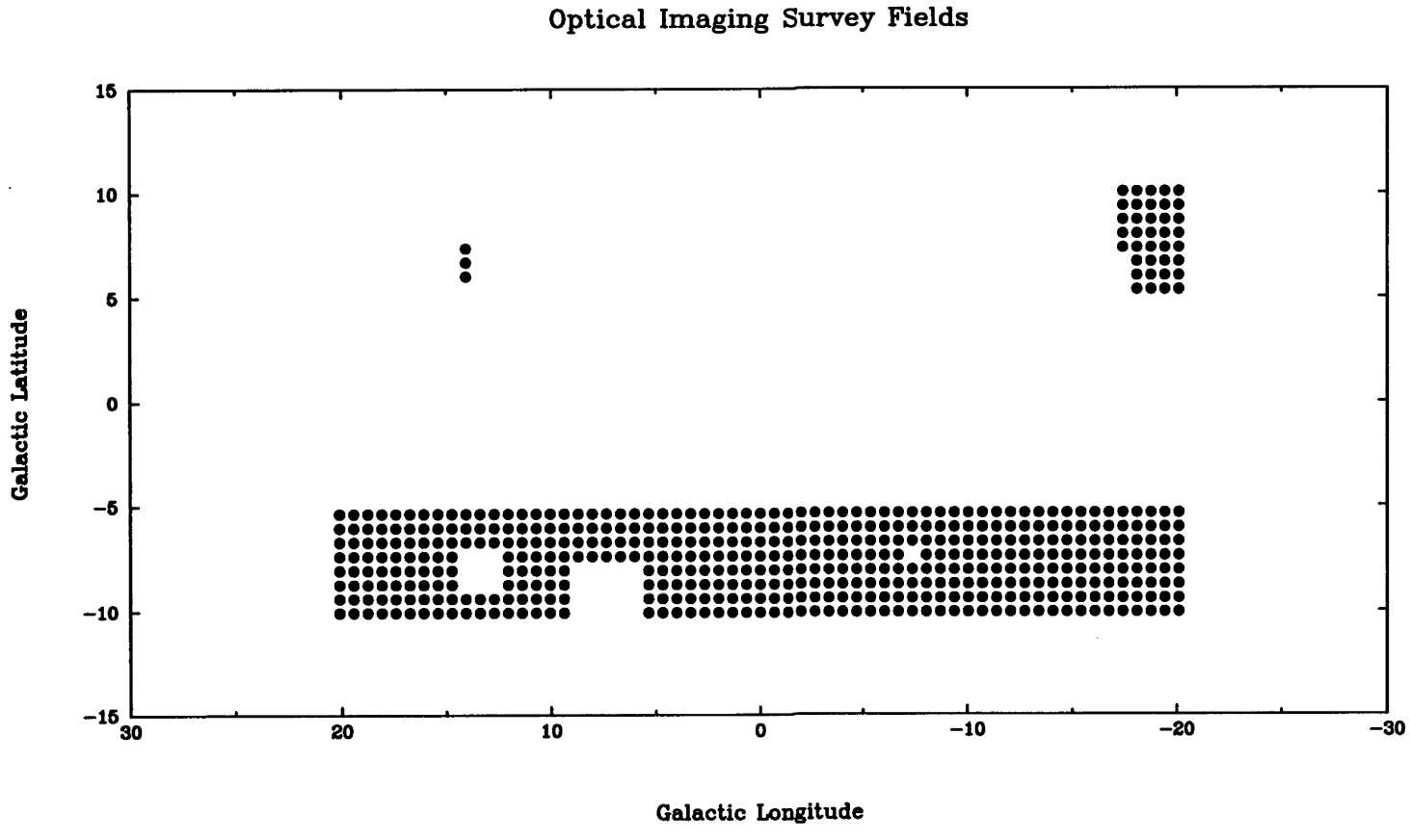

Figure 2.2: Optical Imaging Survey grid with fields observed.

Table 2.1: CCD characteristics

CCD #	Type	Size	Pixel	RN	Gain
4	TEK-UV Thin	1024^2	24μ	5.9	1 e^-
6	LGEC-E2	2186 x 1152	22.5μ	5	1 e^-
9	TEK-E1 Thin	1024^2	24μ	24	1 e^-
11	TEK-E2 Thin	1024^2	24μ	7	1 e^-

The H_α filter was positioned in the aperture plate holder which is situated at the focal plane. At this position, there is enough free space to allow the filter to be tilted and it has the further advantage that all beams have a similar angle of incidence at the filter, so the effective passband does not vary over the field. This is not the case at the pupil plane, which is the alternative filter position in the LDSS. A disadvantage of putting the filters at the focal plane is that the diameter of the field of view is about 10 arcmin smaller than it would be if the same filter were located in the pupil plane. The continuum filter can be placed at the pupil plane, because the precise passband is of less importance for this filter.

By uniformly spacing our 30 arcmin fields of view over the area l = $\pm 20°$ and b = $-5°$ to $-10°$, we produced a grid of 488 fields. In two seasons of observation, we covered 94% of the grid (458 fields). Although there were no plans to observe the northern part of the galactic bulge, we did obtain 40 fields in the equivalent northern galactic latitude strip, b = $+5°$ to $+10°$: in early May (beginning of the bulge season in the southern hemisphere), the southern part becomes accessible only 3 hours after dusk and we used the first three hours of the nights during that period for these northern fields.

In Figure 2.2, the filled circles represent the fields we have observed. The three empty regions in the southern grid are the 30 remaining fields which were unobserved due to a lack of time. Each circular field covers roughly half of the total area associated with each grid point and, added together, they represent about 1% of the total COBE light.

In addition, we took 15 fields in [OIII] λ5007 Å (during dark time). PNe are strong emitters in [OIII], and we wanted to test the possibility of finding more candidates by using this line, which is widely used for surveys of extragalactic PNe. The [OIII] filter was combined with a BG40 blocking filter in order to block its red leak. Again, this filter was designed for a central wavelength of λ5020 Å and so needed to be tilted at a 4° angle to the optic axis in order to obtain the central wavelength for [OIII] λ5007 Å . For the nearby continuum, we used the Omega 475 filter (Table 2.2).

Two exposures in H_α of 500 seconds and one exposure in the nearby continuum at 300 seconds were taken. The same procedure was applied for the 15 fields in [OIII]. The two exposures in H_α and in [OIII] were necessary to ensure removal of

Table 2.2: Filter details

Filter	Type	λ_c Å	$\Delta\lambda$ Å	tilt angle	λ_c (with tilt) Å
H_α	Coherent/Scientific 100mm	6590	19	5°	6563
[OIII]	Coherent/Scientific 100mm	5020	40	4°	5007
Continuum	Omega 100mm	6450	–	0°	–
Continuum	Omega 100mm	4750	–	0°	–

Table 2.3: Observing log for the 1.0m Optical Imaging Survey.

Date	No. of nights	Clear nights	CCD #
25-31 May 1993	7	65%	11
11-22 June 1993	12	50%	11
19-29 July 1993	11	30%	4 & 11
9-18 Aug 1993	10	55%	4
16-23 May 1994	8	80%	9
31 May-5 June 1994	6	60%	6
30 June-3 July 1994	4	75%	6
7-12 July 1994	6	30%	6
1-8 Aug 1994	8	70%	6

cosmic rays: see §2.3. Typical sky counts for the H_α were 75 to 150 (depending on the presence of moonlight) and about twice this level for the continuum.

During the two observing seasons, we were allocated a total of 72 nights at the 1.0m telescope with a success rate of clear nights (not necessarily photometric) of 57%. A summary of the Observing log can be found in Table 2.3. Column 1: the period covered in each observing run, Column 2: the number of nights per run, Column 3: the proportion of clear nights per run and Column 4: the CCD used during each run.

2.2 Data reduction

The basic reduction (bias subtraction and flatfielding) was performed using the standard techniques (Gilliland, 1992 : Massey, 1992) in the **ccdred** package

within the NOAO[1]/IRAF[2] Data Reduction and Analysis System. Calibration images of approximately 10 bias, one dark and twilight flatfields (in each wavelength band) were obtained each night. Twilight flatfields, were obtained at dusk and dawn whenever it was possible.

For each image, the electronic bias level was removed to first-order by fitting a chebyshev function to the overscan region and then subtracting it from each column. In order to remove any remaining bias structure, a master bias frame was created (**zerocombine**) by averaging the 10 bias frames using a *minmax* rejection algorithm and then subtracting it from the image. We did not use the dark frames since no dark signal was detected. A minimum of 3 flatfields were taken by stepping the telescope slightly between each exposure and then combining them according to their wavelength band. For each band, a master flat was created (**flatcombine**) using the *median* option with the *avsigclip* rejection algorithm, the scale set to *mode* and a ± 3 sigma clipping in order to remove any cosmic rays and stars. The image was then divided by the master flat.

2.3 Search

In studying the bulge of the Milky Way, we are challenged with the difficulty of finding H_α emitters in dense star fields. The most straightforward method to detect our H_α candidates was to combine the two H_α frames and then divide the H_α image by the continuum image for each field. With the correct scaling, the stars disappear in the quotient image, and the H_α emitters are readily visible. The advantage of division over subtraction is that the noise in the quotient goes down where the signal goes up and the H_α emitters appear. To illustrate this, say x and y are both normally distributed with $[\mu_x, \sigma_x]$ and $[\mu_y, \sigma_y]$ as their mean and standard deviation respectively. Then, the mean of the ratio x/y is μ_x/μ_y and its standard deviation is

$$\frac{\mu_x}{\mu_y}\sqrt{\frac{\sigma_x^2}{\mu_x^2}+\frac{\sigma_y^2}{\mu_y^2}-2\rho\frac{\sigma_x\sigma_y}{\mu_x\mu_y}}$$

where ρ is the correlation coefficient between x and y (eg Menzel, 1960). If we take the difference, the mean of x-y is $\mu_x - \mu_y$ and its standard deviation is

$$\sqrt{\sigma_x^2+\sigma_y^2}$$

In our situation, where $\mu_x \approx \frac{1}{2}\mu_y$ and (σ_x, σ_y) come from Poisson noise, the noise in the quotient goes like

$$\sqrt{3/8\mu_x}$$

[1]Operated by the Association of Universities for Research in Astronomy, Inc. under contract with the National Science Foundation.

[2]Image Reduction and Analysis Facility

while the noise in the difference goes like

$$\sqrt{3\mu_x}$$

But a drawback of this procedure (the division) is that the photon statistics in the quotient image are no longer gaussian. Since our goal here is to remove the stars and make the H_α emitters appear for the purpose of detection, the photon statistics problem is not so important - we note here that we are not attempting photometry of the detected H_α objects with this technique.

Combining two H_α frames was necessary in order to remove cosmic rays. For the continuum, it was not crucial to obtain two frames as the cosmic rays will appear as low (dark) values in the quotient image. Because the seeing varies during the night and from one night to another, we were careful to take the three images of a field during the same night and as close in time as possible.

Before dividing, we need to get the sky level and the total star signal similar in the three images, so we must perform two kind of scaling.

- a first scaling of the continuum image so that the total star signal above the sky is the same as for the H_α image. This involve a multiplicative scaling.
- a second additive scaling to adjust the sky level of the continuum image so that it is the same as for the H_α image.

A division of the H_α image by the scaled continuum image will then, in the absence of seeing effects and noise, cause the stars to disappear and leave behind only the H_α emitters visible above the divided sky level. The pixel values of the quotient image will thus lie near 1.0 except for (i) H_α absorption in some stars, (ii) (dark) cosmic rays from the continuum image and (iii) the H_α emitters.

We begin by calculating shifts (**imshift**) between the three images using one as a reference in order to register them properly. We used a *linear* interpolation with the boundary set to *nearest*. Then, we obtain the final H_α image by combining the two H_α images using **imcombine** with the *minmax* reject algorithm in order to reject the highest value of each pixel - this allow for the rejection of cosmic rays. For a set of 2 images, the S/N ratio of the *minmax* image is a factor of ≈ 1.2 higher than the S/N ratio of a single image. The use of the *minmax* reject algorithm is also justified here by the fact that we do not intend to do any photometry but just perform an object detection. Many of our nights were non-photometric anyway.

In order to do the scaling to match the total star signal above the sky for the H_α and the continuum images, we selected a box of Q pixels, carefully chosen to avoid bright saturated stars, bad columns and vignetted regions. The total star signal in the box is $S_\star = N_{total}$ - Q n_{sky} where N_{total} is the total (stars + sky) photon count in the box and n_{sky} is the mean pixel sky level in the box.

The sky level, n_{sky} is the mode obtained from the pixel histogram using the task **imhistogram**. N_{total} is derived directly using **imstat**. Thus, the multiplicative factor, f, for the continuum image is

$$f = \frac{N_{total,\alpha} - Qn_{sky,\alpha}}{N_{total,c} - Qn_{sky,c}}$$

After multiplying the continuum image by f, its total star signal is the same as for the H_α image. Its sky level is f $n_{sky,c}$. We then subtract from the scaled continuum image the constant Δ = f $n_{sky,c}$ - $n_{sky,\alpha}$ as the final step before dividing the H_α image by the continuum image.

We now have the continuum image scaled and offset so that its total star signal above the sky and its sky level are the same as for the H_α image. The last step towards finding H_α emitting objects is to divide the H_α image by the scaled continuum image.

The resulting quotient image will then have pixel values near 1.0, except for the effects of

i) H_α emitting objects – these appears as bright regions and are readily visible
ii) cosmic rays in the continuum – these appears as regions of low signal in the quotient image
iii) stars with strong H_α absorption – these appear dark in the quotient image
iv) residual misalignment, errors in scaling and different seeing for the H_α and continuum images

After a thorough and systematic visual examination of the quotient images for our 498 fields, we have a total of 148 H_α detections. Figure 2.3 (on two pages) shows examples of images for a set of 4 objects. The montage is composed of the H_α, the continuum and the quotient images. These 4 objects represent typical cases found in our fields. One of them, 345.26–8.71, is a catalogued object. The remaining three objects are new discoveries.

We did not use an automatic detection procedure because it soon became clear that a visual search was very effective for identifying H_α emitters and rejecting ghosts and defects.

The same technique was applied to the 15 [OIII] fields. There was a total of 14 [OIII] detections, all of which had been detected in H_α. Two objects detected in the H_α images were not detected in [OIII]. These two objects are probably symbiotic stars (symbiotic stars emit in H_α and sometimes [OIII] but the [OIII] emission can be weak or absent). The spectroscopic follow-up will determine the true nature of these objects.

Figure 2.3: Montage of a set of 4 objects (two per pages) with the H_α, the continuum and the quotient images.

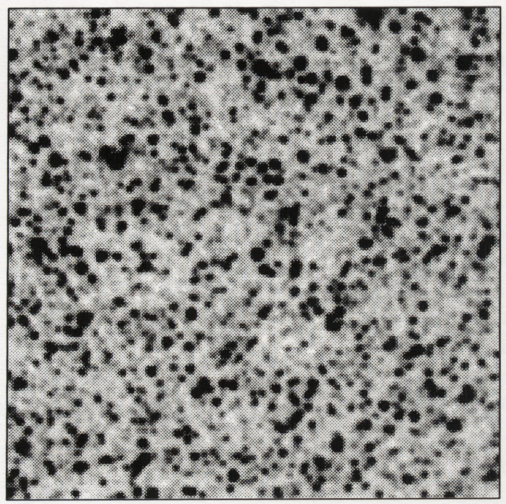

004.2−05.2 H_α

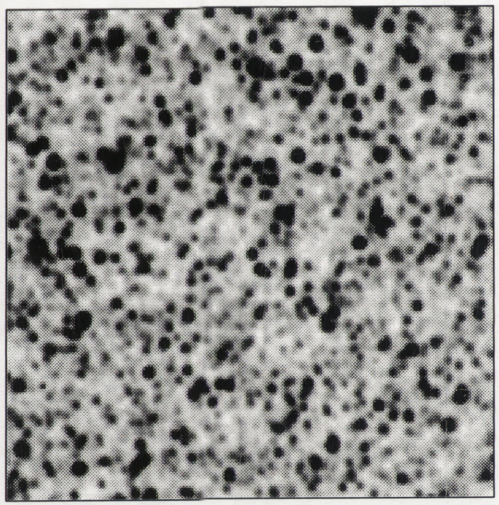

004.2−05.2 Cont

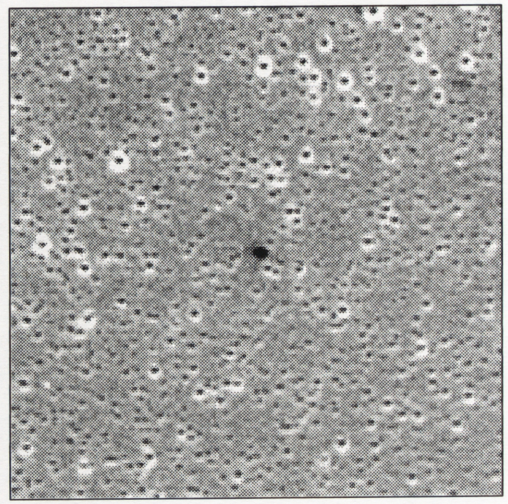

004.2−05.2 Quotient

345.2−08.8 H_α

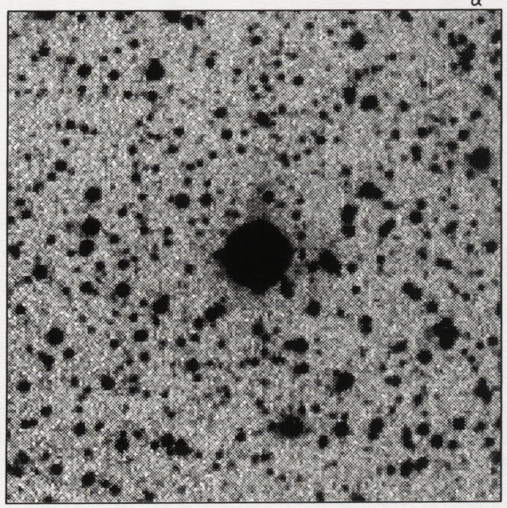

345.2−08.8 Cont

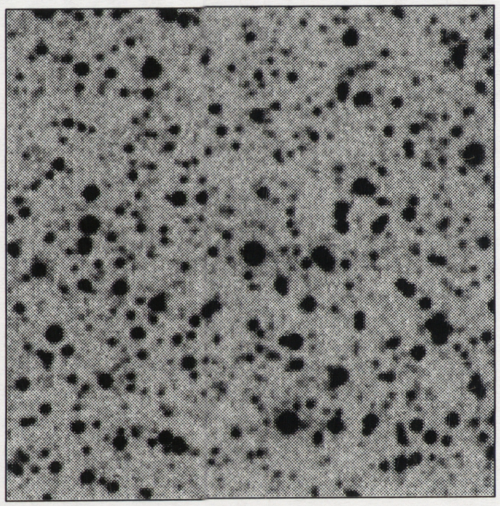

345.2−08.8 Quotient

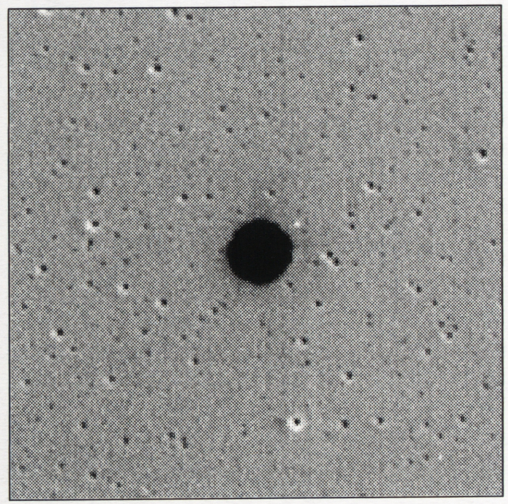

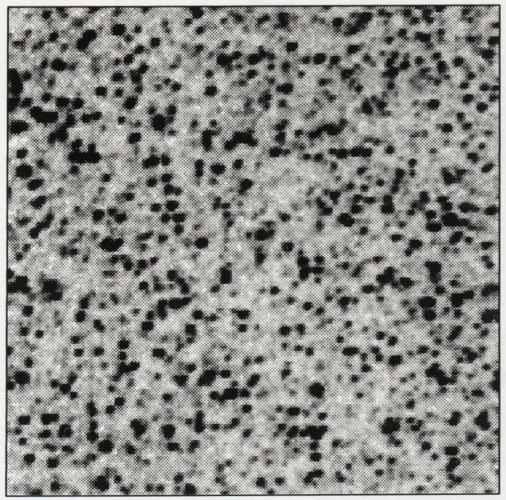

005.4−06.1 H_α

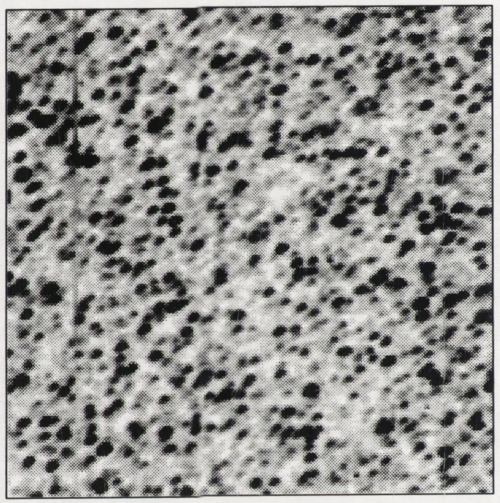

005.4−06.1 Cont

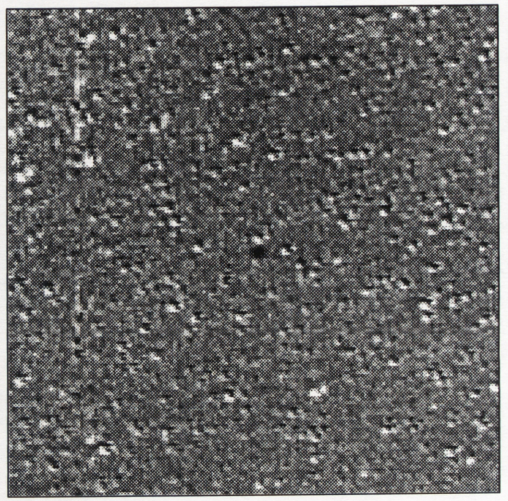

005.4−06.1 Quotient

000.1−08.0 H_α

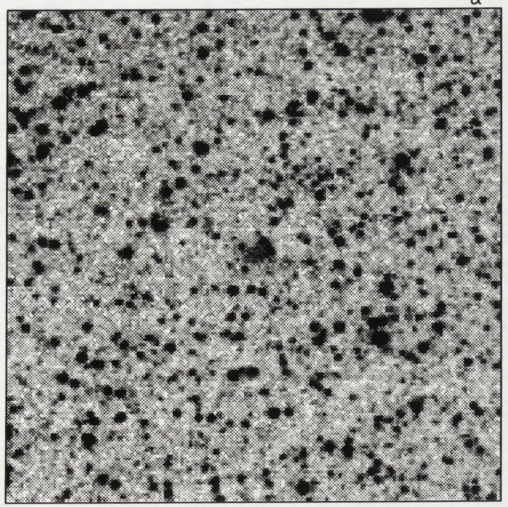

000.1−08.0 Cont

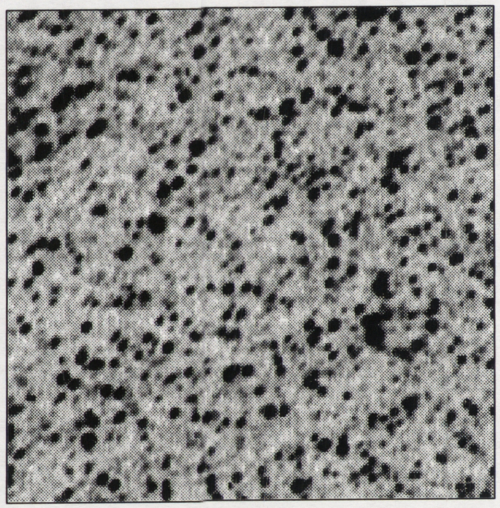

000.1−08.0 Quotient

Table 2.4: Search results of the 1.0m Optical Imaging Survey.

Filter	Detections	Known	Candidates
H_α	148	51	97
[OIII]	14	14	0

2.4 Astrometry

The last step of the optical reduction is to perform an astrometric solution for each frame containing a candidate in order to derive the equatorial and galactic coordinates.

The method to perform astrometric solution is straightforward. We used the *Guide Star Catalogue*[3] (GSC) within the IRAF environment to obtain a finding chart centered on the field. The IRAF tasks used to create those finding charts were **region** and **skymap** from the **gasp** package. We then identified approximately 10 reference bright stars in our field in order to obtain a good solution. Using the astrometric program **astrom**[4], we used the equatorial coordinate list of those stars provided by the GSC, the pixel positions of those reference stars on our frame and the pixel position of our candidate to estimate (α, δ) and (l, b) for the PN candidates. The program uses a linear 6-coefficients fit to calculate the solution and gave rms residuals of less than 0.5 arcsec for the reference stars.

Once the equatorial coordinates are obtained for each candidate, the next step is to cross-check the position of our candidates with catalogues of known planetary nebulæ in order to identify those which are already catalogued. We used the Acker *et al.* (1992) catalogue which is the most up-to-date. In addition, we searched through Ratag's and van de Steene's thesis (Ratag, 1990, van de Steene, 1995) because, for Ratag's list of discoveries, if the optical finding chart was not available, Acker *et al.* (1992) listed his discoveries as "probable PNe" in their catalogue and, for van de Steene's list, her work came after the publication of the catalogue.

Table 2.4 show the result of the final count for our 148 detections in H_α and 14 detections in [OIII]. Of the 51 known objects, 45 are PNe and the remaining 6 are catalogued as either symbiotic stars or peculiar emission line objects in the Acker *et al.* (1992) catalogue. None of our objects was found in van de Steene's thesis and objects found in Ratag's thesis were already reported in the catalogue as "probable PNe". We note that one of the two objects which did not show up in our [OIII] images is classified as a symbiotic star in the Acker catalogue. The other one will need spectroscopic investigation.

We wished to ensure that all the Acker catalogue objects have been recovered

[3]GSC is an all-sky astrometric and photometric catalog and was prepared by the Space Telescope Science Institute (STScI)

[4]A program within the Starlink software / Starlink Project, funded by PPARC at RAL

in our deep survey fields. We thus performed a search in the catalogue within a radius of 15 arcmin of our field center (our circular field-of-view is roughly 30 arcmin in diameter). The search showed that 7 objects from the catalogue were not recovered in our fields. After investigating these objects, it became clear that they were all at the edge of our circular field-of-view and were lost in the vignetting of our frames (we recall that our grid of circular fields covers about half of the total area within the survey region).

Chapter 3

Optical Spectroscopy Survey

We are using PNe of the galactic bulge to investigate the bulge's kinematics and dynamics. Since PNe have strong emission lines, it is relatively quick and easy to measure their radial velocities spectroscopically. The Acker *et al.* (1992) catalogue of galactic PNe includes 326 objects located in the more extended bulge region of galactic longitude, l = ±30° and galactic latitude between b = ±(3.3° and 15°). Nearly half of these catalogue objects lack any radial velocity measurements, and a fair number needed to be re-observed because of poor spectral resolution in the original measurements. We decided to make new velocity measures of this sub-sample in order to obtain a uniform quality sample. This is important because we then know the error of the measurements and, for many cases, we can reduce the velocity error.

We took advantage of the fact that the spectroscopic data is so easy to obtain in order to cover a more extended region (l = ±30° and b = ±(3.3° and 15°)) than our Optical Imaging Survey (l = ±20° and b = −5° to −10°). This extra data will serve to investigate the behaviour of the kinematics as we move away from the bulge beyond galactic longitude l = ±15°. This may be important for the detection of a lens around the galactic bar and for studying the transition from bulge to disk. The spatial distribution of our PNe, even in the zone b = −5° to −10°, is probably affected by galactic absorption. However, the determination of the mean motion and velocity dispersion is not greatly influenced by foreground absorption, and therefore one can use the existing spatially non-uniform database to improve the statistical significance of the velocity data.

In this chapter, we describe the entire procedure followed in order to obtain velocities of our 97 new candidates and the subsample of PNe from the Acker catalogue. We first describe the observations, then move on to the data reduction techniques, followed by the lines measurement and summarize with the radial velocities.

3.1 Observations

Using the 74-inch (188 cm) telescope at Mount Stromlo Observatory, we obtained spectra for the 97 new H_α objects detected in our 1.0m telescope imaging survey and for 317 of the 326 PNe from the Acker catalogue in the region l = ±30° and b = ±(3.3° to 15°).

We used the Boller and Chivens spectrograph with the 600 l mm^{-1} grating blazed at λ 7500 Å in first order and the GEC 385 x 578 UV coated CCD. The spectrograph slit width was 2 arcsec. This CCD has a pixel size of 22.5μ and a readout noise of 10. We binned the CCD with a factor 3 along the slit and a factor 1 in λ. The grating was set to have a wavelength coverage from λ 6200 Å to λ 6800 Å . A GG 475 filter in the beam was used to cut off light from the second order blue. This setup gave a wavelength scale of about 1 Å pixel^{-1} (50 km s^{-1}).

When possible, we took two spectra for each object in order to discriminate against cosmic rays and to determine our measurement error. Typical exposure

Table 3.1: Observing log for the 74-inch Optical Spectroscopy Survey.

Date	No. of nights	Clear nights
18-25 June 1993	8	40%
9-18 July 1993	10	50%
6-13 June 1994	8	40%
30 June - 7 July 1994	8	15%
2-7 May 1995	6	30%
22-25 May 1995	4	20%
22 June 1995	1	100%
26 June - 2 July 1995	7	30%
31 July - 7 Aug 1995	8	55%
18-27 Aug 1995	10	70%

times varied from 50 to 900 seconds. Each object spectrum was sandwiched between two comparison lamp (NeFe) exposures in order to provide a wavelength calibration.

In three observing seasons, we were allocated a total of 70 nights at the 74-inch telescope, 45% of which were clear. The observing log is summarized in Table 3.1. Column 1: the period covered in each observing run, Column 2: the number of nights per run and Column 3: the proportion of clear nights per run.

3.2 Data reduction

The data reduction for the spectra is straightforward. We again used the IRAF environment to correct for electronic bias and illumination variation across the chip (Massey *et al.*, 1992). Details of the complete procedure is given in §2.3 of this thesis. We note however that the flatfields were obtain using a continuum lamp instead of twilight flatfields. Having removed the detector signature, we proceeded to correct the spectra for geometrical distortions, such as slit curvative and tilt. Throughout the correction procedure, we have used the *long-slit* analysis from the **noao.twodspec.longslit** packages.

On a 2-D array, we define the dispersion axis as the axis along the stellar spectrum and the spatial axis as the perpendicular axis. In order to correct for geometrical distortions, we first need to identify where the PN spectrum lies along the slit. Usually, we find it very close to the center. Then, we define three windows along the dispersion axis, one for the PN spectrum and two, on each side of the PN spectrum, for the sky background. The background windows will be used for sky subtraction.

Table 3.2: Summary of the classification for the 97 new candidates.

Objects	Counts
PN	53
Prob. PN	3
Symb. star	14
Prob. Symb. star	3
dMe	3
CV?	1
Spurious	20

When we observed the PNe, we took comparison spectra of the NeFe lamp between the two PNe exposures. We identified the lines in these comparison spectra using the tasks **identify** and **reidentify**. A *spline3* function was used with *order=1*. In this step, we mainly mark each line with its wavelength value so that we later get a transformation from pixels to wavelengths. Then, using the task **fitcoords**, we fit a two-dimensional function in x and y (*chebyshev*: xorder $\approx$ 6 and yorder $\approx$ 6). This task allow us to display the transformation in (x, y, residuals), therefore allowing us better control in interactive fitting mode. At this stage, we have the transformation from pixels to wavelength. Using the task **transform**, we apply the solution to our PN spectrum; the result is a linearized spectrum.

The final step toward obtaining a 1-D spectrum is extracting the spectrum and subtracting its background. To remove the skylines, which may interfere with the spectrum of faint objects, we used the task **background** with the *chebyshev* function and an *order=1*. To extract the 1-D spectrum, we used the **scopy** task with *nsum* set to a few columns.

At this point, we are able to distinguish true or probable PNe from other kind of objects on the criteria that a PN has narrow H_α emission with possibly other emission lines from [NII] and [SII] and a symbiotic star shows broad H_α emission with possibly emission in HeI. Table 3.2 summarizes the final count of our 97 new candidates. Column 1: the classification of objects and Column 2: the number of objects in each class. The second object (mentioned in Chapter 2) which did not appear in the [OIII] surveyed fields shows characteristics of a symbiotic star and therefore will be catalogued as such.

3.3 Line measurements

All 1-D spectra are then processed through the **splot** task in order to measure the wavelength of the emission lines. A *spline3* function with *order=1* was applied

Table 3.3: Rest wavelength values of emission lines.

[NII]	H_α	[NII]	[HeI]	[SII]	[SII]
λ6548.1 Å	λ6562.7 Å	λ6583.4 Å	λ6678.4 Å	λ6716.4 Å	λ6730.8 Å

for the wavelength transformation of each emission line. The rest wavelengths (λ_o) of emission lines likely to be found in our wavelength window (from λ6200 Å to λ6800 Å) are shown in Table 3.3.

The radial velocity of each object is calculated using

$$V_r = c \frac{\lambda - \lambda_o}{\lambda_o}$$

where λ is the observed wavelength of the line, λ_o is its rest wavelength and c is the speed of light.

If more than one line was identified and measured for a given spectrum, we then applied a weight factor according to the strength of each line:

$$\langle V_r \rangle = \frac{\Sigma\, f_i\, v_{r,i}}{\Sigma\, f_i}$$

where f_i is the flux of a line and $v_{r,i}$ its corresponding radial velocity. For PN where we took two spectra, we then can calculate the mean velocity for each object from the two measurements.

As mentioned earlier, there were 193 catalogue PNe with published radial velocities. Figure 3.1 show a comparison of our velocity values against the catalogued velocities. Apart from a few outliers, we find good agreement with the catalogued values.

3.4 IRAS Search

We also performed a cross-check of our new PNe positions with the IRAS[1] Point Source Catalogue (PSC) and found a match for 11 objects. Figure 3.2 show an overplot of our objects in the IRAS color-color diagram from Pottasch (1987) reproduced in Acker *et al.* (1992). Our objects are the filled circles and we see that most of them do not lie in the region occupied by most PNe in this diagram. We have 2 PNe which are located in the HII-OH/IR star regions, one in the PNe region, 4 in the OH/IR star-galaxies region, one in the PNe-galaxies region and 3 in an empty region above the OH/IR stars.

Therefore, relatively few of our new PNe are seen at IRAS wavelengths, and those that were seen have colors which would not have led to their selection as PN

[1]InfraRed Astronomical Satellite, 1984

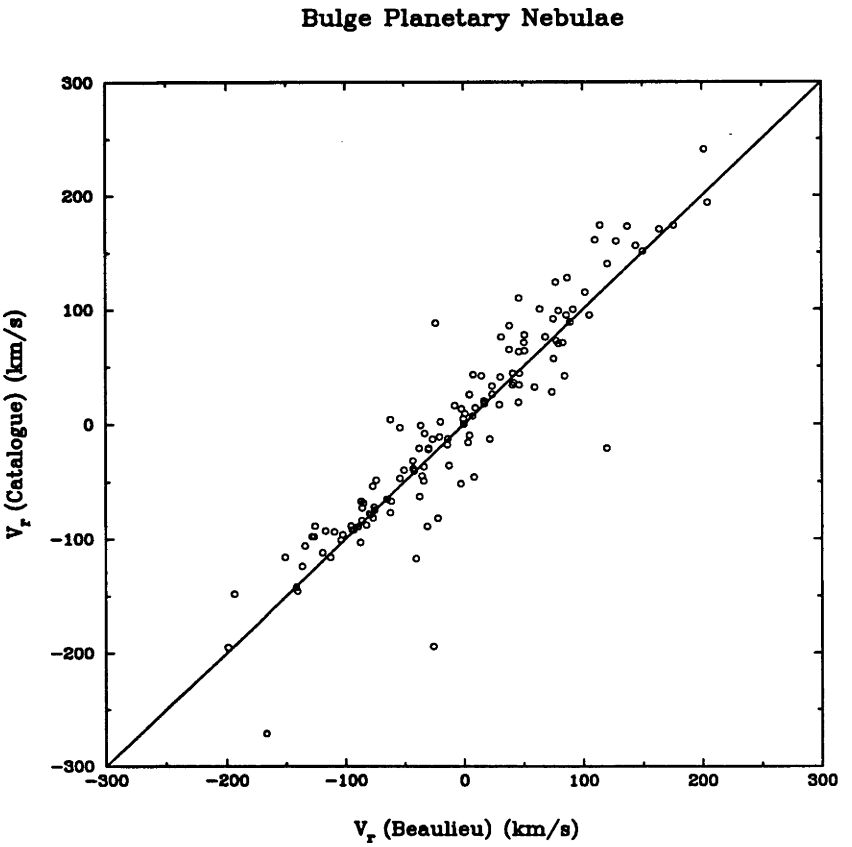

Figure 3.1: Comparison between the velocity values obtain from the 74-inch telescope and the catalogued values.

candidates. This is quite unexpected. The reason for most of these new objects to lie so far away from the PNe region is not clear. These objects include a mixture of compact and extended PNe, and there is no evidence for any correlation between their IRAS color, angular diameter and position on the longitude-velocity diagram.

3.5 Summary of the results

Table 3.4 lists our new PNe. Column 1: the name of the new PN, Column 2: the (l,b) coordinates, Column 3: the (α, δ) coordinates in J2000.0, Column 4: comments for each PN, Column 5: the mean radial velocity corrected for heliocentric motion, Column 6: the difference in velocities between our two spectra when two were available, Column 7: the IRAS detection from the Point Source Catalogue (when applicable) and Column 8: the IRAS number.

Object SB17 (011.1–07.9) is classified as "Possible planetary nebula : V 348 Sgr" in the Acker *et al.* (1992) Catalogue. Our spectrum show strong H_α, [NII] and [SII] lines, indicating that this object is in fact a PN.

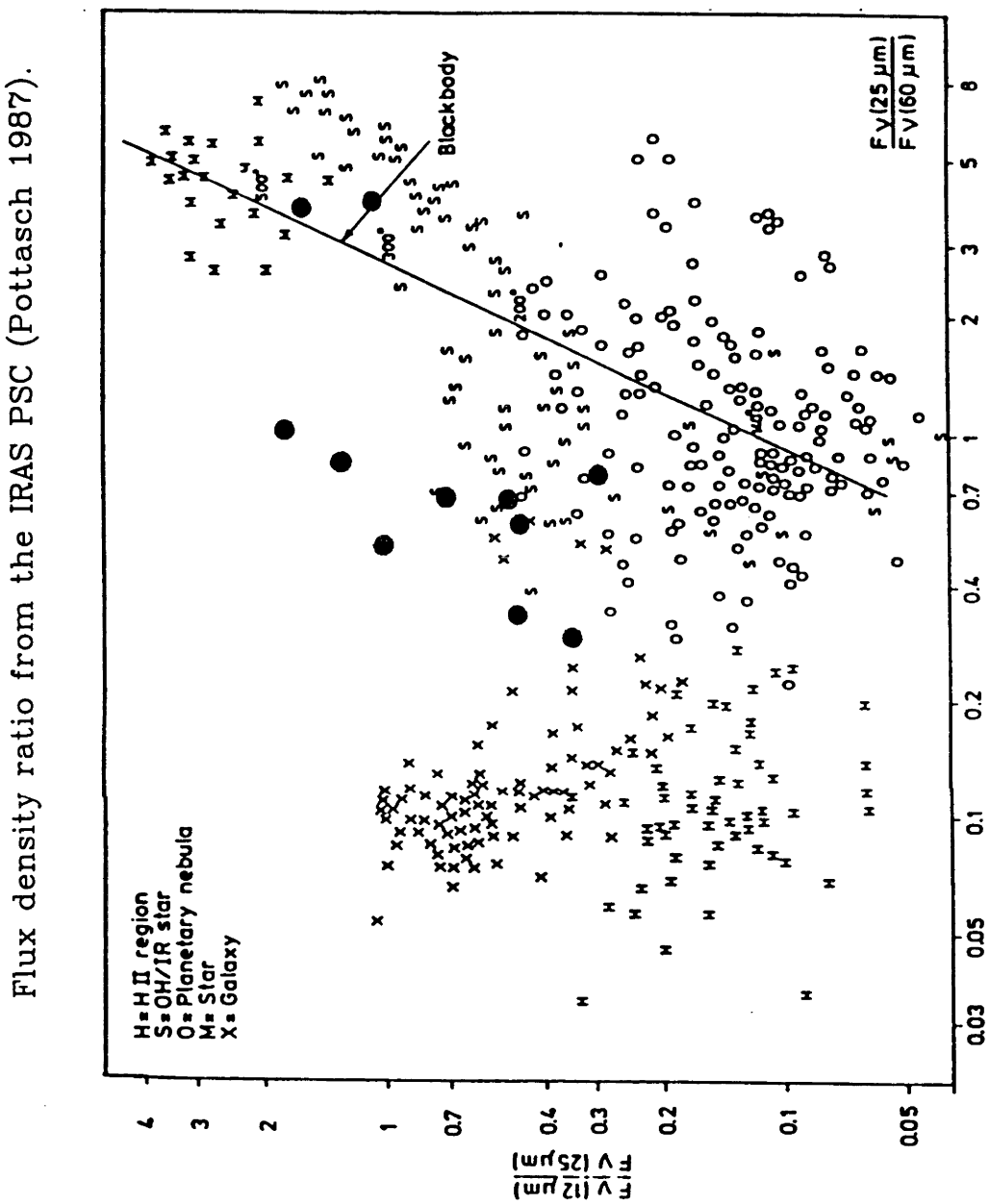

Figure 3.2: Newly discovered PNe, which have a match in the IRAS/PS Catalogue, overlayed on the color-color diagram from Pottasch (1987). Our 11 matchs are the filled circles.

Table 3.5 contains our velocity data for the 317 PNe from the Acker catalogue. Column 1: the name of the PN, Column 2: the heliocentric radial velocity value reported in the catalogue, Column 3: our mean heliocentric radial velocity value and Column 4: the velocity difference between our two spectra when two were available.

Table 3.6 gives the IRAS flux values for each objects found in the IRAS/PS Catalogue. Column 1: the name of the new PN, Column 2: the (l, b) coordinates, Column 3: the (α, δ) coordinates in J2000.0, Columns 4, 5, 6 and 7: the far IR flux density at 12, 25, 60 and 100 μm in Jy respectively and Column 8: the IRAS flux quality, where 1 = upper limit, 2 = moderate quality, and 3 = good quality.

Table 3.4: Final list of the newly discovered PNe.

Object	PN G $lll.l \pm bb.b$	Coords J2000.0 $\alpha^h\ ^m\ ^s\ \ \delta^\circ\ '\ ''$	Comments	$V_r(helio)$ $km\ s^{-1}$	$v_1 - v_2$ $km\ s^{-1}$	IRAS detection	IRAS source
SB1	000.1–08.0	18 18 48.4 -32 47 56.5	PN	-54	-5		
SB2	000.5–05.3	18 08 34.7 -31 06 52.1	PN	3	0		
SB3	000.7–06.1	18 12 14.4 -31 19 58.9	PN	68	0		
SB4	001.1–06.4	18 14 14.1 -31 11 09.2	PN	21	-8		
SB5	001.3–05.6	18 11 15.2 -30 37 48.9	PN	-31	6		
SB6	001.6–05.9	18 13 15.5 -30 26 04.6	PN	31	2		
SB7	003.3–06.1	18 17 46.1 -29 06 04.9	PN opt. thin	-27	-2		
SB8	004.2–05.2	18 15 50.3 -27 48 59.7	PN	40	-5		
SB9	004.6–09.9	18 35 42.4 -29 38 22.2	PN opt. thin	-22			
SB10	004.7–05.5	18 18 06.9 -27 31 35.4	PN	54			
SB11	005.2–05.9	18 20 44.7 -27 15 48.0	PN	95	-20	yes	172497
SB12	005.4–06.1	18 21 55.1 -27 09 46.2	PN opt. thin	25			
SB13	006.5–05.8	18 23 00.0 -26 05 17.1	PN probable	57	27		
SB14	007.7–05.3	18 23 42.4 -24 47 26.2	PN opt. thin	31			
SB15	009.3–06.5	18 31 14.7 -23 58 03.2	PN probable	165	4		
SB16	009.4–05.6	18 28 21.1 -23 25 28.0	PN	61	8		
SB17	011.1–07.9	18 40 19.9 -22 54 29.9	PN (V 348 Sgr)	145		yes	181973
SB18	011.4–07.3	18 38 43.3 -22 24 15.0	PN opt. thin	-2	30		
SB19	014.4–06.1	18 39 39.9 -19 14 12.5	PN opt. thin	72		yes	181710
SB20	014.8–08.4	18 49 24.3 -19 52 15.6	PN opt. thin	-24	4		

continues ...

Object	PN G $lll.l \pm bb.b$	Coords J2000.0 $\alpha^h\ ^m\ ^s\quad \delta^\circ\ '\ ''$	Comments	$V_r(helio)$ $km\ s^{-1}$	$v_1 - v_2$ $km\ s^{-1}$	IRAS detection	IRAS source
SB21	016.0–07.6	18 48 11.4 -18 29 39.8	PN opt. thin (+ star)	66		yes	185736
SB22	016.7–07.3	18 48 30.5 -17 43 56.5	PN opt. thin	-10			
SB23	017.5–07.4	18 50 13.7 -17 02 27.6	PN opt. thin	52	4		
SB24	017.5–09.2	18 57 16.6 -17 50 49.1	PN opt. thin	22			
SB25	341.0+09.4	16 13 38.1 -37 59 57.9	PN	-93	13		
SB26	341.7–06.0	17 21 02.8 -47 35 25.8	PN opt. thin	-154	-25		
SB27	341.9+08.8	16 19 13.9 -37 47 30.5	PN probable	-2	-8		
SB28	342.3–06.0	17 22 52.5 -47 02 45.3	PN	-27		yes	145844
SB29	343.7–09.6	17 45 33.4 -47 43 49.7	PN opt. thin	-88	-5	yes	155474
SB30	343.9–05.8	17 27 02.2 -45 32 39.7	PN opt. thin	67	9		
SB31	347.9–06.0	17 40 03.5 -42 24 02.6	PN opt. thin	-70	23	yes	153025
SB32	349.7–09.1	17 59 26.9 -42 24 52.3	PN	186			
SB33	351.2–06.3	17 50 27.7 -39 40 17.3	PN	-58	24		
SB34	351.5–06.5	17 52 09.6 -39 32 16.0	PN opt. thin	-57	-3	yes	158612
SB35	351.7–06.6	17 53 02.7 -39 24 08.8	PN opt. thin	-120	-8		
SB36	352.0–06.7	17 54 20.6 -39 10 39.8	PN opt. thin	35	-13		
SB37	352.6–04.9	17 47 52.7 -37 48 03.4	PN opt. thin	20		yes	156740
SB38	352.7–08.4	18 03 28.9 -39 21 26.8	PN opt. thin	59	4		
SB39	353.3–08.3	18 04 31.8 -38 47 36.8	PN opt. thin	6			
SB40	354.7–07.2	18 02 55.6 -37 08 15.3	PN opt. thin	-69	-2		

continues ...

Object	PN G $lll.l \pm bb.b$	Coords J2000.0 $\alpha^h\ ^m\ ^s\ \ \delta^\circ\ '\ ''$	Comments	$V_r(helio)$ $km\ s^{-1}$	$v_1 - v_2$ $km\ s^{-1}$	IRAS detection	IRAS source
SB41	354.7–10.0	18 15 39.1 -38 27 56.4	PN opt. thin	34	-1		
SB42	355.3–07.5	18 05 52.5 -36 45 35.9	PN	40	52		
SB43	355.8–08.7	18 12 23.7 -36 52 50.9	PN	-74	-4		
SB44	356.0–07.4A	18 07 07.6 -36 02 52.8	PN opt. thin	1	3	yes	165874
SB45	356.0–07.4B	18 06 52.2 -36 06 41.2	PN opt. thin	-116	2		
SB46	356.1–08.6	18 12 39.7 -36 31 51.3	PN opt. thin	54	2		
SB47	356.3–07.3	18 07 21.3 -35 45 43.8	PN	-27	0		
SB48	356.4–06.8	18 05 14.3 -35 28 07.4	PN opt. thin	10	-2		
SB49	357.2–09.8	18 20 09.4 -36 07 25.3	PN opt. thin	20	-10		
SB50	357.3–06.5	18 06 08.2 -34 33 31.1	PN opt. thin	0	35		
SB51	357.4–07.2	18 09 16.1 -34 47 41.0	PN	-222	-14		
SB52	358.3–07.3	18 11 39.9 -34 00 22.6	PN opt. thin	-49	-16		
SB53	358.7–05.1	18 03 28.4 -32 37 25.6	PN opt. thin	-14	-6		
SB54	359.3–06.0	18 08 31.3 -32 29 54.4	PN opt. thin	38			
SB55	359.4–08.5	18 19 26.4 -33 37 07.5	PN opt. thin	163		yes	171836
SB56	359.9–07.4	18 15 32.4 -32 38 01.5	PN opt. thin	222	-31		

Table 3.5: Radial velocities for the Acker Catalogue objects

PN G $lll.l \pm bb.b$	$V_r(cat)$ $km\ s^{-1}$	$V_r(helio)$ $km\ s^{-1}$	$v_1 - v_2$ $km\ s^{-1}$	PN G $lll.l \pm bb.b$	$V_r(cat)$ $km\ s^{-1}$	$V_r(helio)$ $km\ s^{-1}$	$v_1 - v_2$ $km\ s^{-1}$
000.0–06.8	-84	-86		002.5–05.4	107	90	
000.1–05.6		-70	-4	002.6–03.4	241	202	25
000.2–04.6		117	-17	002.6+04.2		-174	1
000.3–04.6	-17	-29		002.6+08.1	2	-20	17
000.3+06.9	-46	9		002.7–04.8	-92	-93	
000.3+12.2	-33	-36		002.9–03.9		33	-19
000.7–03.7	-54	-77	-5	002.9+06.5		70	6
000.7+04.7		40	-5	003.1+03.4	87	80	6
000.7–07.4	-21	-30		003.2–04.4	124	77	2
000.8–07.6		33	-9	003.2–06.2	100	64	
000.9–04.8	-156	-155	-4	003.3–04.6	152	157	-19
001.2–03.9		-92	31	003.3–07.5	32	59	-2
001.4–03.4	-117	-40	9	003.4–04.8	-21	120	
001.4+05.3	36	42		003.5–04.6	-20	-3	
001.5–06.7	-19	-12		003.7–04.6	174	115	
001.7–04.4	-52	-3	7	003.7+07.9		41	-27
001.7–04.6	-106	-134		003.8+05.3	-59	-88	
001.7+05.7	34	40		003.9–14.9	-65	-65	
001.8–03.8		-222	13	004.0–05.8		159	-32
002.0–06.2	-112	-119		004.0–11.1	50	39	
002.0–13.4	19	22	3	004.1–03.8	-63	-38	-1
002.1–04.2	-116	-151	-14	004.2–04.3		-5	3
002.2–06.3	-1	-36		004.2–05.9	57	75	
002.2–09.4	-30	-44		004.5+06.8		-180	-25
002.3–03.4		-158	-1	004.6+06.0	160	151	
002.3–07.8	-82	-22		004.7–11.8		115	7
002.4–03.7	-70	-92	-4	004.8–05.0	-10	5	21
002.4+05.8	-101	-104		004.9+04.9	26	24	

continues ...

PN G $lll.l \pm bb.b$	$V_r(cat)$ $km\ s^{-1}$	$V_r(helio)$ $km\ s^{-1}$	$v_1 - v_2$ $km\ s^{-1}$	PN G $lll.l \pm bb.b$	$V_r(cat)$ $km\ s^{-1}$	$V_r(helio)$ $km\ s^{-1}$	$v_1 - v_2$ $km\ s^{-1}$
004.9–04.9	-75	-107		007.9+10.1		-45	55
005.0–03.9		-122	-3	008.0+03.9	16	-8	-7
005.0+04.4	17	30	8	008.1–04.7	71	83	
005.1–08.9		56	3	008.2–04.8	157	119	
005.2+04.2		132	-6	008.2+06.8		23	10
005.2+05.6	18	17		008.3–07.3	194	205	
005.5–04.0		-53	-5	008.4–03.6	84	70	3
005.6–04.7	17	53	10	008.6–07.0		26	3
005.7–03.6		-91	8	008.8+05.2	44	47	
005.7–05.3	-72	-76		009.0+04.1	-18	-32	1
005.8+05.1	-56	-62		009.3+04.1		16	-4
005.8–06.1	73	78		009.4–05.0	14	10	
006.0–03.6	157	136	12	009.4–09.8	46	50	
006.1+08.3	92	75		009.6+10.5		30	-31
006.2–03.7	123	118	-2	009.6–10.6	174	176	
006.3+04.4	-116	-113	-3	009.6+14.8	-48	-40	
006.4–04.6		47	31	009.8–04.6	-13	22	
006.8–03.4		89	9	010.4+04.5	-21	-46	7
006.8+04.1	100	92	6	010.7–06.4	-145	-141	
006.8–08.6		72	-37	010.7–06.7		-84	-3
007.0–06.0	42	85		010.7+07.4		116	-20
007.0+06.3	-7	-26		011.0–05.1	-72	-69	
007.0–06.8	115	102		011.0+05.8	-94	-109	
007.5+04.3	-108	-134	2	011.0+06.2	4	-33	
007.5+07.4	13	-2		011.1+07.0		-81	31
007.6+06.9	-65	-66		011.1+11.5	86	38	
007.8–03.7	70	79	2	011.3–09.4	-21	3	
007.8–04.4	161	110	11	011.7–06.6	-22	-30	7

continues ...

PN G $lll.l \pm bb.b$	$V_r(cat)$ $km\ s^{-1}$	$V_r(helio)$ $km\ s^{-1}$	$v_1 - v_2$ $km\ s^{-1}$	PN G $lll.l \pm bb.b$	$V_r(cat)$ $km\ s^{-1}$	$V_r(helio)$ $km\ s^{-1}$	$v_1 - v_2$ $km\ s^{-1}$
011.9+04.2	-73	-86	-9	021.1–05.9	26	5	-2
012.2+04.9		43	7	021.2–03.9		-11	-1
012.5–09.8	34	41		022.5+04.8		24	-3
013.0–04.3		81	24	023.0+04.3		119	16
013.1+04.1	-37.3	-60	-24	023.3–07.6		54	-41
013.4–03.9	140.0	121	3	024.1+03.8	89	90	-1
013.7–10.6		37	3	024.2–05.2	19	46	4
013.8–07.9		42	13	024.2+05.9	-21	-38	1
014.0–05.5		-42	16	024.3–03.3		1	-10
014.2–07.3	-89	-95		025.0–11.6		-10	
014.3–05.5		-29	25	025.3–04.6		-85	15
014.6–04.3	27	5	3	025.4–04.7	-36	-13	2
014.7–11.8		20		025.9–10.9		96	-2
014.9+06.4		-5		027.3–03.4		28	-5
015.4–04.5	63	46	2	027.4–03.5	110	47	9
015.9+03.3	128	87	11	027.6+04.2	95	105	58
016.0–04.3	-41	-42	-2	027.6–09.6	151	150	-1
016.0+13.5		10	-3	028.0+10.2		49	-10
016.1–04.7	88	-24		028.2–04.0		65	11
017.6–10.2	23	3		028.5+05.1	42	15	10
017.9–04.8	71	51		028.7–03.9		-20	7
018.9+03.6	28	31	-2	029.2–05.9	-39	-43	-1
018.9+04.1	-16	4	-5	029.8–07.8		89	-4
019.4–05.3	41	31		330.2+05.9		-33	-3
019.4–13.6		-37	-13	330.6–03.6	-89	-89	3
019.7–04.5	76	88		330.7+04.1		-9	6
019.8+05.6		86	4	330.9+04.3		27	0
020.7–05.9		46	-7	331.1–05.7		-52	-74

continues ...

PN G $lll.l \pm bb.b$	$V_r(cat)$ $km\ s^{-1}$	$V_r(helio)$ $km\ s^{-1}$	$v_1 - v_2$ $km\ s^{-1}$	PN G $lll.l \pm bb.b$	$V_r(cat)$ $km\ s^{-1}$	$V_r(helio)$ $km\ s^{-1}$	$v_1 - v_2$ $km\ s^{-1}$
331.4–03.5	33	24	-18	341.8+05.4	37	36	
331.5–03.9	-18	-14	0	342.1+10.8	7	7	
332.0–03.3	-77	-62	8	342.5–14.3	46	43	
332.3–04.2	64	51	6	342.8–06.6	-88	-82	
332.9–09.9		-67	1	342.9–04.9	-38	-19	
333.4–04.0		-88	11	343.4+11.9		67	-17
334.3–09.3	44	41	0	343.5–07.8		-142	-7
334.8–07.4		-77	-7	343.6+03.7	-194	-26	-14
335.2–03.6		-97	9	344.2+04.7	-142	-142	9
335.4+09.2		-62	4	344.4–06.1		-35	3
335.6–04.0		24	-7	344.8+03.4		-131	-4
335.9–03.6		-85	-2	345.0+03.4		32	0
336.2–06.9	-49	-34	-5	345.0+04.3		15	-17
336.3–05.6	-67	-87	4	345.0–04.9	-78	-80	
336.8–07.2		8	-3	345.2–08.8	-83	-94	
336.9+08.3		-159	0	345.3–10.2		21	-16
336.9–11.5		-14		345.5+15.1		-19	6
337.4–09.1		-101	-2	345.6+06.7	-32	-43	
337.5–05.1		52	3	346.0+08.5	-83	-93	
337.6–04.2		-96	0	346.2–08.2	-49	-74	
338.1–08.3	9	1		346.3–06.8	35	17	
338.8+05.6	-27	-61	-9	346.9+12.4	-13	-14	
340.4–14.1		-279	-16	347.4+05.8	-102	-101	-14
340.8+10.8		9	21	348.0+06.3		-52	-5
340.8+12.3		-79	22	348.0–13.8	-124	-136	
340.9–04.6		-2	-9	348.4–04.1		-208	-16
341.5–09.1		-25	-17	348.8–09.0		-53	-19
341.6+13.7	-103	-87		349.2–03.5		-12	-2

continues ...

PN G $lll.l \pm bb.b$	$V_r(cat)$ $km\ s^{-1}$	$V_r(helio)$ $km\ s^{-1}$	$v_1 - v_2$ $km\ s^{-1}$	PN G $lll.l \pm bb.b$	$V_r(cat)$ $km\ s^{-1}$	$V_r(helio)$ $km\ s^{-1}$	$v_1 - v_2$ $km\ s^{-1}$
349.3–04.2		13	2	355.9+03.6	-148	-193	-13
349.8+04.4	-184	-186	0	355.9–04.2	-98	-127	-5
350.1–03.9	-37	-34	-5	356.1–03.3		-165	-7
350.5–05.0	-45	-35		356.2–04.4	-271	-167	13
350.9+04.4	-20	-25	14	356.3–06.2	-47	-54	
351.0–10.4		-38	0	356.5–03.6		-37	-2
351.1+04.8	-40	-51	37	356.5–03.9	-50	-117	-8
351.2+05.2	-98	-128		356.5+05.1		-48	-19
351.3+07.6		8	-10	356.6–07.8		-19	10
351.6–06.2	-16	-28		356.7–04.8	76	68	
351.7–10.9		-58	24	356.7–06.4		-206	-5
351.9+09.0		-74	10	356.8+03.3	330	168	0
352.0–04.6	-8	-33		356.8–05.4	-195	-199	
352.1+05.1	27	26		356.8–11.7		-60	-6
352.9–07.5	5	0	-9	356.9+04.4	-156	-170	-10
352.9+11.4		-2	-16	356.9+04.5	78	51	2
353.2–05.2		-151	1	356.9–05.8	173	137	
353.3+06.3	-89	-126		357.1+03.6	-191	-208	-8
353.7+06.3	-56	-56		357.1+04.4		52	-1
353.7–12.8		-50	-9	357.1–04.7	76	31	
354.2+04.3	-75	-75	-5	357.1–06.1	24	11	
354.4–07.8		-124	0	357.2–04.5	-79	-79	7
354.5+03.3		-165	4	357.2+07.4	156	144	
354.9+03.5		-72	19	357.3+03.3	-69	-132	
355.1–06.9	-69	-85	-9	357.3+04.0		76	-16
355.4–04.0		-84	-10	357.4–03.5	-3.0	-54	9
355.7–03.4		38	10	357.4–04.6	-92	-94	
355.7–03.5	160	128	8	357.6–03.3		114	2

continues ...

PN G $lll.l \pm bb.b$	$V_r(cat)$ $km\ s^{-1}$	$V_r(helio)$ $km\ s^{-1}$	$v_1 - v_2$ $km\ s^{-1}$	PN G $lll.l \pm bb.b$	$V_r(cat)$ $km\ s^{-1}$	$V_r(helio)$ $km\ s^{-1}$	$v_1 - v_2$ $km\ s^{-1}$
357.9–03.8		-32	1	358.9+03.4	65	38	5
357.9–05.1	2	-5		358.9–03.7	99	80	10
358.0–05.1		-132	-7	359.0–04.1	-11	-21	3
358.0+07.5	43	8		359.0–04.8	20	17	
358.0+09.3		-8	0	359.1+15.1		2	-5
358.2+03.5	50	51	-16	359.2+04.7		-237	42
358.2+03.6	-96	-102	5	359.3+03.6		-49	-5
358.2+04.2	95	86	-4	359.4–03.4		107	-12
358.4+03.3		122		359.6–04.8		-108	6
358.5+03.7		-168	-1	359.7–04.4	200	213	
358.5–04.2	-13	-26	18	359.8+03.7	-93	-117	17
358.5+05.4	4	-62		359.8+05.2	-89	-31	
358.5–07.3	-30	-30		359.8+05.6	73	76	
358.6–05.5	34	46		359.8+06.9	-67	-61	
358.6+07.8	12	6		359.8–07.2	-49	-74	
358.7–05.2	28	74		359.9–04.5	170	164	2
358.7+05.2	37	45		359.9+05.1	-82	-77	
358.8+04.0		33	8	359.9–05.4	-19	19	
358.8+04.1		46	12				

Table 3.6: Results from the IRAS search for the newly discovered PNe.

Object	PN G	Coords J2000.0	F12	F25	F60	F100	FQuality
	$lll.l \pm bb.b$	$\alpha^h\ ^m\ ^s\ \ \delta^\circ\ '\ ''$	Jy	Jy	Jy	Jy	
SB11	005.2–05.9	18 20 44.7 -27 15 48.0	4.8	2.9	0.7	4.1	3321
SB17	011.1–07.9	18 40 19.9 -22 54 29.9	5.5	3.0	2.9	13.4	3331
SB19	014.4–06.1	18 39 39.9 -19 14 12.5	0.3	0.5	1.4	26.7	1331
SB21	016.0–07.6	18 48 11.4 -18 29 39.8	0.3	0.5	0.7	15.1	1331
SB28	342.3–06.0	17 22 52.5 -47 02 45.3	0.4	0.3	0.7	29.9	3111
SB29	343.7–09.6	17 45 33.4 -47 43 49.7	3.4	2.9	0.7	2.3	3311
SB31	347.9–06.0	17 40 03.5 -42 24 02.6	0.3	0.9	1.1	24.9	1331
SB34	351.5–06.5	17 52 09.6 -39 32 16.0	0.3	0.8	2.4	18.1	1331
SB37	352.6–04.9	17 47 52.7 -37 48 03.4	0.3	0.7	1.1	9.1	1311
SB44	356.0–07.4A	18 07 07.6 -36 02 52.8	0.5	0.4	0.5	3.6	3111
SB55	359.4–08.5	18 19 26.4 -33 37 07.5	0.3	0.5	0.8	10.3	1331

Chapter 4

The Catalogue

This Catalogue presents the finding charts and spectrum for each new and probable planetary nebula discovered during this study. It is arranged in the following manner:

4.1 Part I : Newly discovered Planetary Nebulæ

Each page is a montage of the H_α (upper image) and the continuum (lower image) of a newly-found planetary nebula. North is up and east is at the left. Most objects are centered (or nearly centered) in the image and are identified by a cross. Some objects were not centered because they lie near the edge of the original image. For those objects, if there was a lack of clarity, an arrow was added to the continuum image where the object would most likely be. Each image is 181 pixels on a side (with 2.35 arcsec pixel^{-1}). A 2 arcmin bar is shown on the right-hand side of the H_α image. The newly-found planetary nebulæ are ordered by increasing galactic number and are identified following the designation system, PN *Glll.l* $\pm$ *bb.b*, which has been adopted by Acker *et al* (1992). On the right-hand side is the spectrum associated with the object.

For a few PNe, some comments are needed:

- 001.6–05.9: an arrow was added to the continuum image
- 003.3–06.1: on the H_α image, the cross indicate the position of the new object and the arrow points to a catalogued object, 003.2–06.2.
- 014.8–08.4: there is a ghost object on the NE quadrant of the continuum image, produced by a bright star (outside of this frame).

Table 4.1 gives information about the position and size of the PNe on the H_α chart. The size in pixels is an eye estimate of the optical dimensions of the PN and represents the EW size x NS size.

4.2 Part II : The 2.3m Observations

In June 1995, 25 of our new PNe were observed at the 2.3m telescope of Siding Spring Observatory. We present the H_α images as a complement to our Catalogue. The focal-reducing imager at the Nasmyth B f/18 focus was used with a Tek 1024 CCD. The H_α filter is a Bausch and Lomb 3-cycle 90mm diameter (λ_{peak} = 6586 Å and FWHM = 16 Å) and was tilted at an angle of 7° in order to obtain the central wavelength for H_α λ6562 Å .

There are 5 H_α images per page. North is up and east is at the left. Most objects are centered (or nearly centered) in the image and are identified with an arrow only if there was a lack of clarity. Each image is 181 pixels on a side with 0.6 arcsec pixel^{-1}.

Table 4.1: Positions and angular sizes of the newly discovered PNe.

Object	PN G *lll.l* ± *bb.b*	Center pixels	Size pixels	Object	PN G *lll.l* ± *bb.b*	Center pixels	Size pixels
SB1	000.1–08.0	91,92	12x12	SB29	343.7–09.6	92,91	3x3
SB2	000.5–05.3	91,92	10x10	SB30	343.9–05.8	90,91	6x6
SB3	000.7–06.1	91,90	20x24	SB31	347.9–06.0	90,90	7x7
SB4	001.1–06.4	91,91	12x12	SB32	349.7–09.1	90,91	8x8
SB5	001.3–05.6	110,91	8x8	SB33	351.2–06.3	90,92	11x11
SB6	001.6–05.9	91,93	11x10	SB34	351.5–06.5	91,92	11,11
SB7	003.3–06.1	89,90	6x6	SB35	351.7–06.6	90,91	6x6
SB8	004.2–05.2	90,91	9x9	SB36	352.0–06.7	90,91	5x5
SB9	004.6–09.9	92,91	6x4	SB37	352.6–04.9	90,90	5x5
SB10	004.7–05.5	91,91	20x20	SB38	352.7–08.4	90,100	5x5
SB11	005.2–05.9	92,90	3x3	SB39	353.3–08.3	91,90	47x47
SB12	005.4–06.1	92,91	4x3	SB40	354.7–07.2	92,91	11x8
SB13	006.5–05.8	89,92	13x16	SB41	354.7–10.0	91,91	10x10
SB14	007.7–05.3	91,89	8x8	SB42	355.3–07.5	90,91	10x10
SB15	009.3–06.5	92,91	7x6	SB43	355.8–08.7	90,91	19x19
SB16	009.4–05.6	90,94	14x16	SB44	356.0–07.4A	90,91	7x11
SB17	011.1–07.9	91,91	9x7	SB45	356.0–07.4B	90,91	9x9
SB18	011.4–07.3	92,92	6x6	SB46	356.1–08.6	90,91	6x6
SB19	014.4–06.1	91,92	8x8	SB47	356.3–07.3	90,92	11x11
SB20	014.8–08.4	91,91	11x13	SB48	356.4–06.8	89,77	6x6
SB21	016.0–07.6	92,91	9x9	SB49	357.2–09.8	90,93	6x6
SB22	016.7–07.3	91,91	4x3	SB50	357.3–06.5	91,91	9x9
SB23	017.5–07.4	92,91	6x6	SB51	357.4–07.2	90,90	20x20
SB24	017.5–09.2	91,91	8x8	SB52	358.3–07.3	90,91	6x8
SB25	341.0+09.4	91,90	8x8	SB53	358.7–05.1	89,91	5x8
SB26	341.7–06.0	90,90	5x5	SB54	359.3–06.0	89,91	15x12
SB27	341.9+08.8	92,90	6x6	SB55	359.4–08.5	89,91	12x12
SB28	342.3–06.0	90,91	3x3	SB56	359.9–07.4	90,92	4x3

Part I : The Finding Charts and Spectra

PN G000.1−08.0

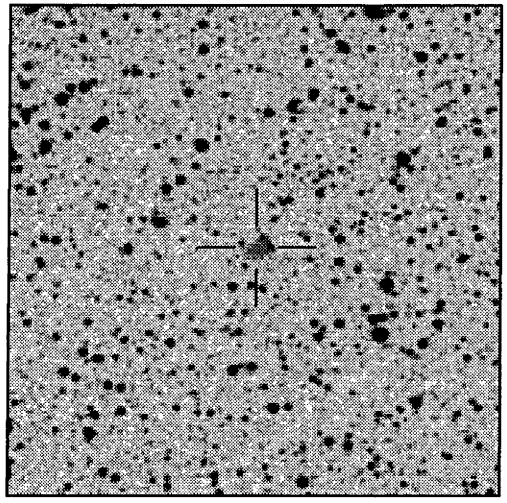

H_α

Cont

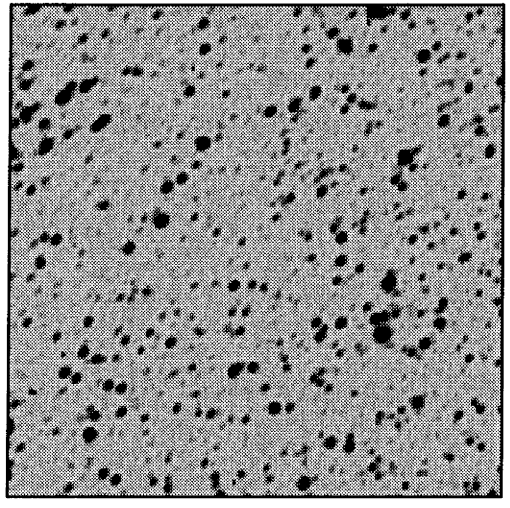

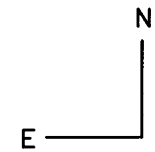

2'

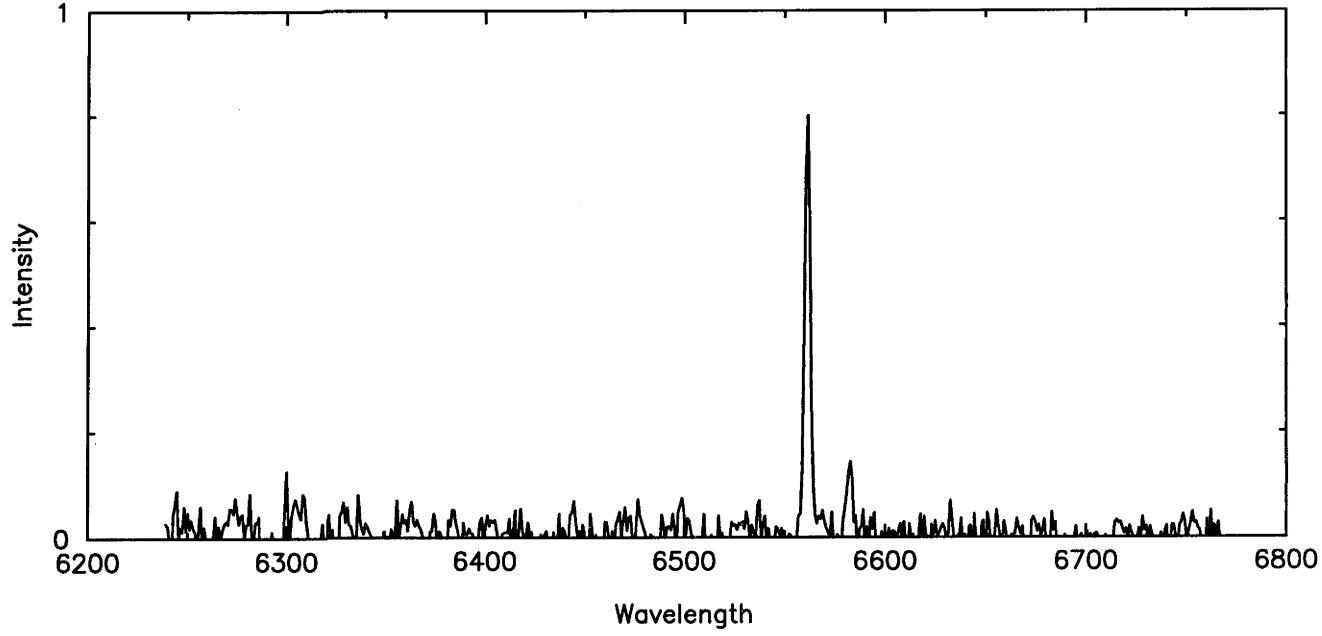

PN G000.5−05.3

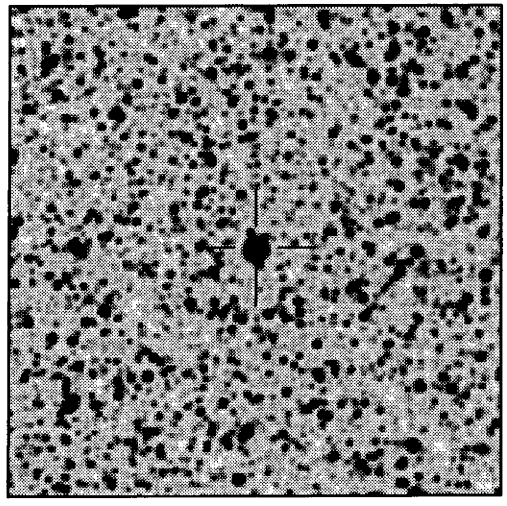

H_α

Cont

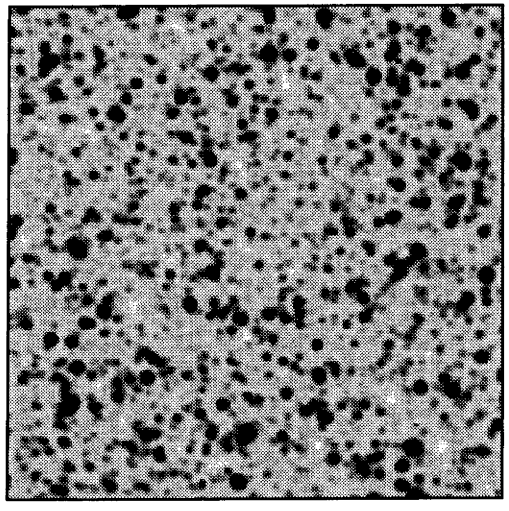

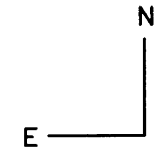

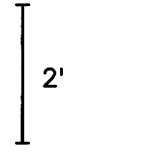

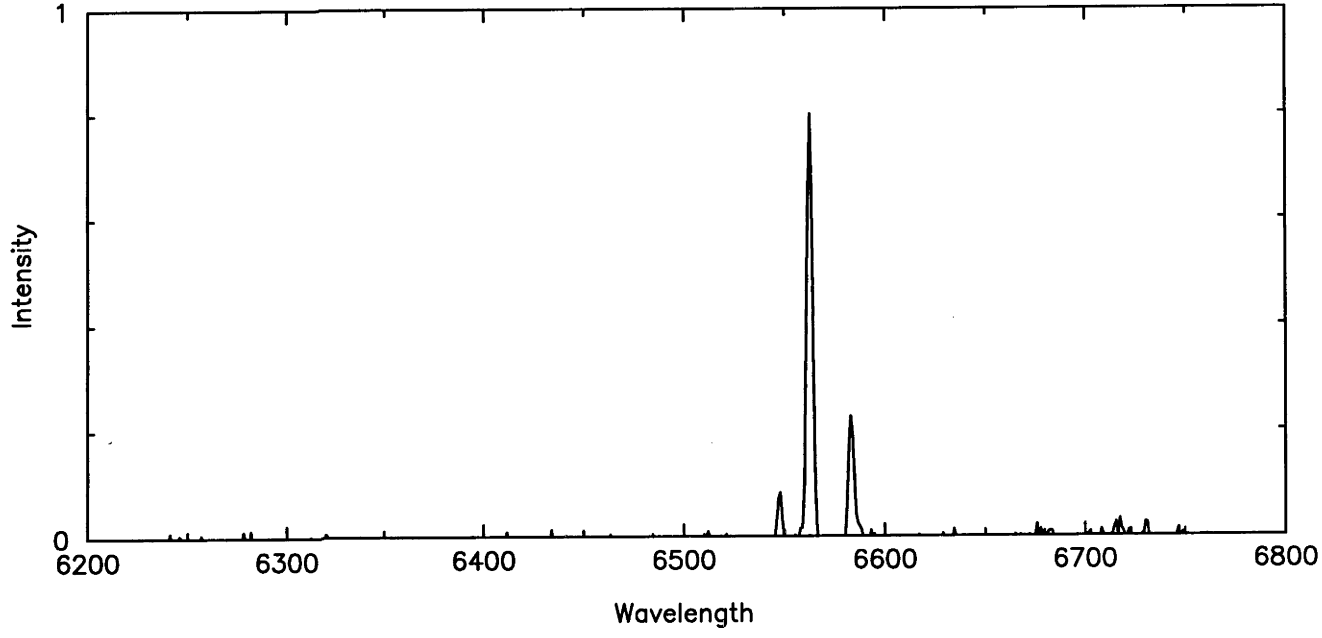

PN G000.7−06.1

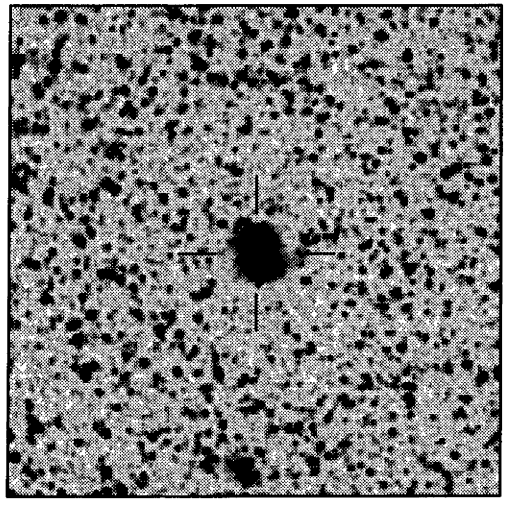

H_α

Cont

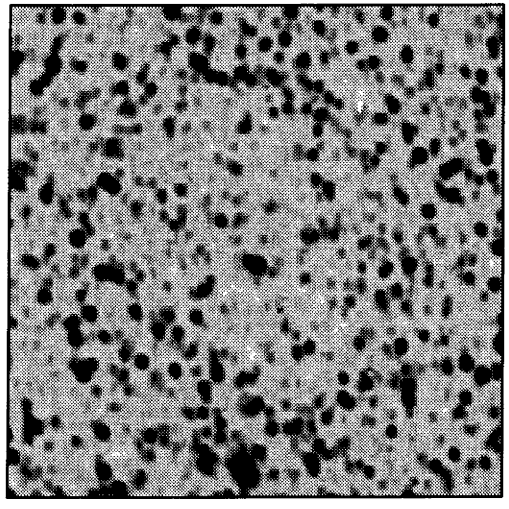

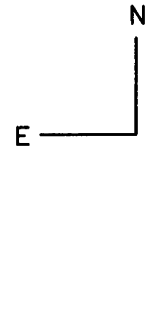

2'

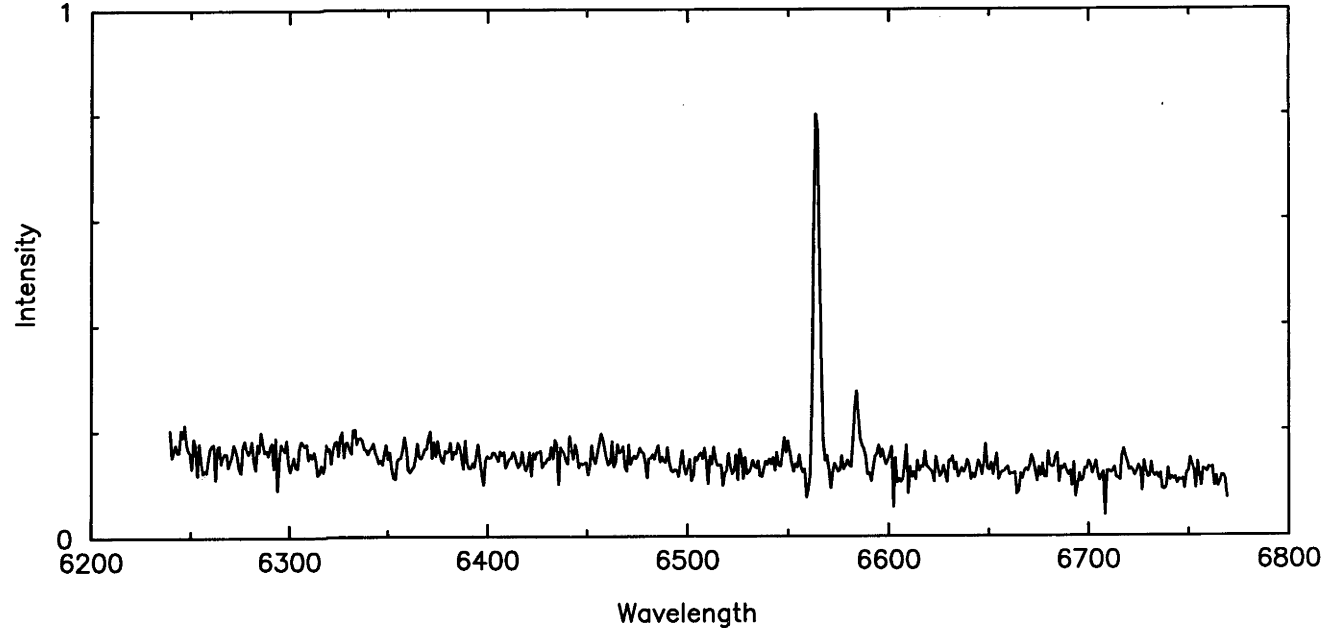

PN G001.1−06.4

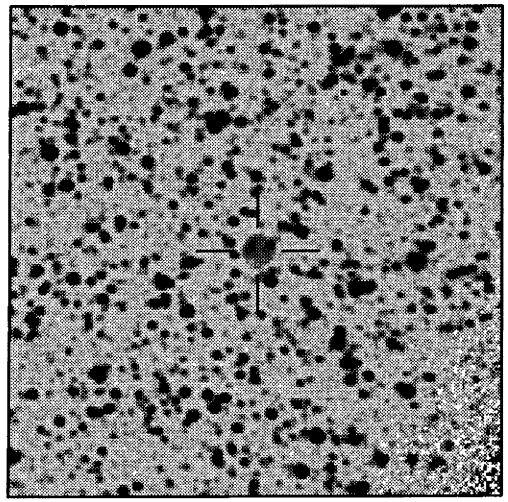

H_α

Cont

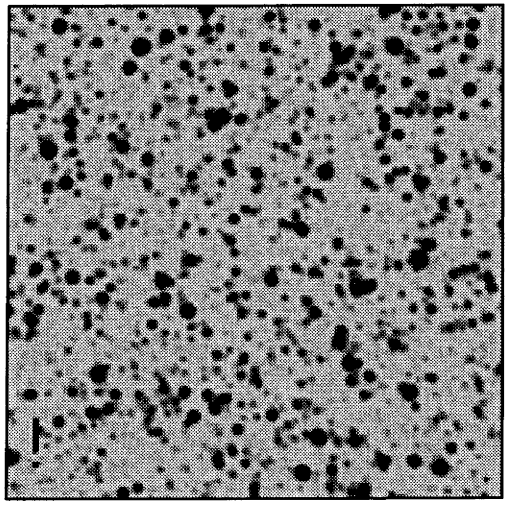

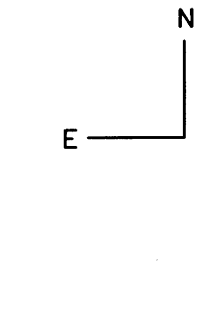

2'

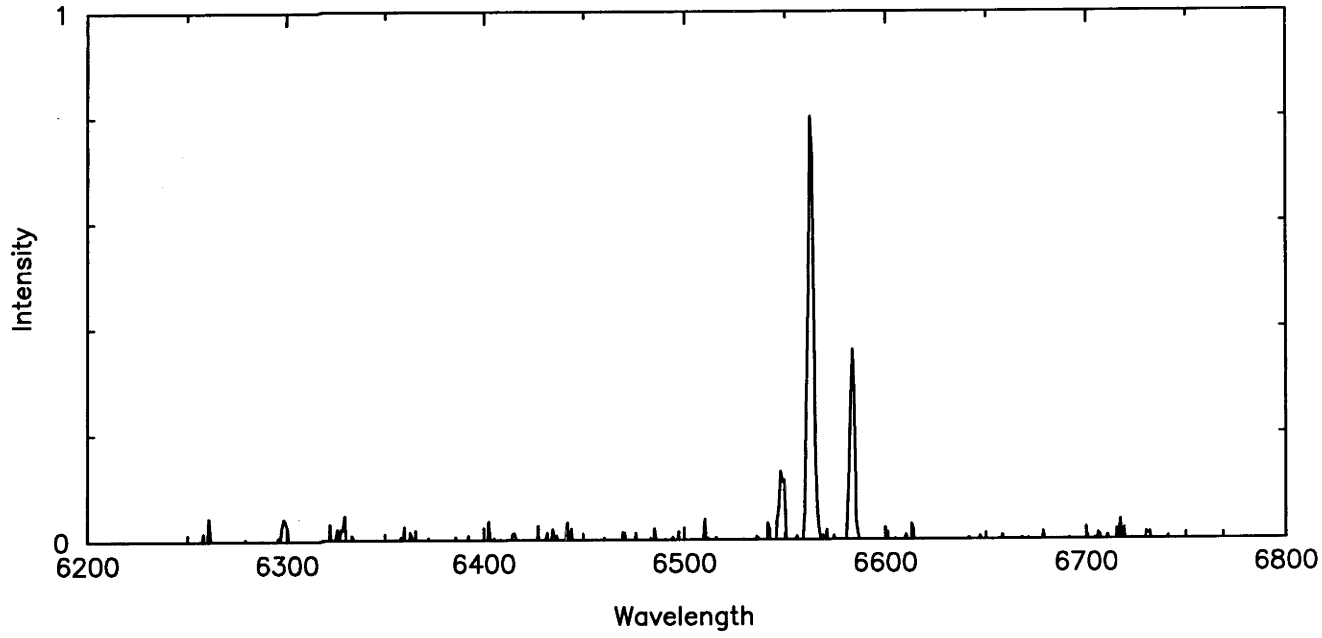

PN G001.3−05.6

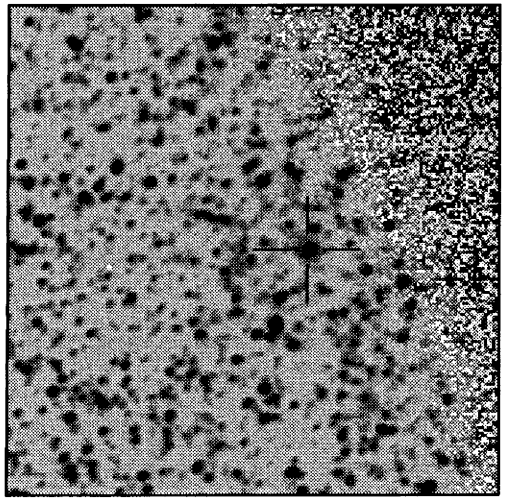

H_α

Cont

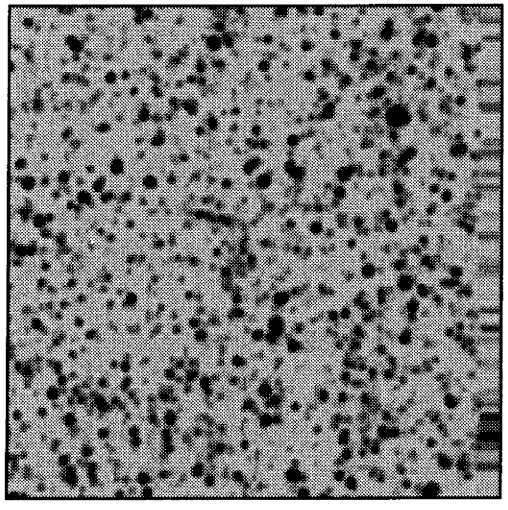

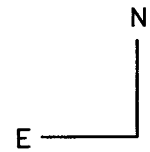

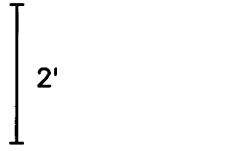

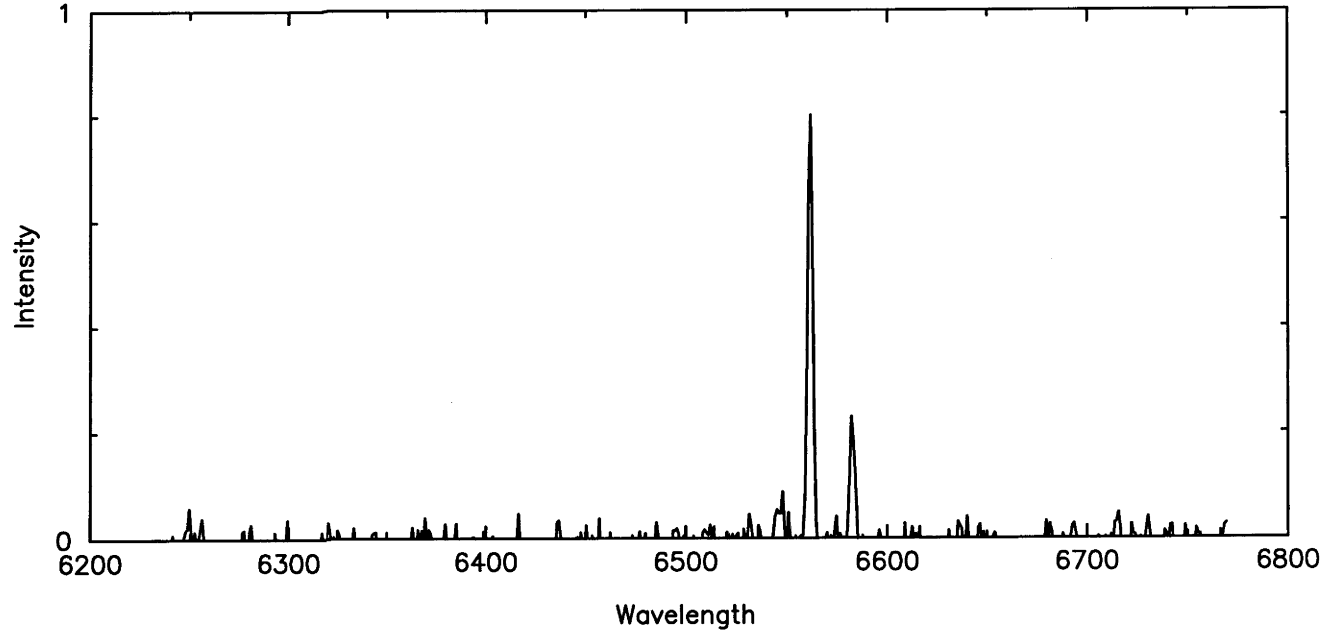

PN G001.6−05.9

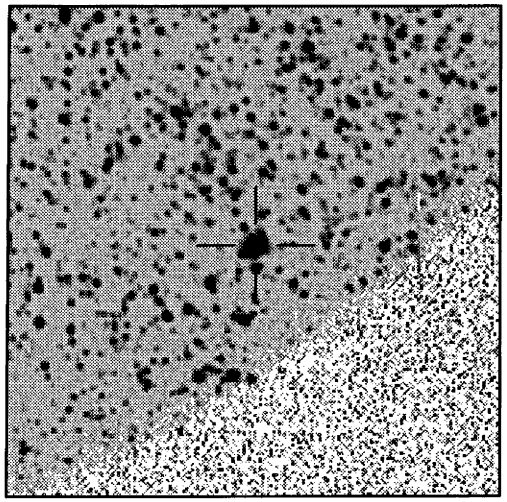

H_α

Cont

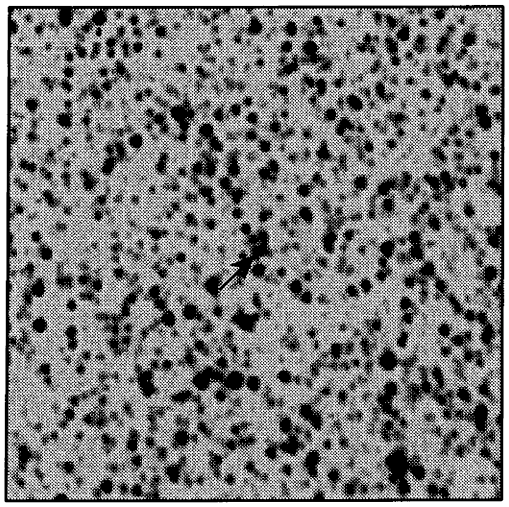

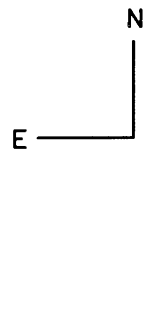

2'

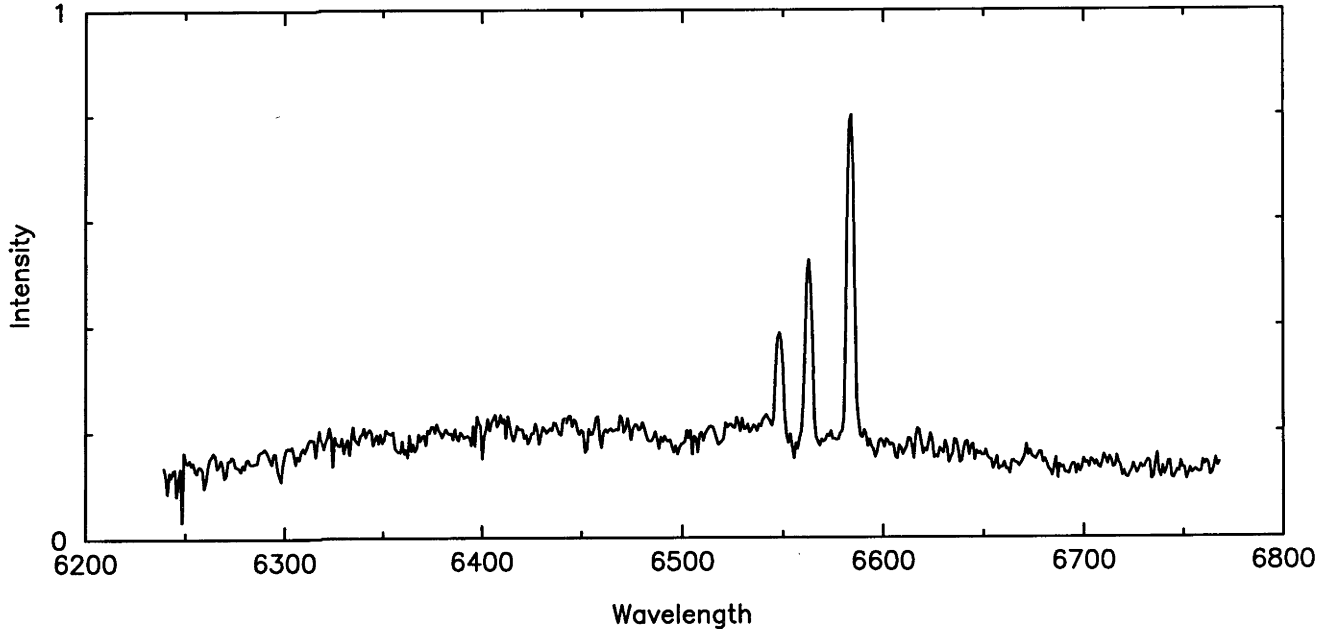

PN G003.3−06.1

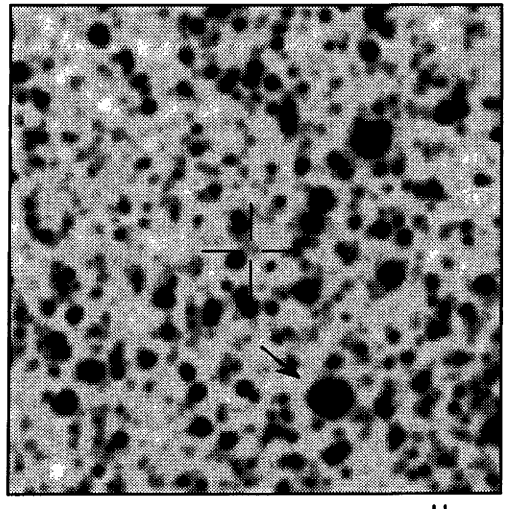

H_α

Cont

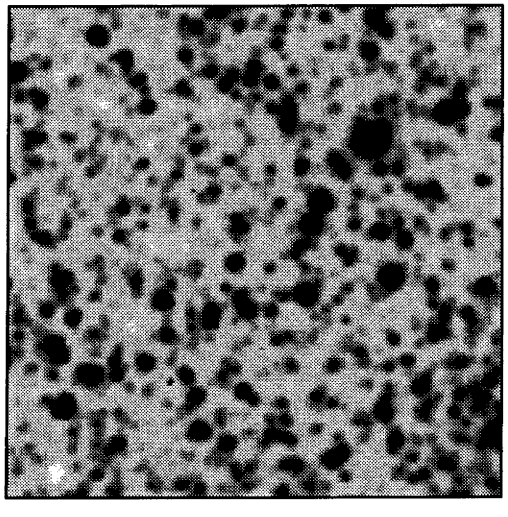

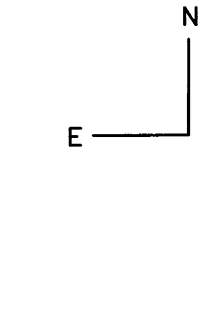

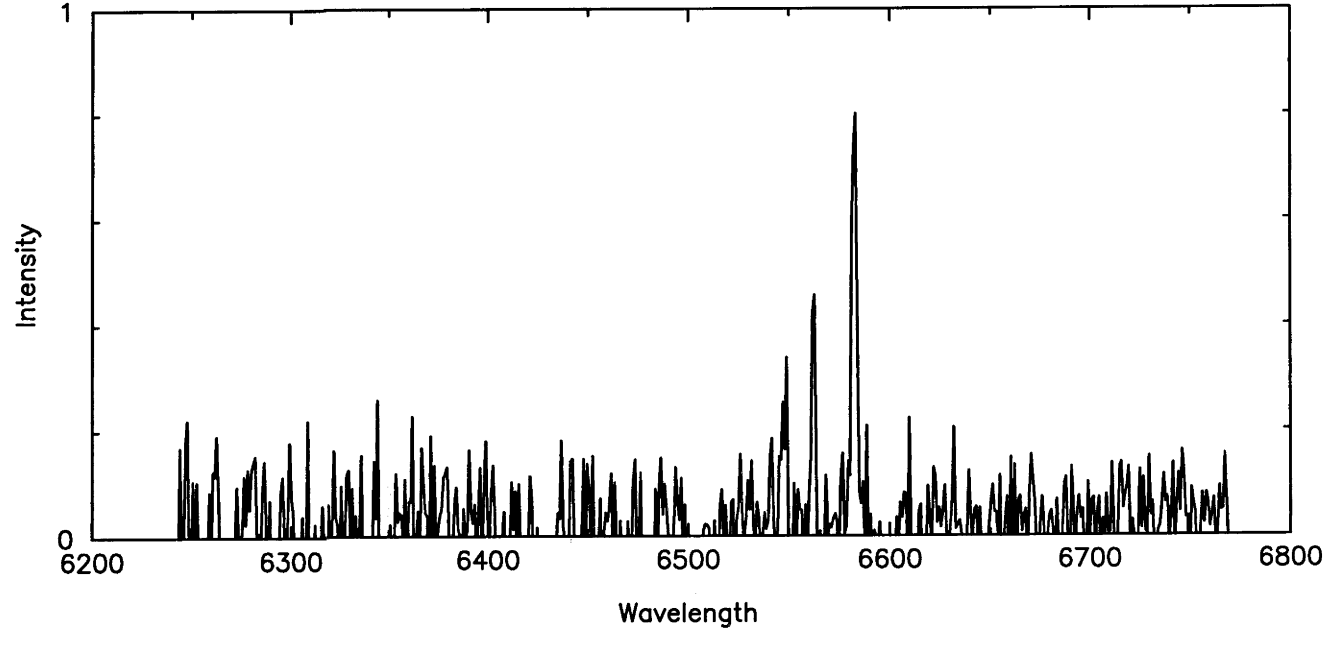

PN G004.6−09.9

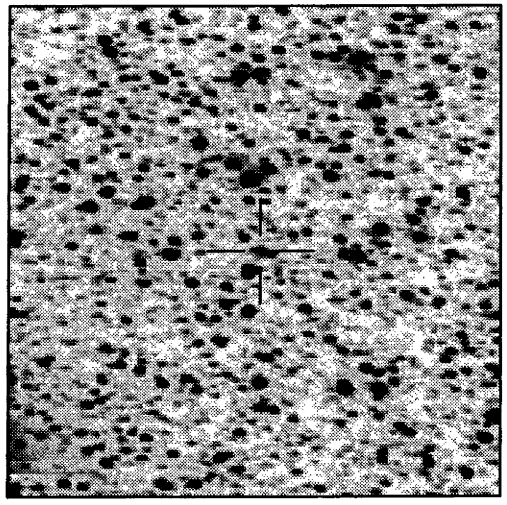

H_α

Cont

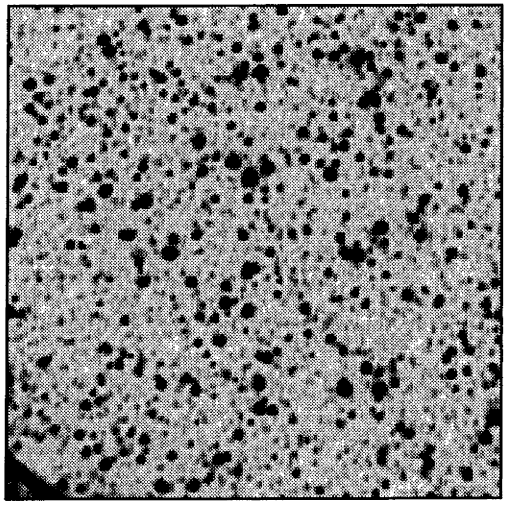

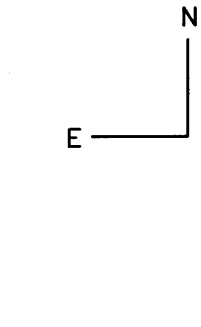

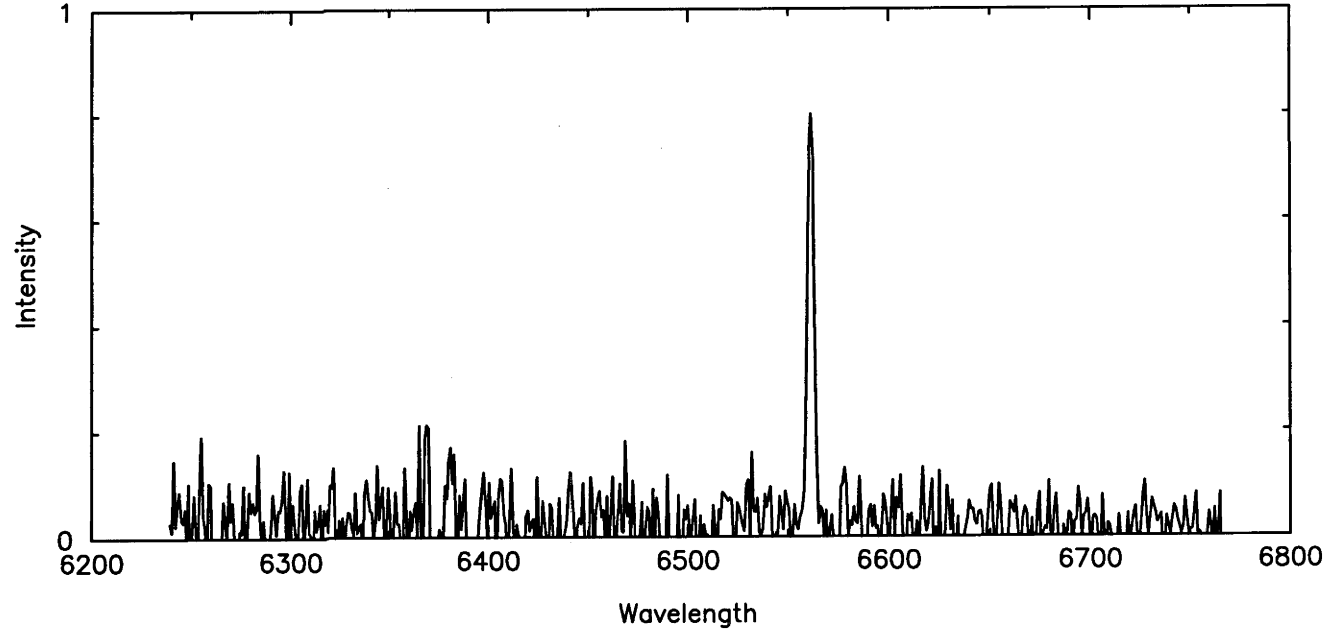

PN G004.7−05.5

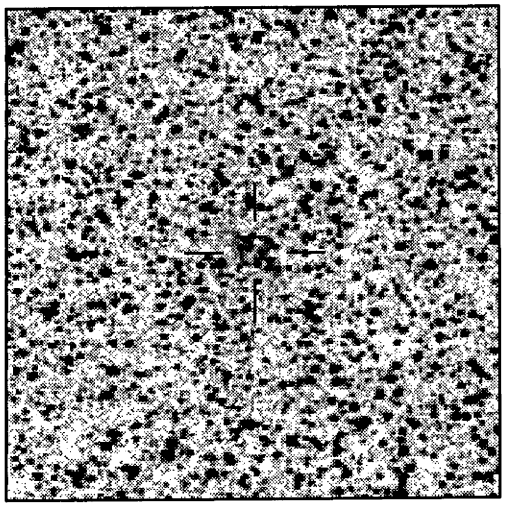

H_α

Cont

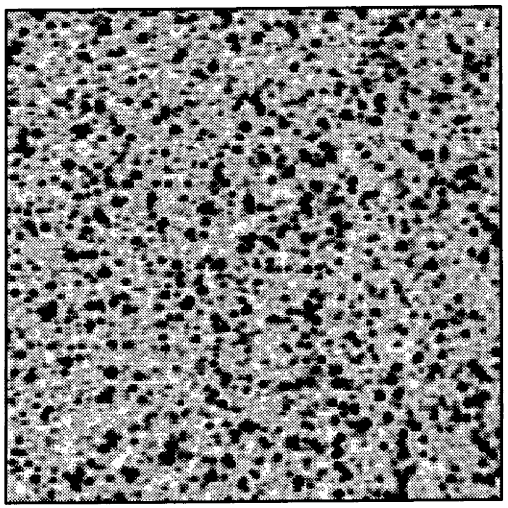

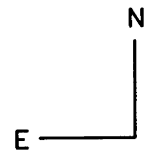

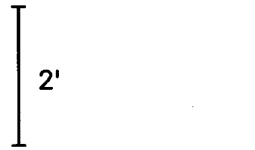

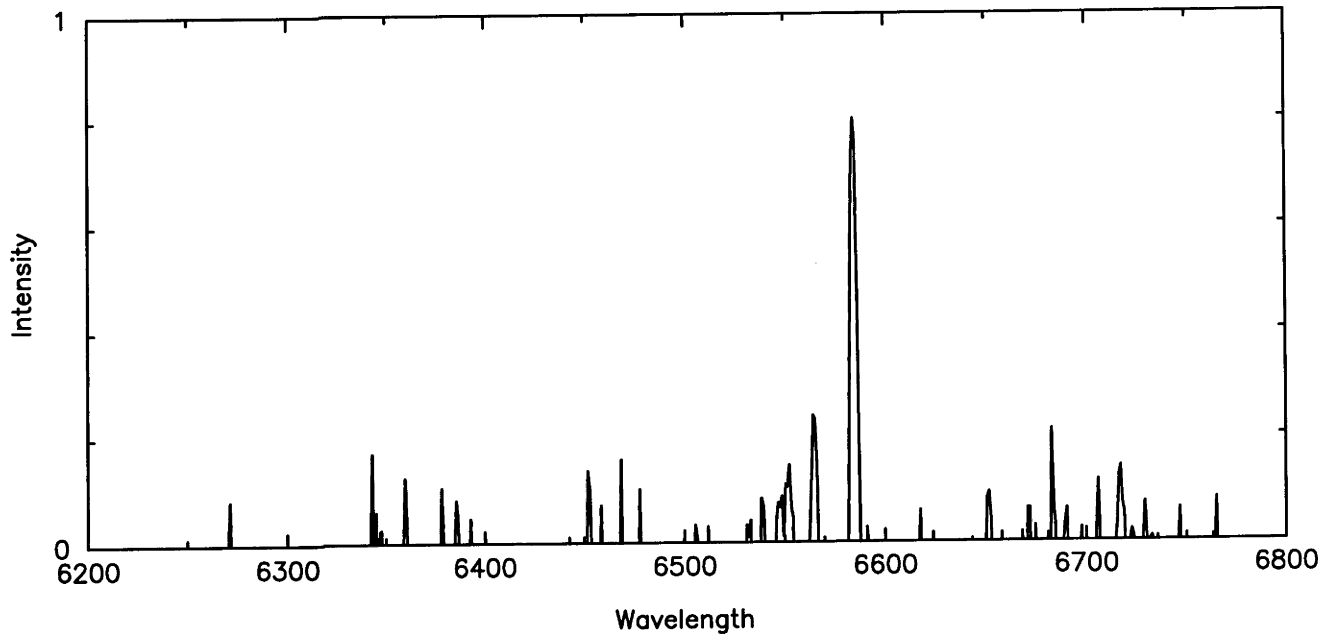

PN G005.2−05.9

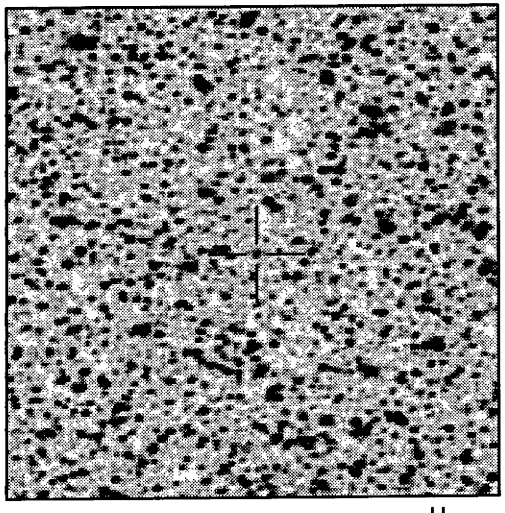

H_α

Cont

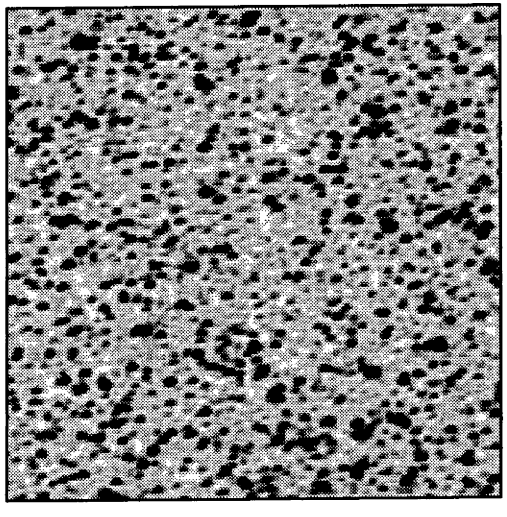

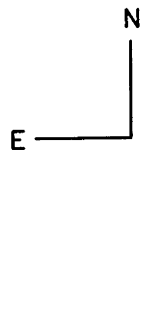

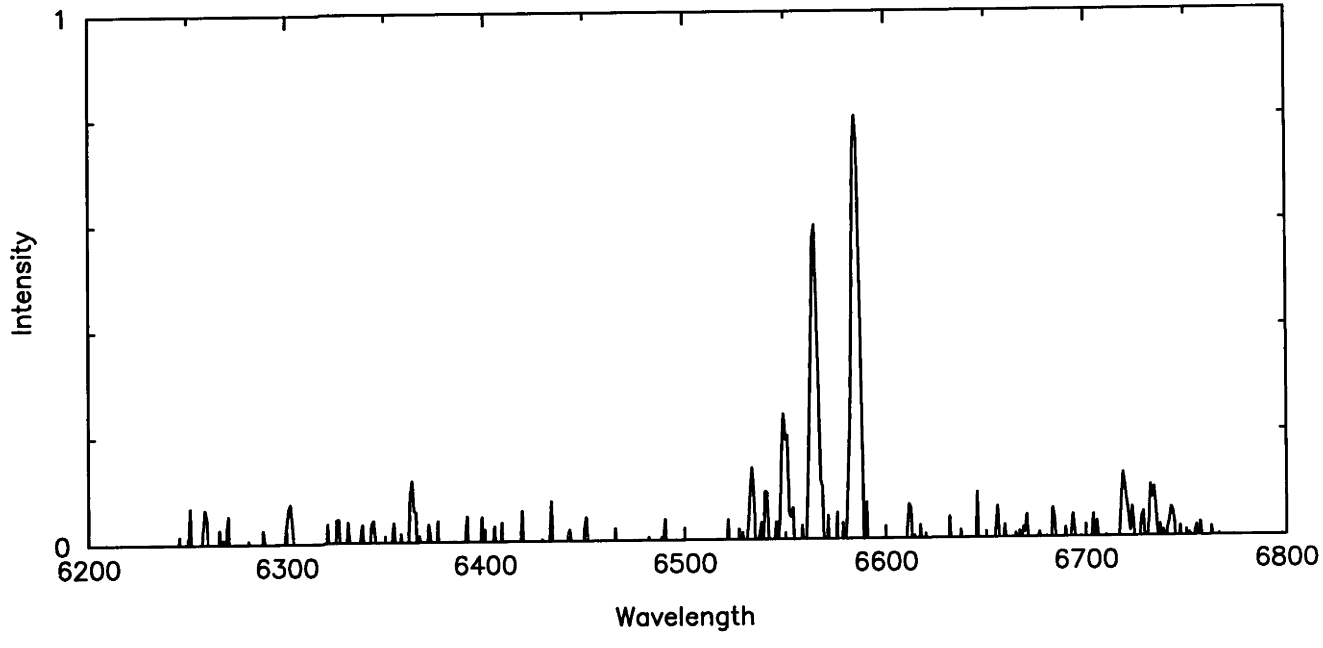

PN G005.4−06.1

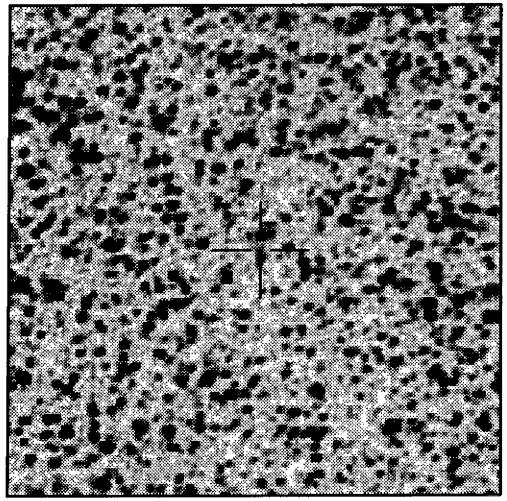

H_α

Cont

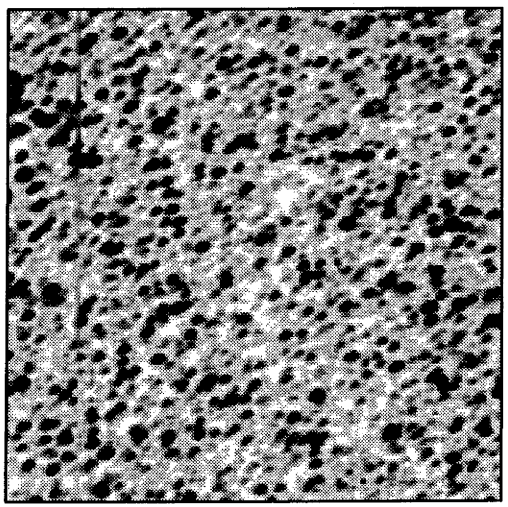

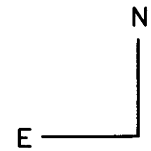

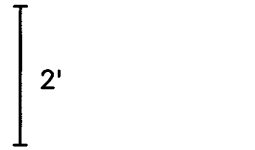

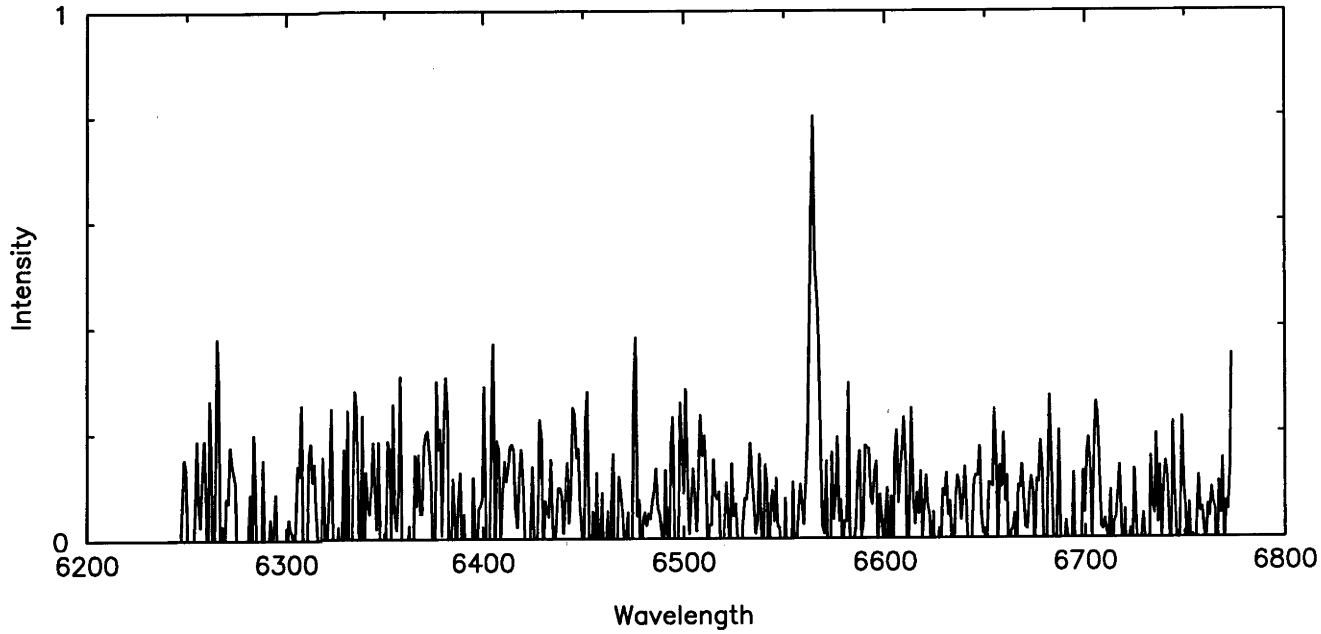

PN G006.5−05.8

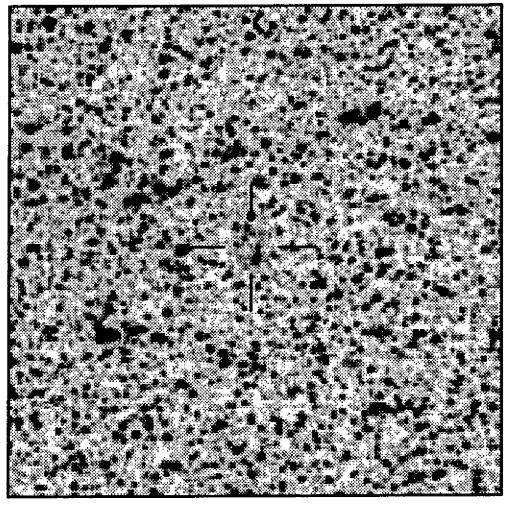

H_α

Cont

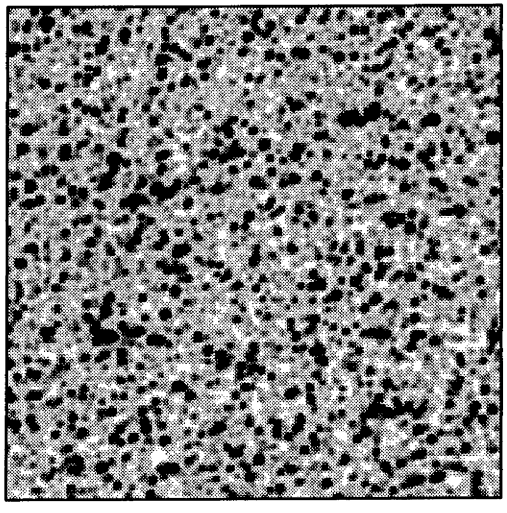

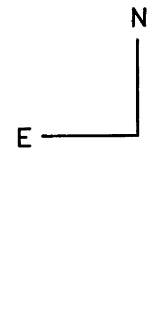

2'

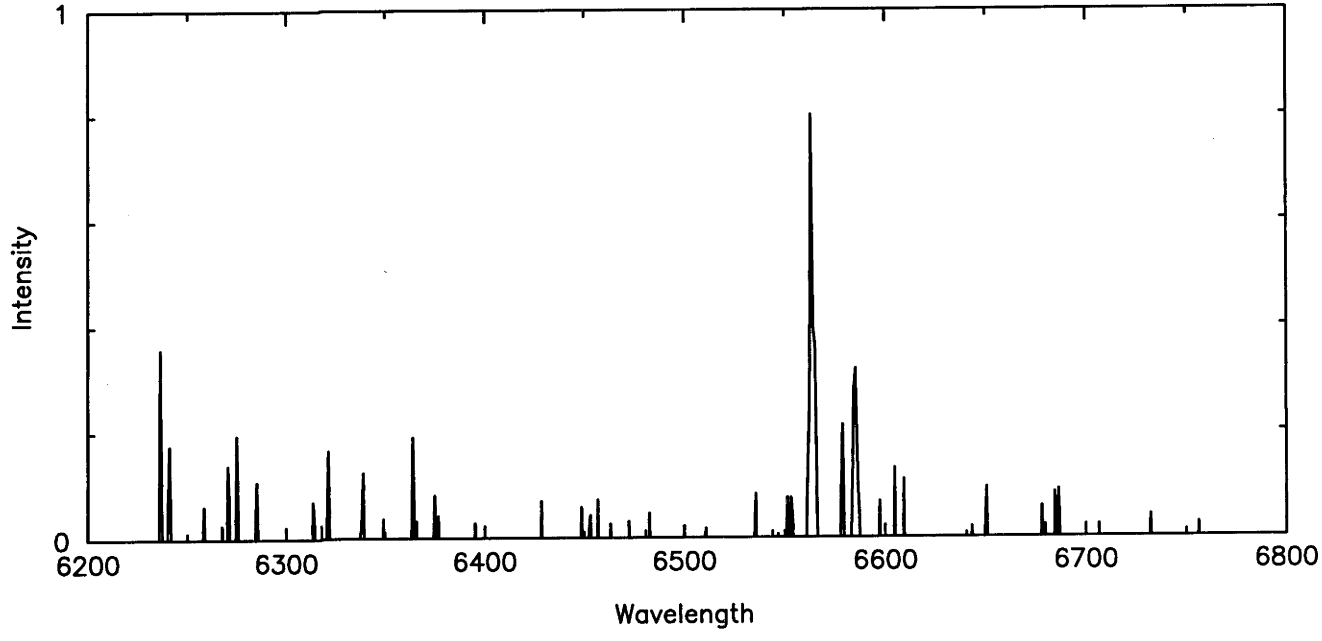

PN G007.7−05.3

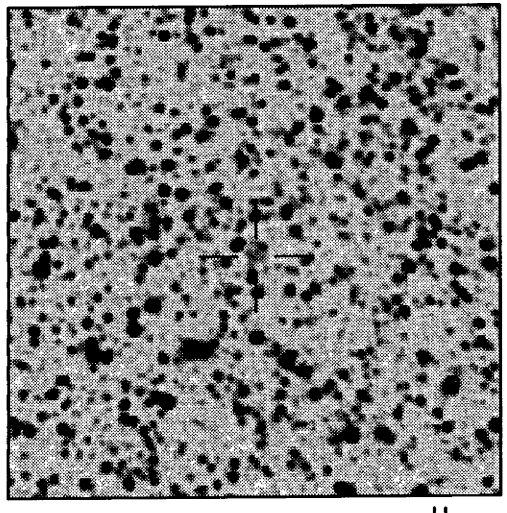

H_α

Cont

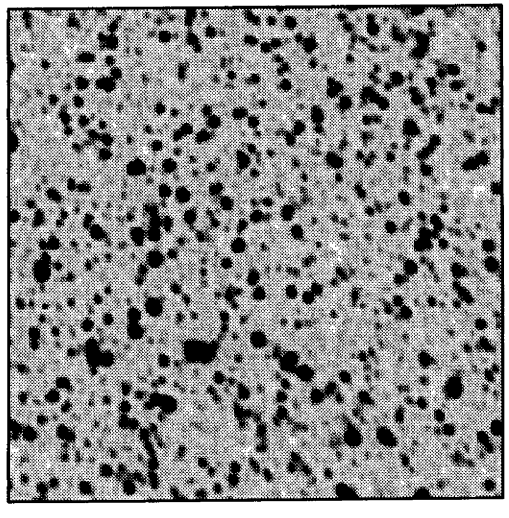

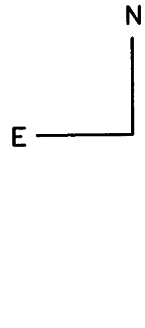

2'

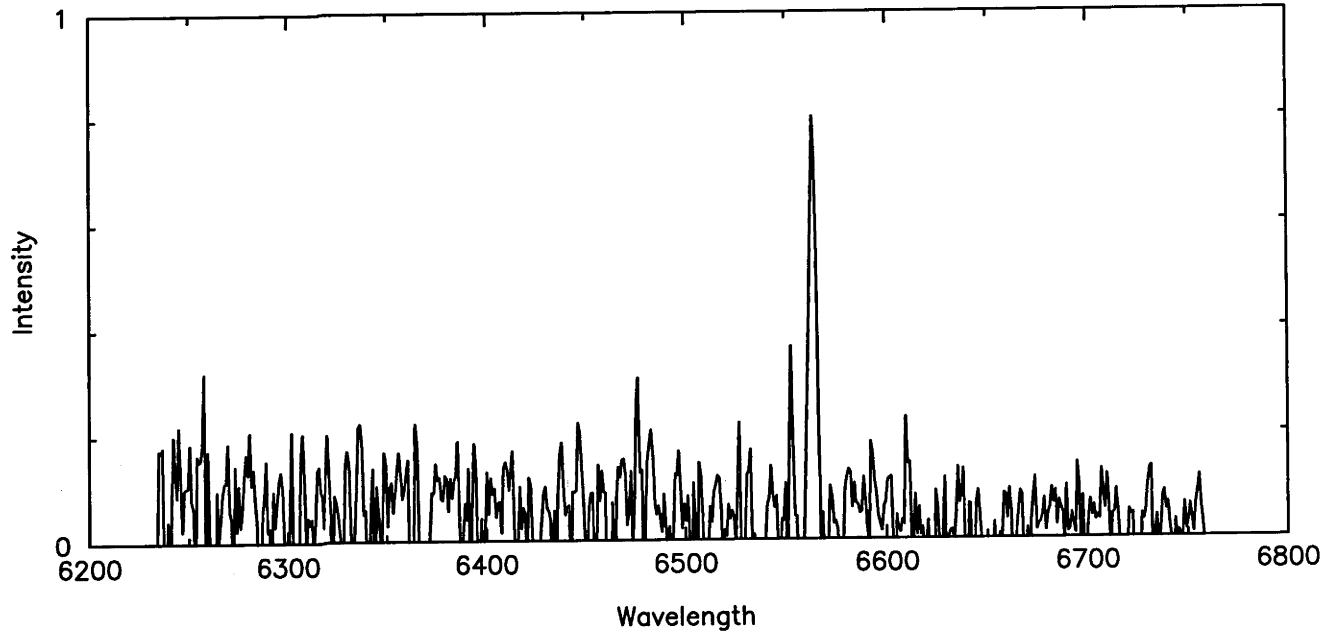

PN G009.3−06.5

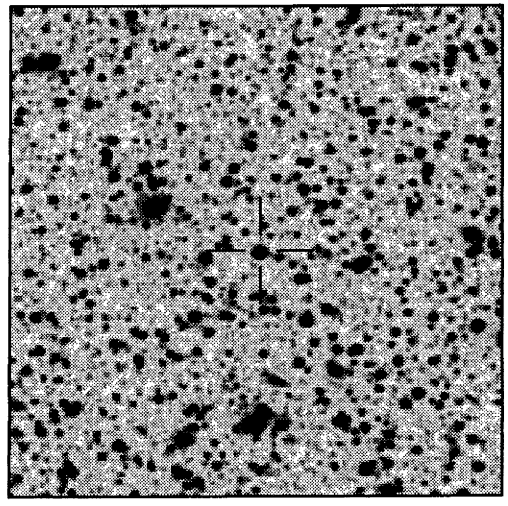

H_α

Cont

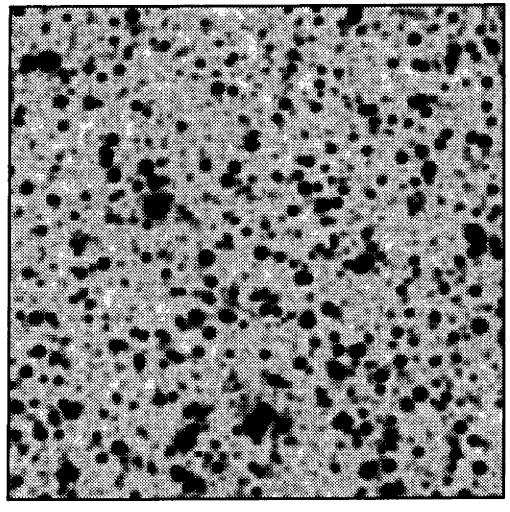

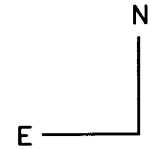

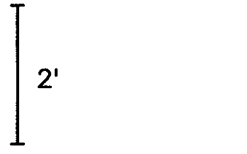

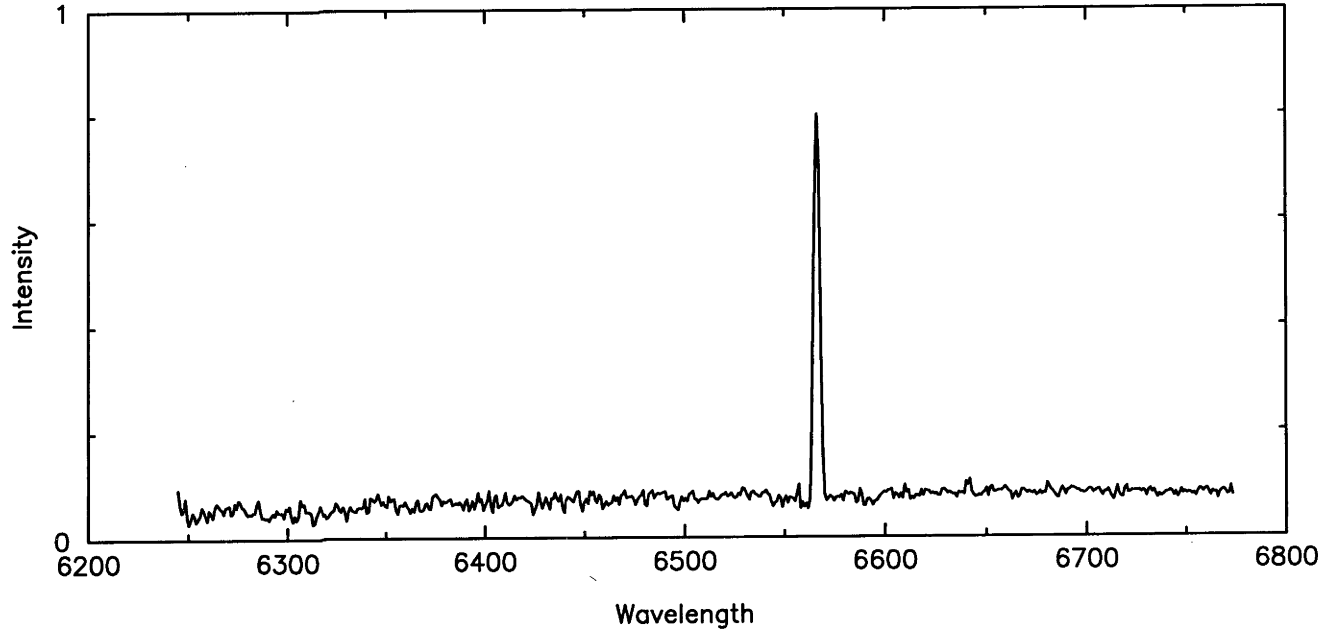

PN G009.4−05.6

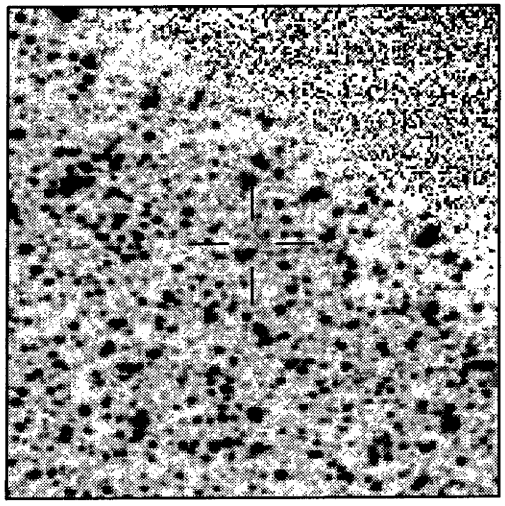

H_α

Cont

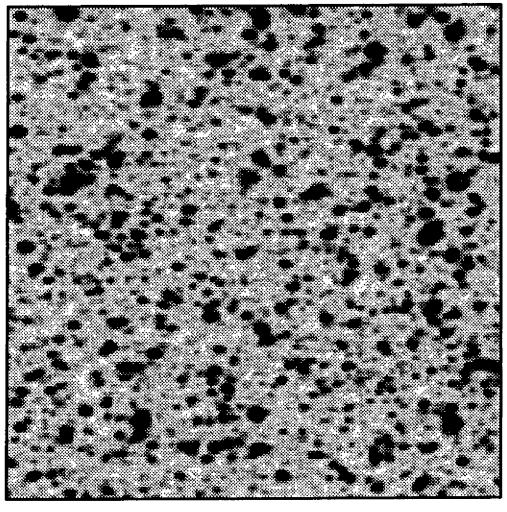

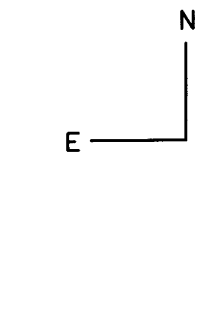

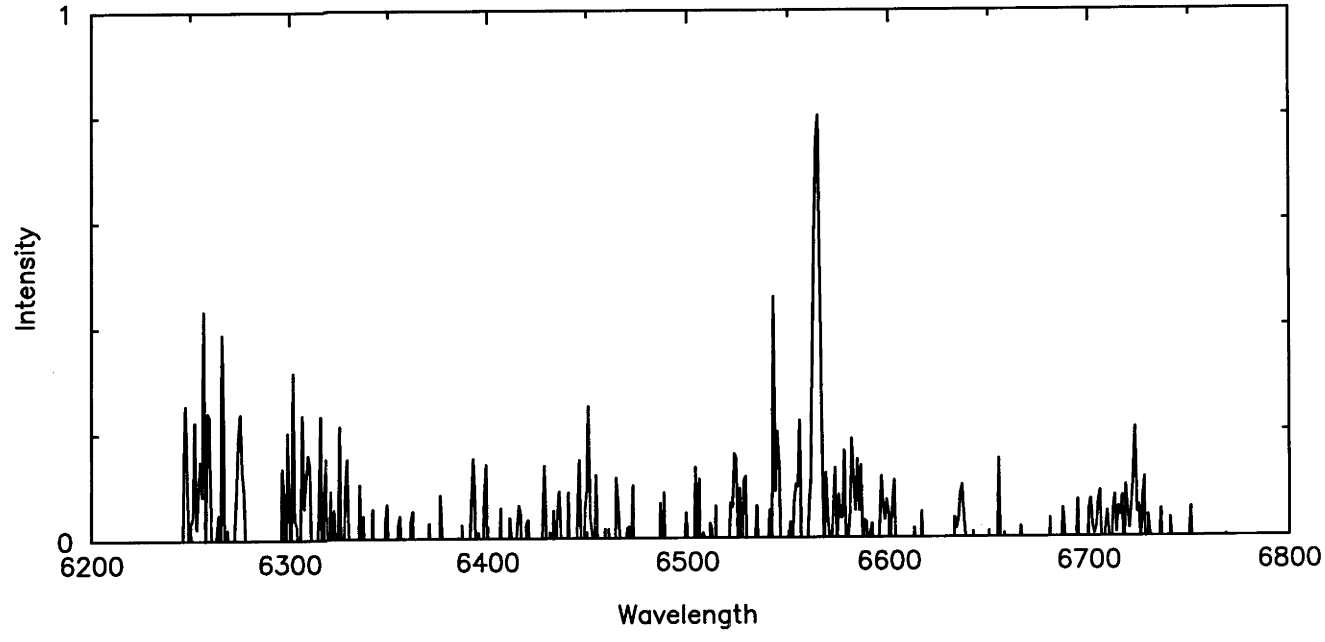

PN G011.1−07.9

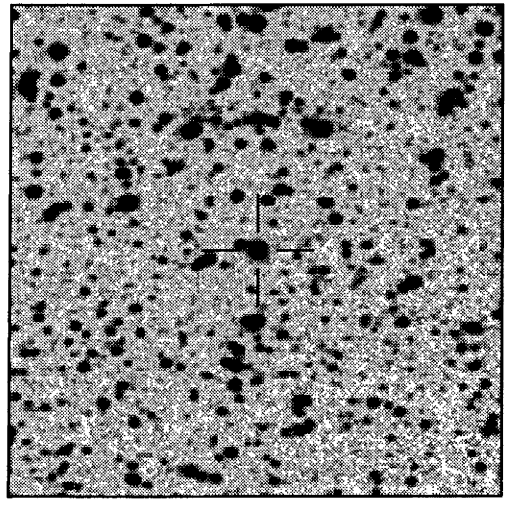

H_α

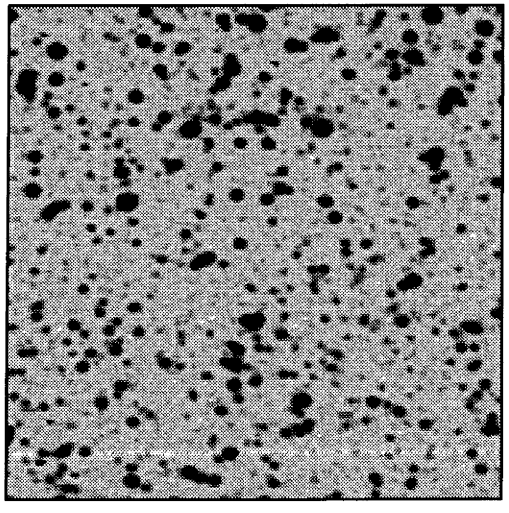

Cont

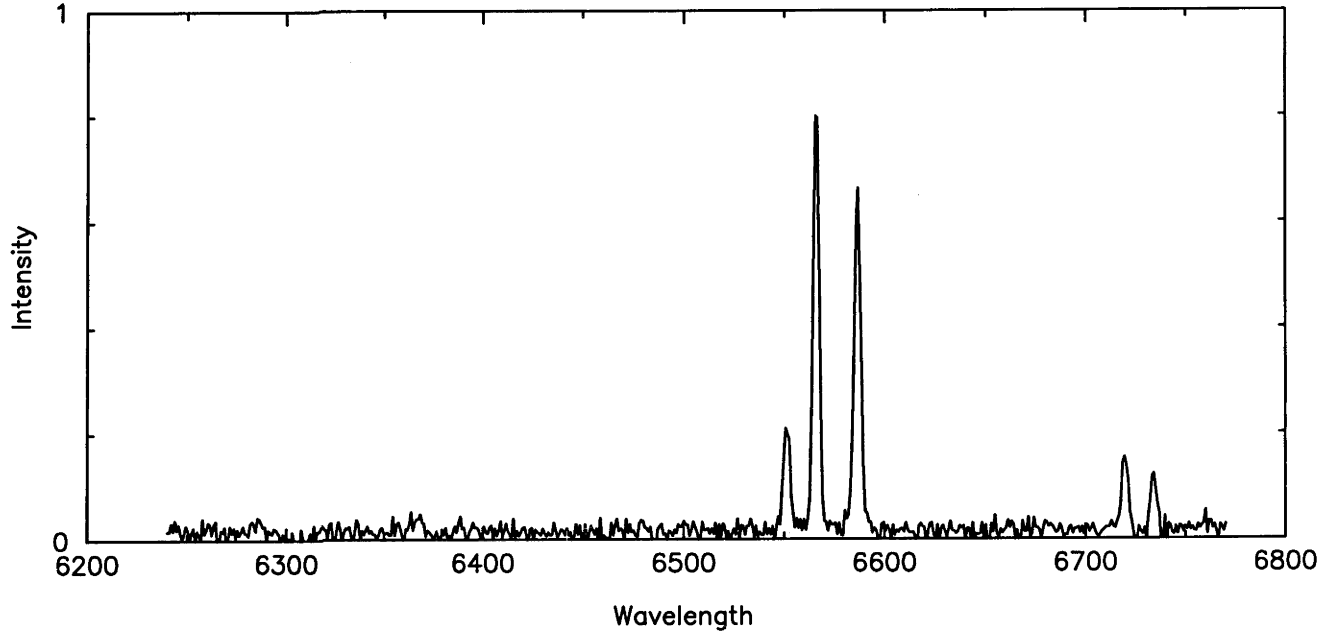

PN G011.4−07.3

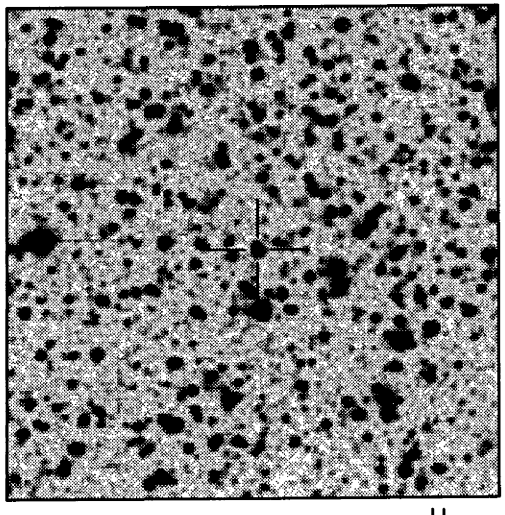

H_α

Cont

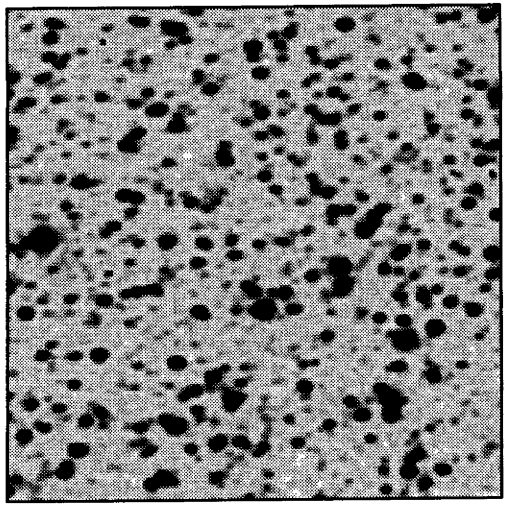

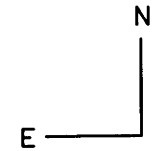

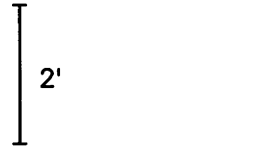

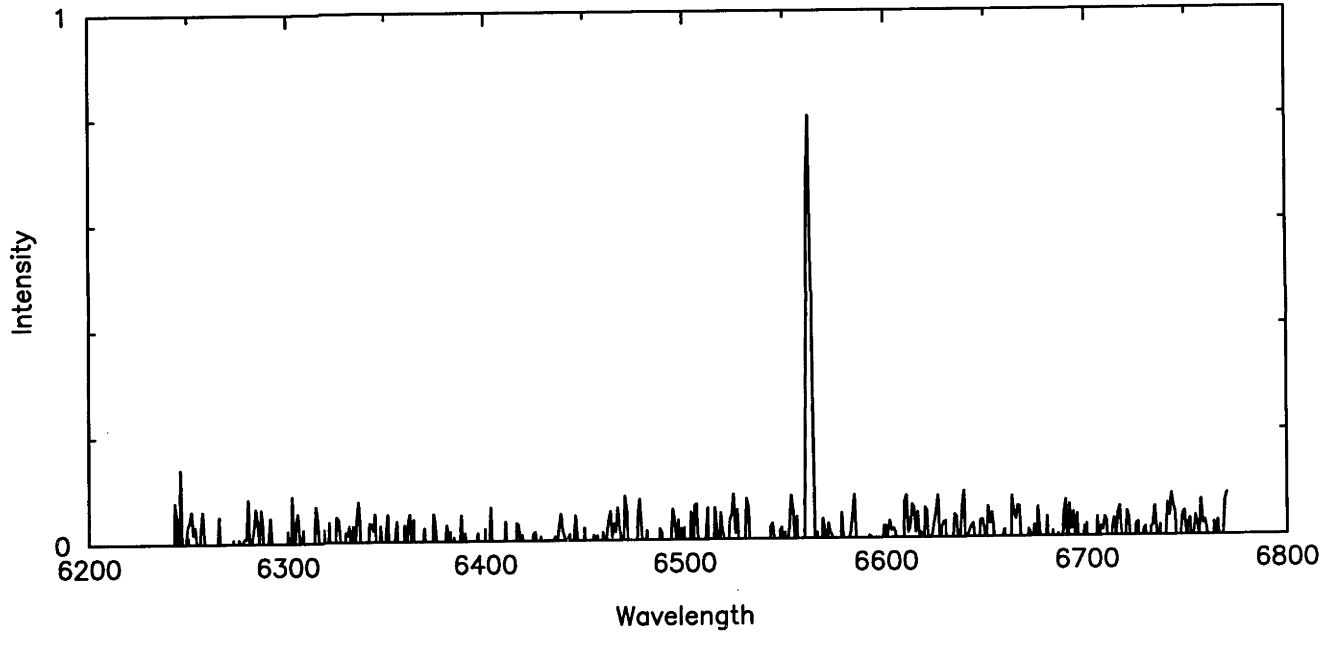

PN G014.4−06.1

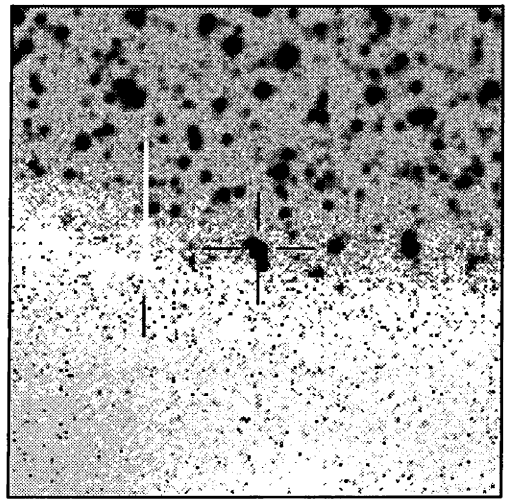

H_α

Cont

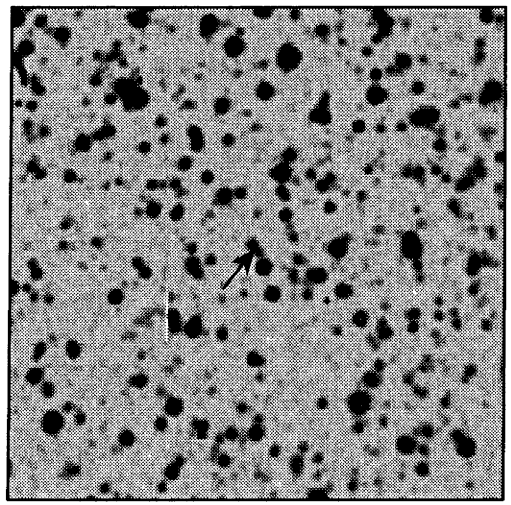

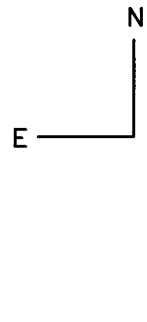

2'

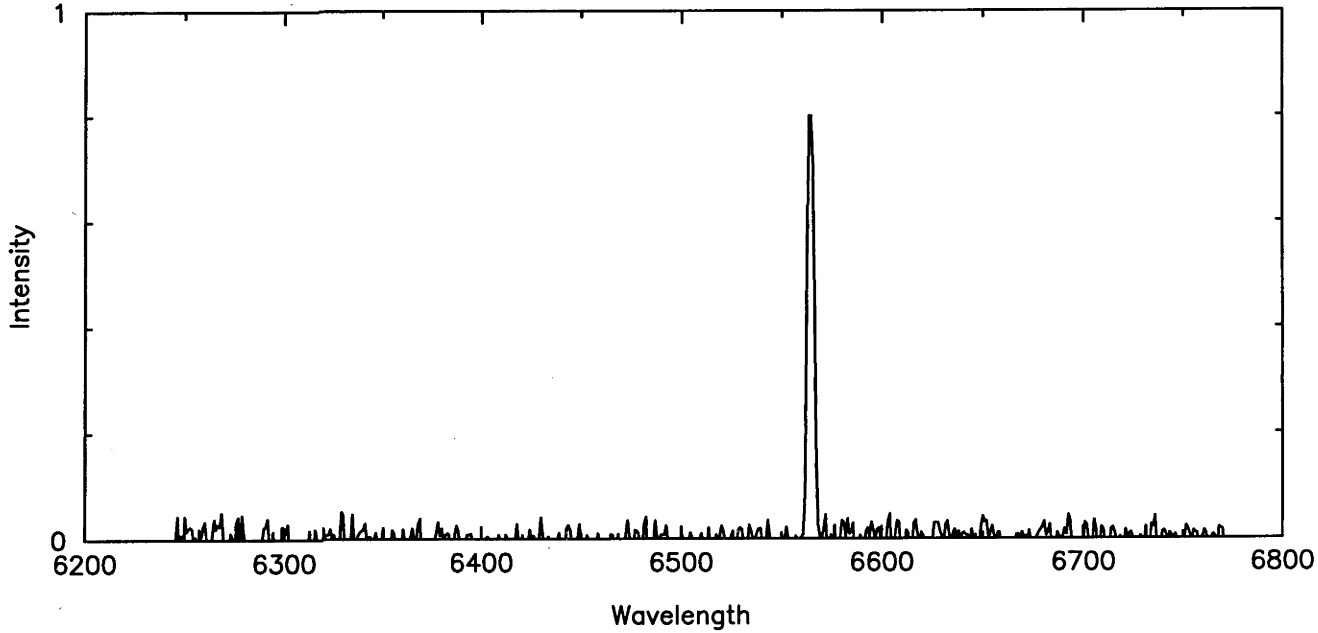

PN G014.8−08.4

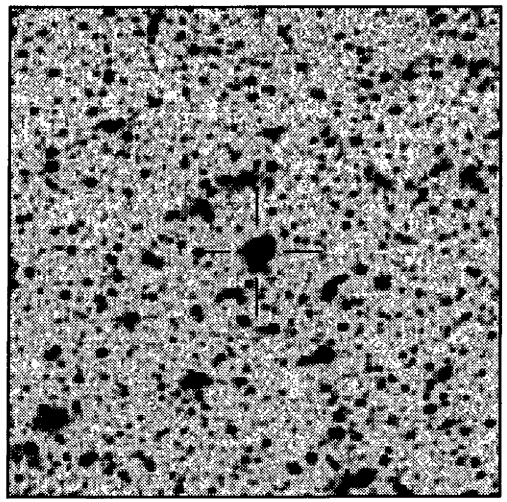

H_α

Cont

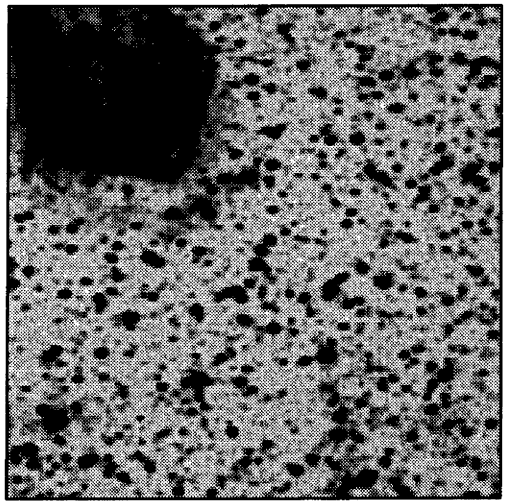

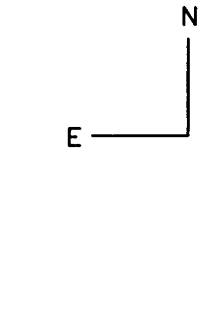

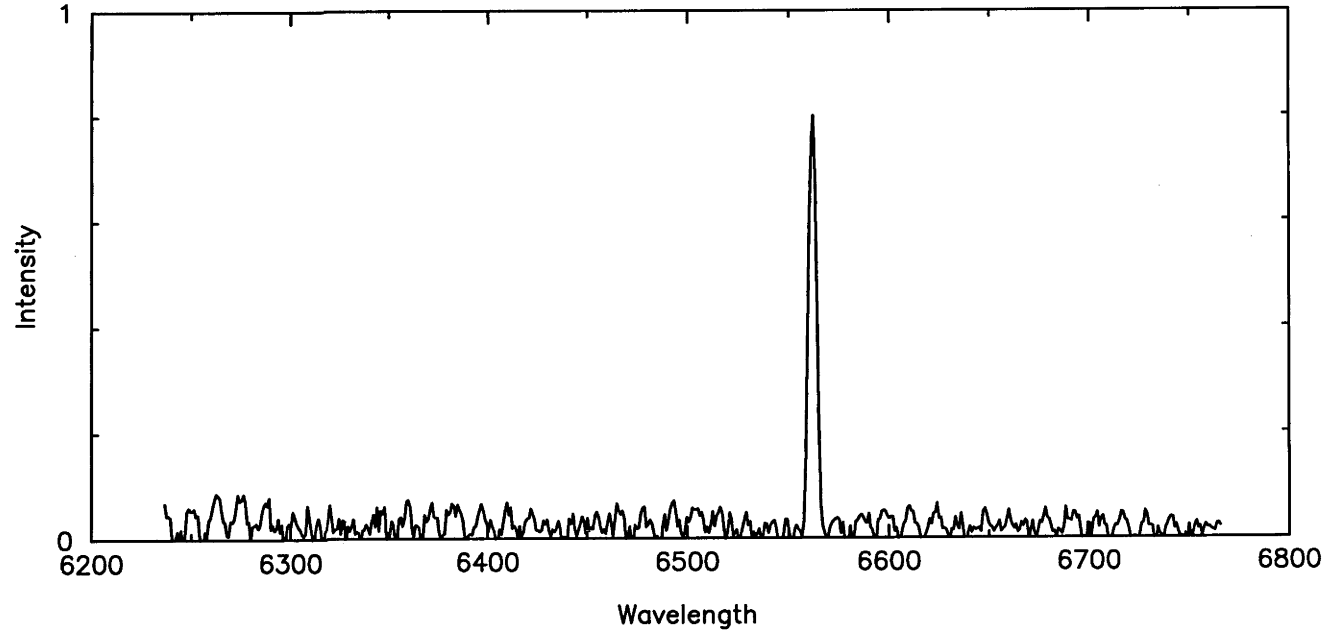

PN G016.0−07.6

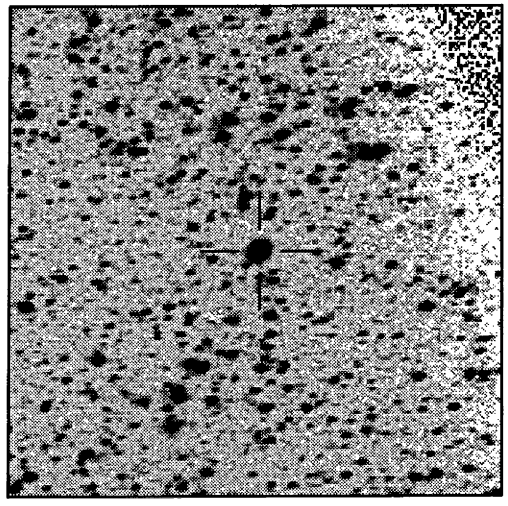

H_α

Cont

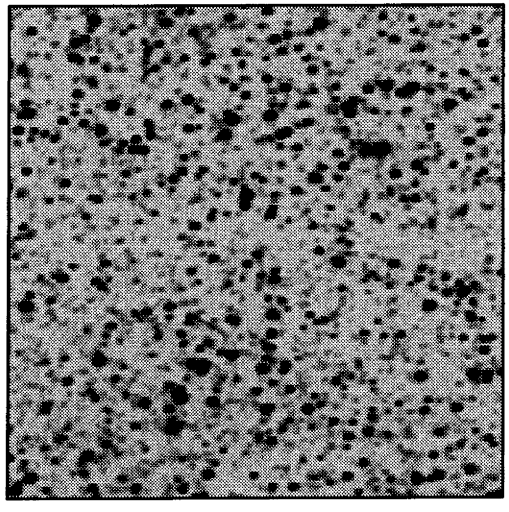

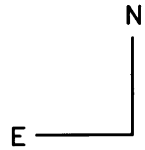

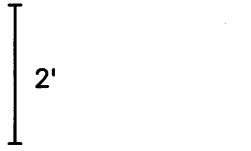

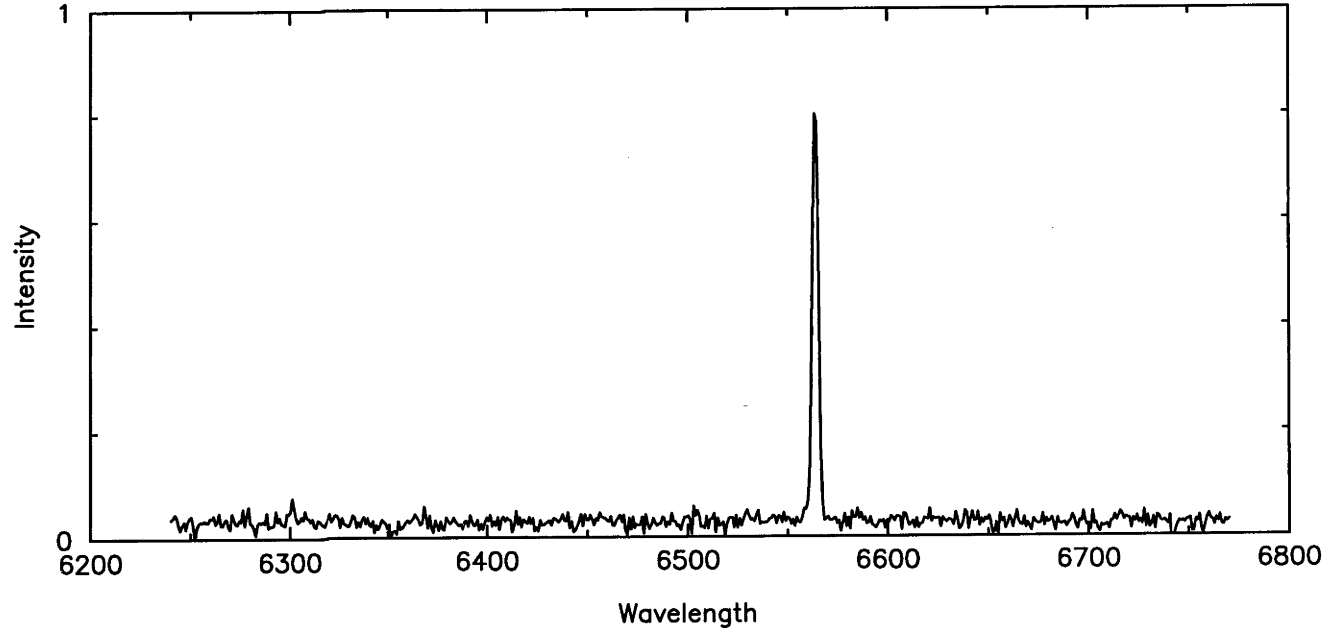

PN G016.7−07.3

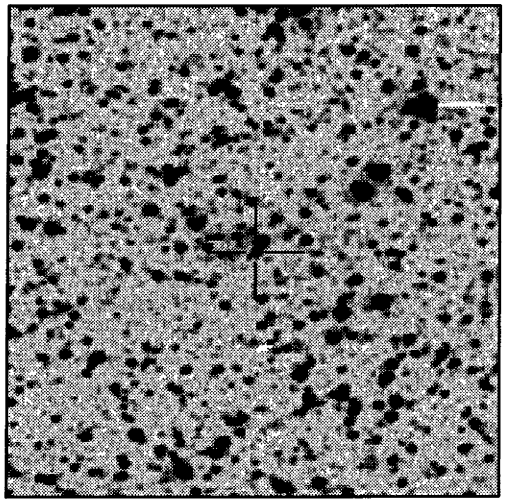

H_α

Cont

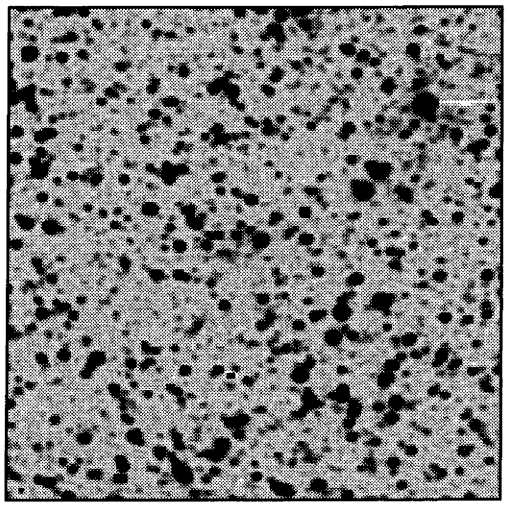

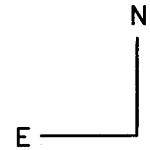

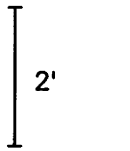

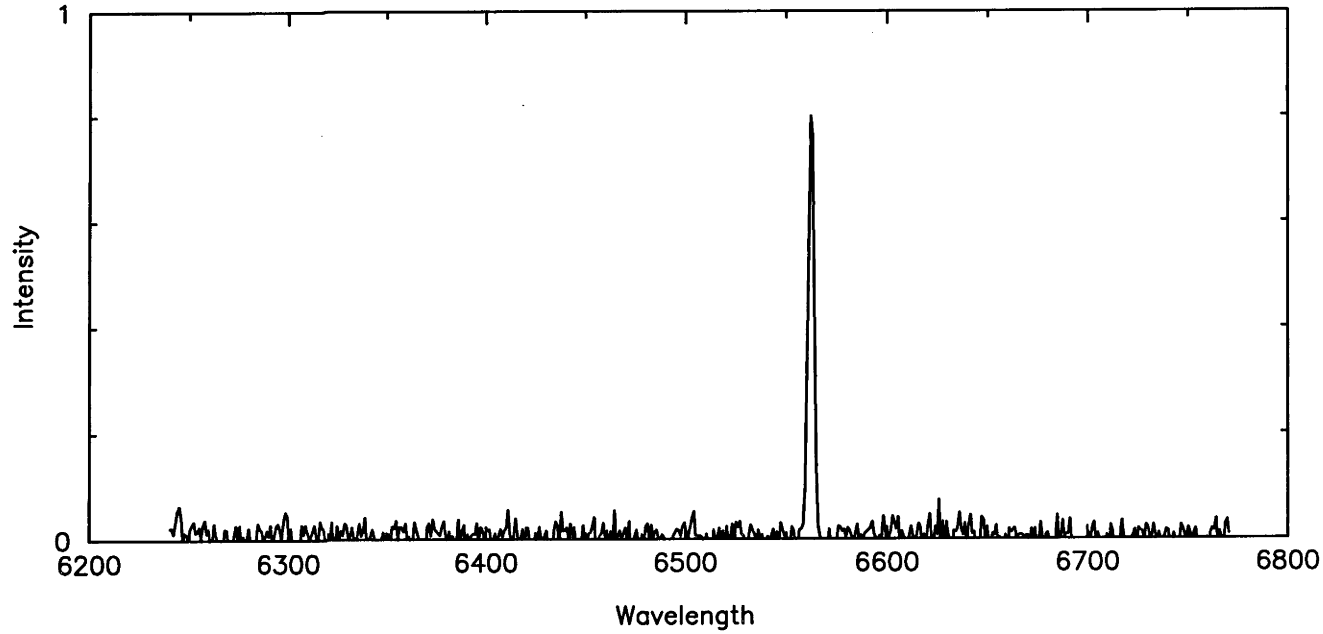

PN G017.5−07.4

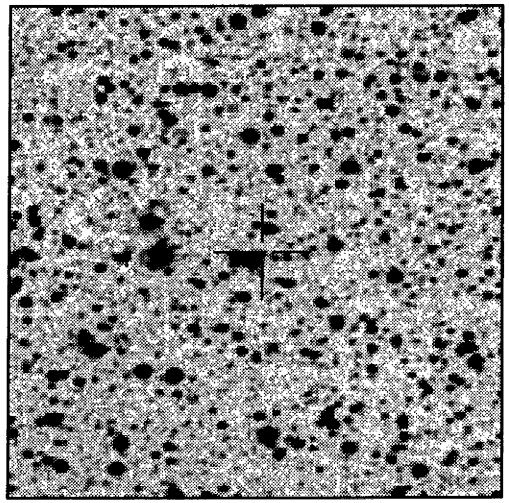

H_α

Cont

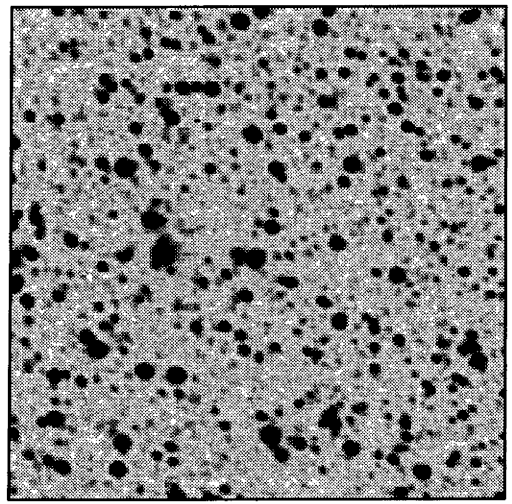

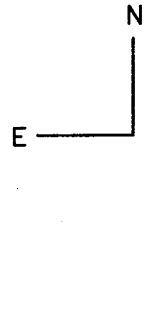

2'

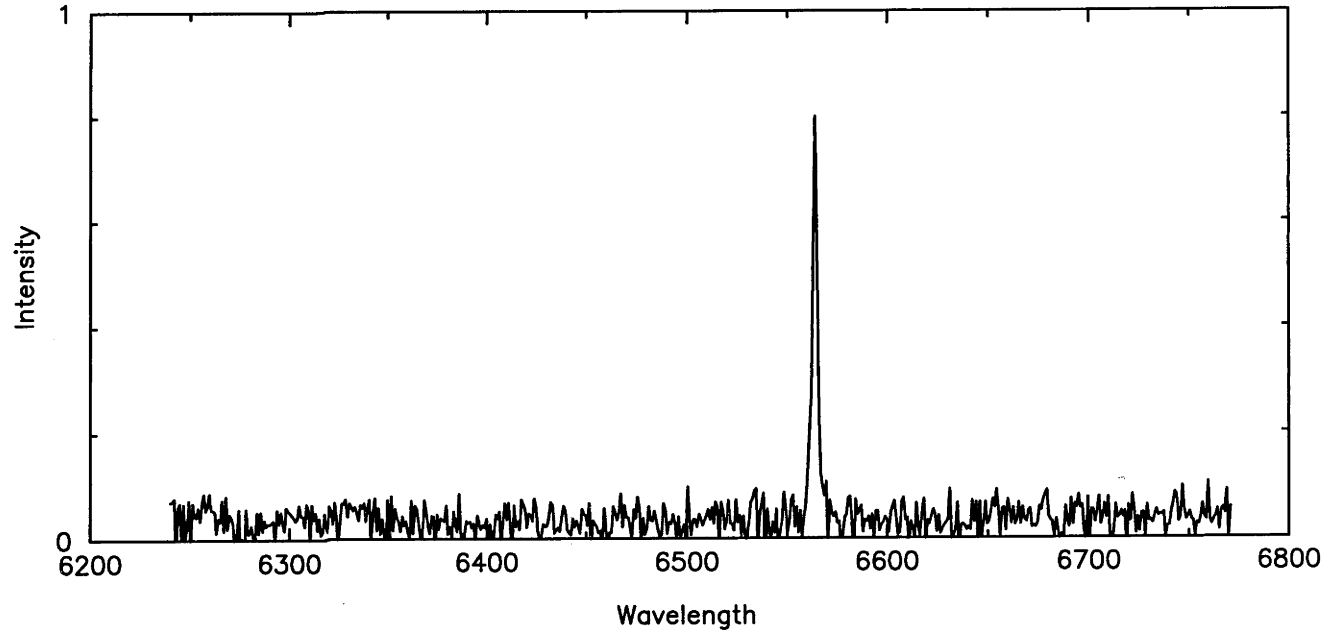

PN G017.5−09.2

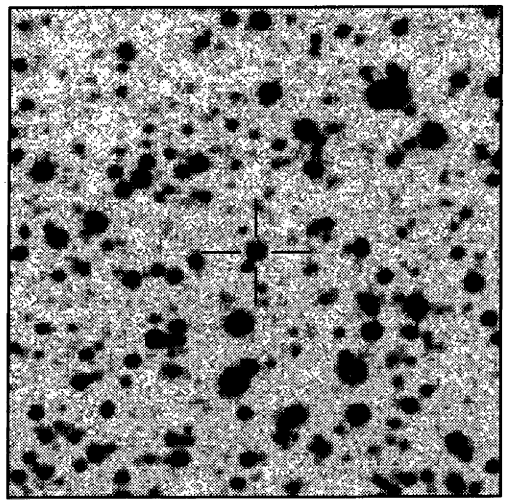

H_α

Cont

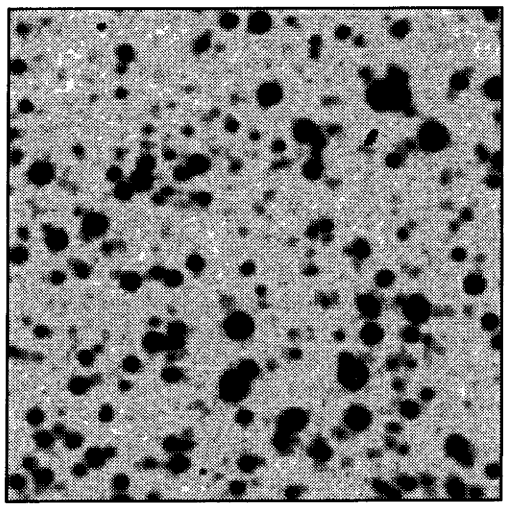

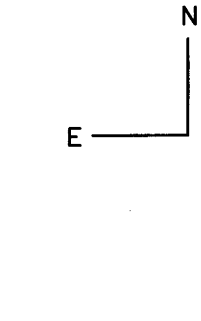

2'

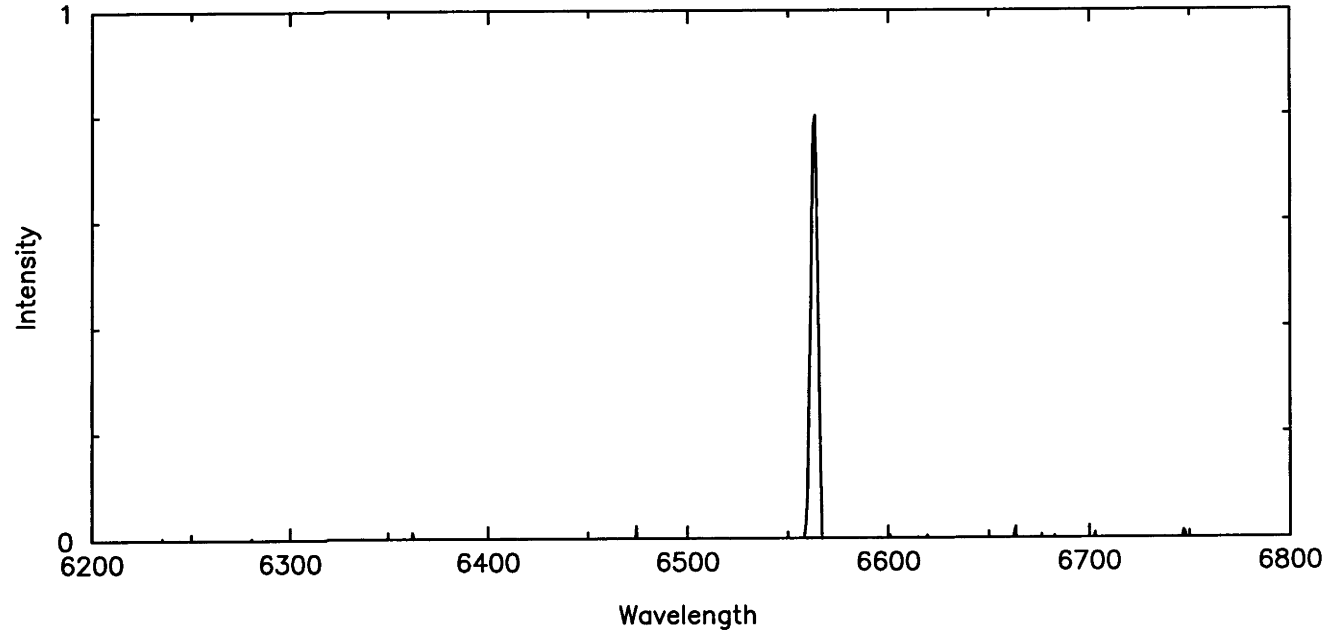

PN G341.0+09.4

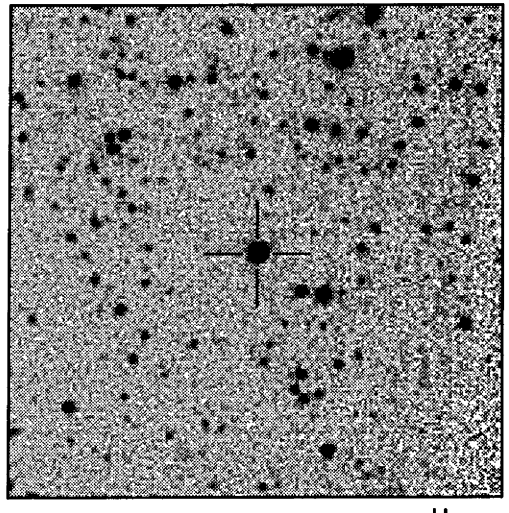

H_α

Cont

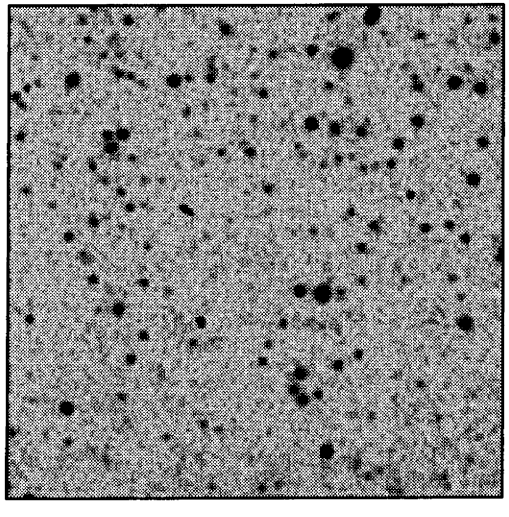

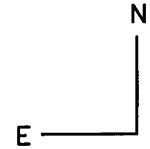

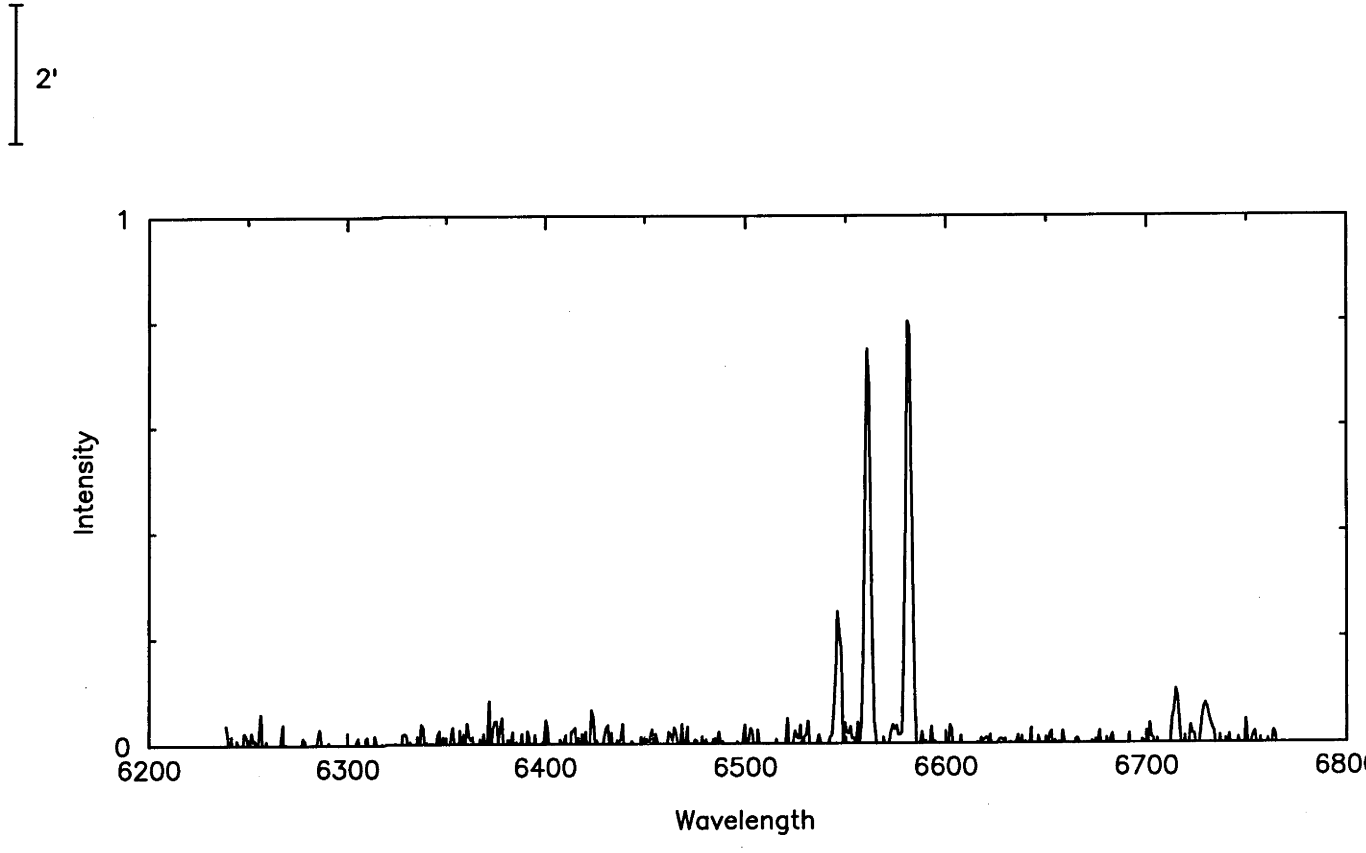

PN G341.7−06.0

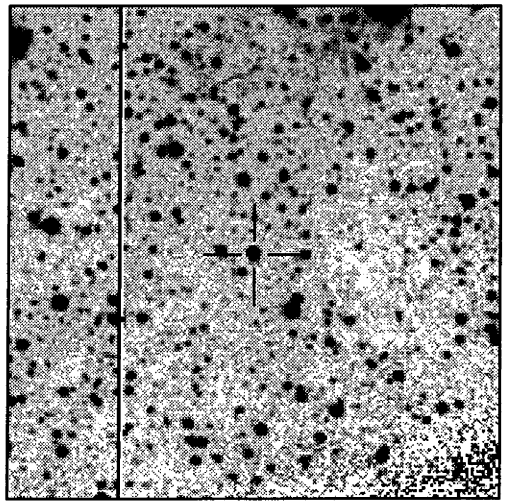

H_α

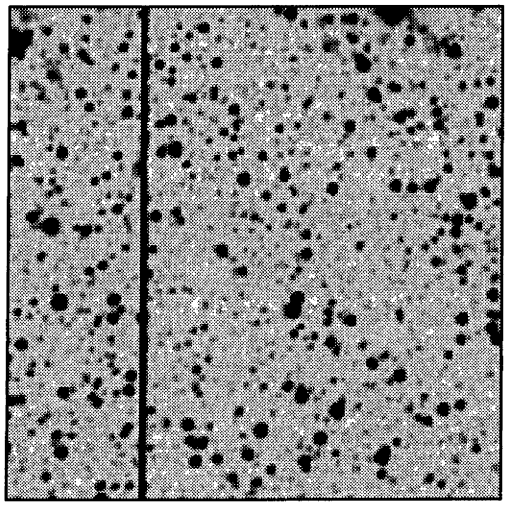

Cont

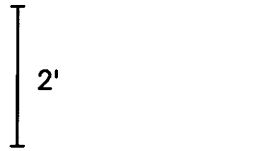

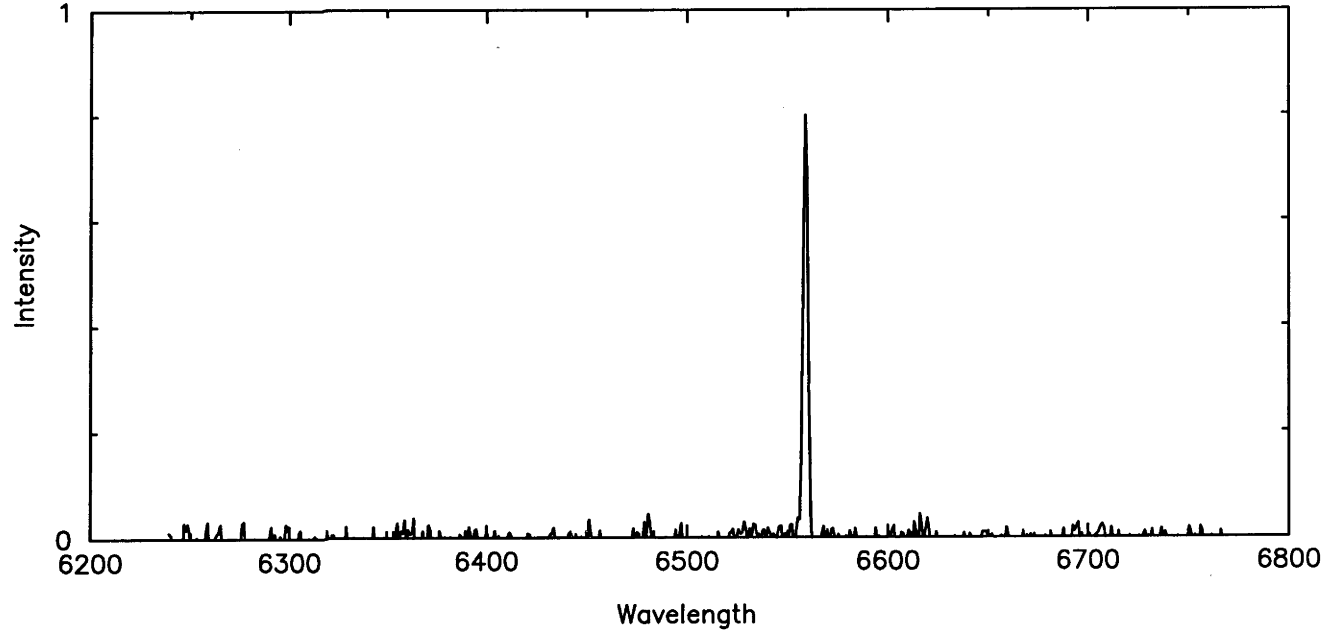

PN G341.9+08.8

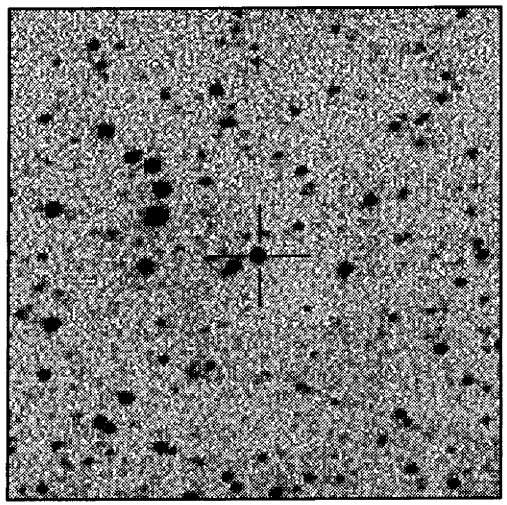

H_α

Cont

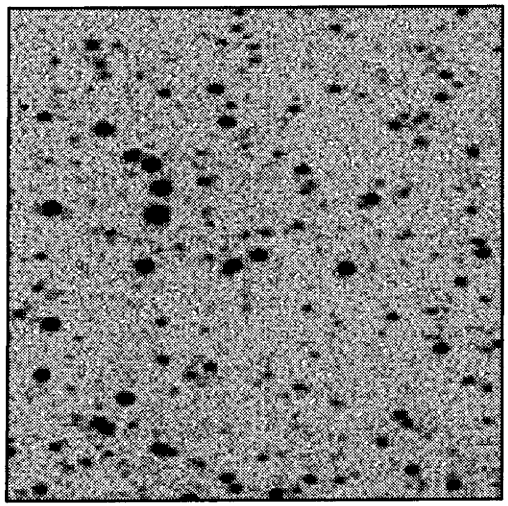

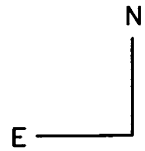

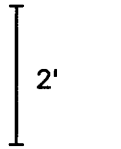

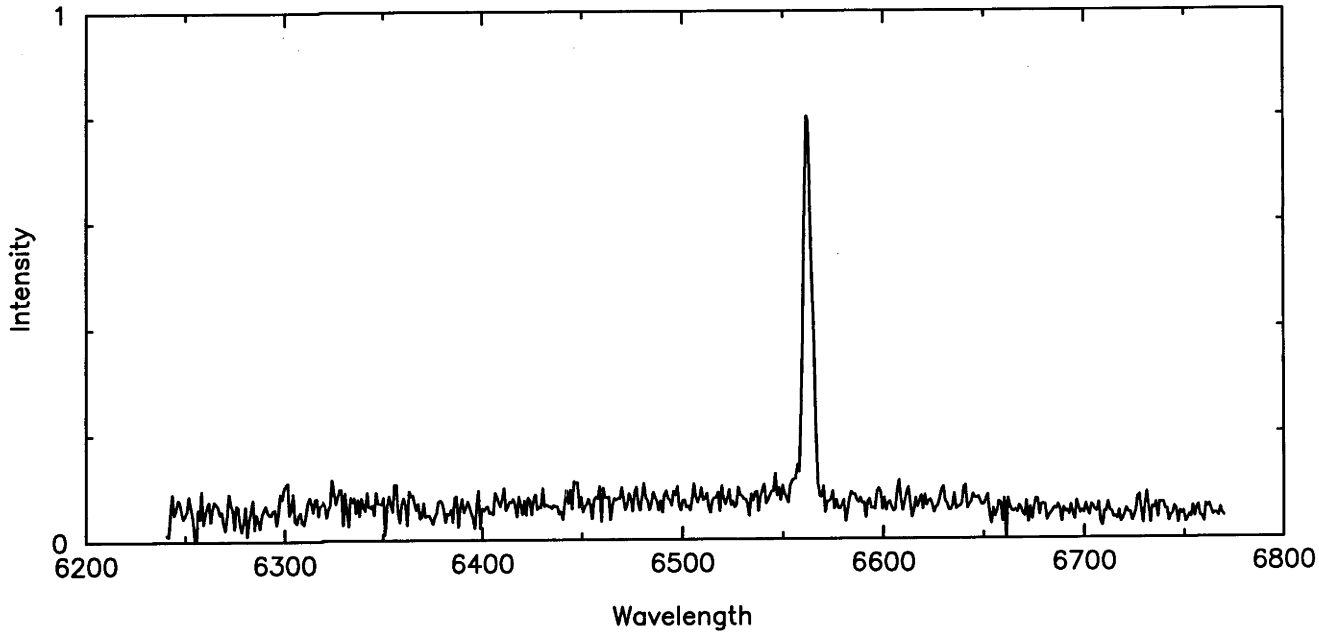

PN G342.3−06.0

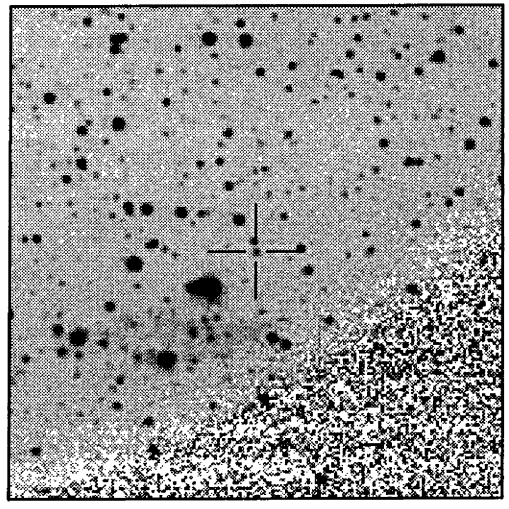

H_α

Cont

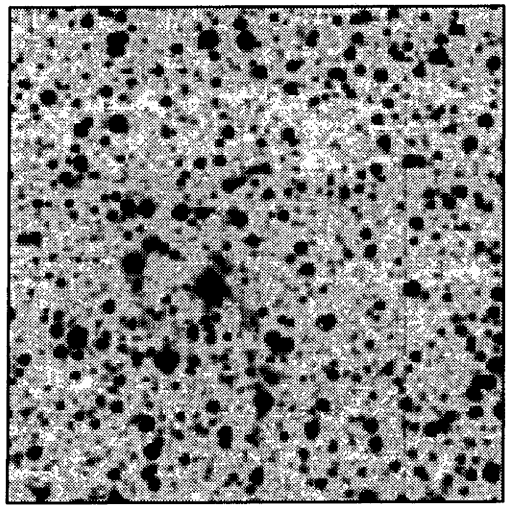

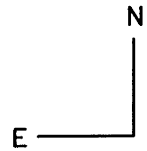

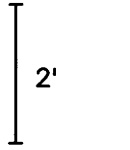

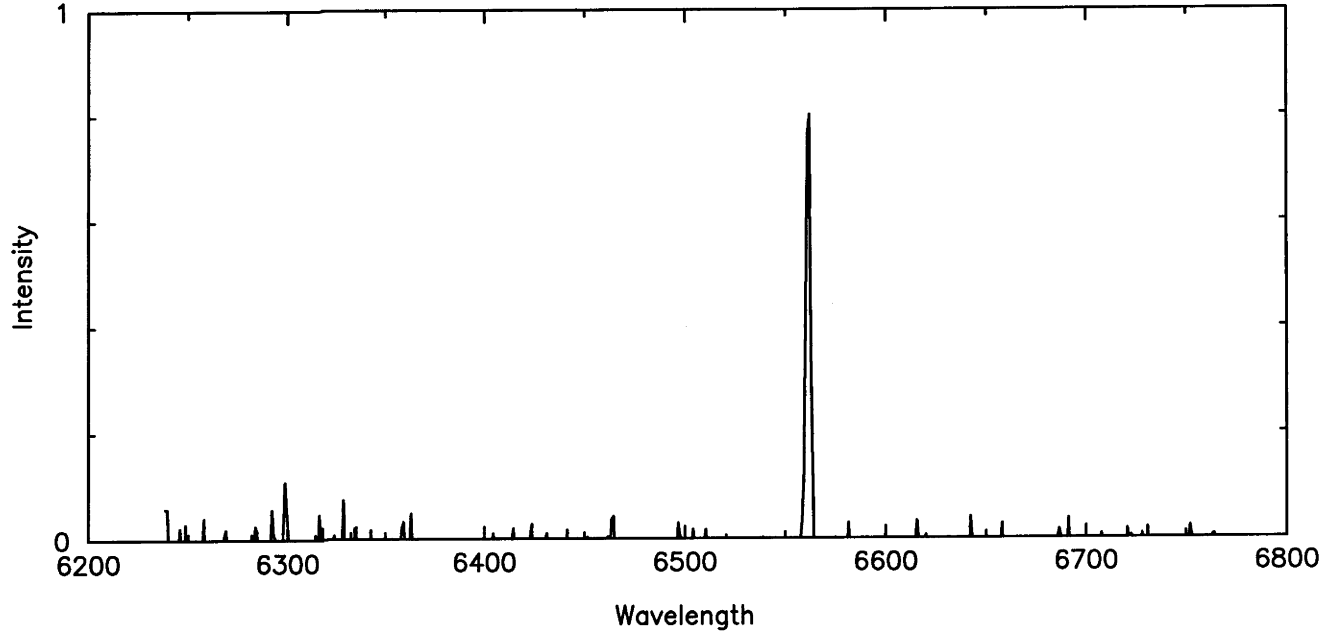

PN G343.7−09.6

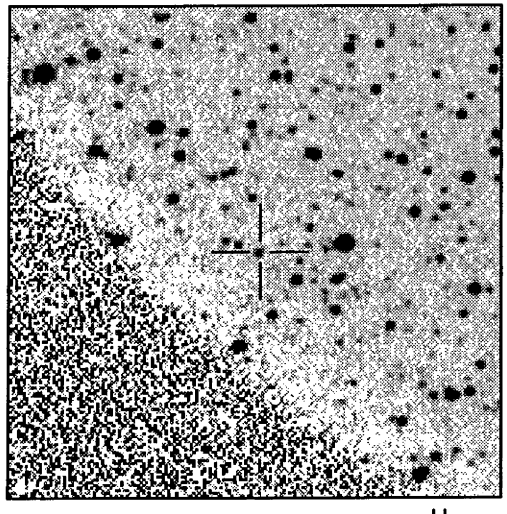

H_α

Cont

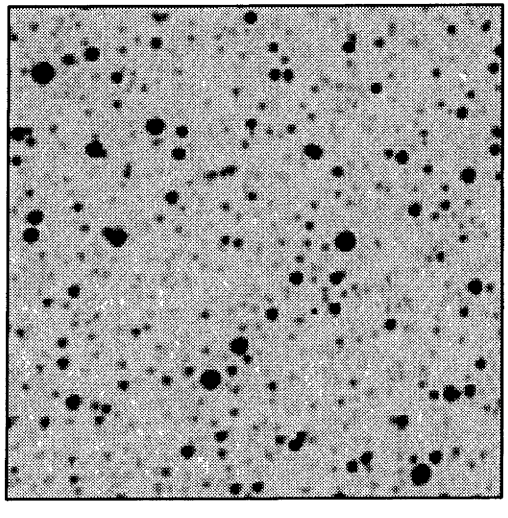

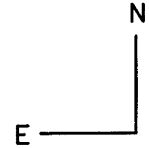

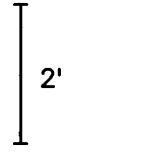

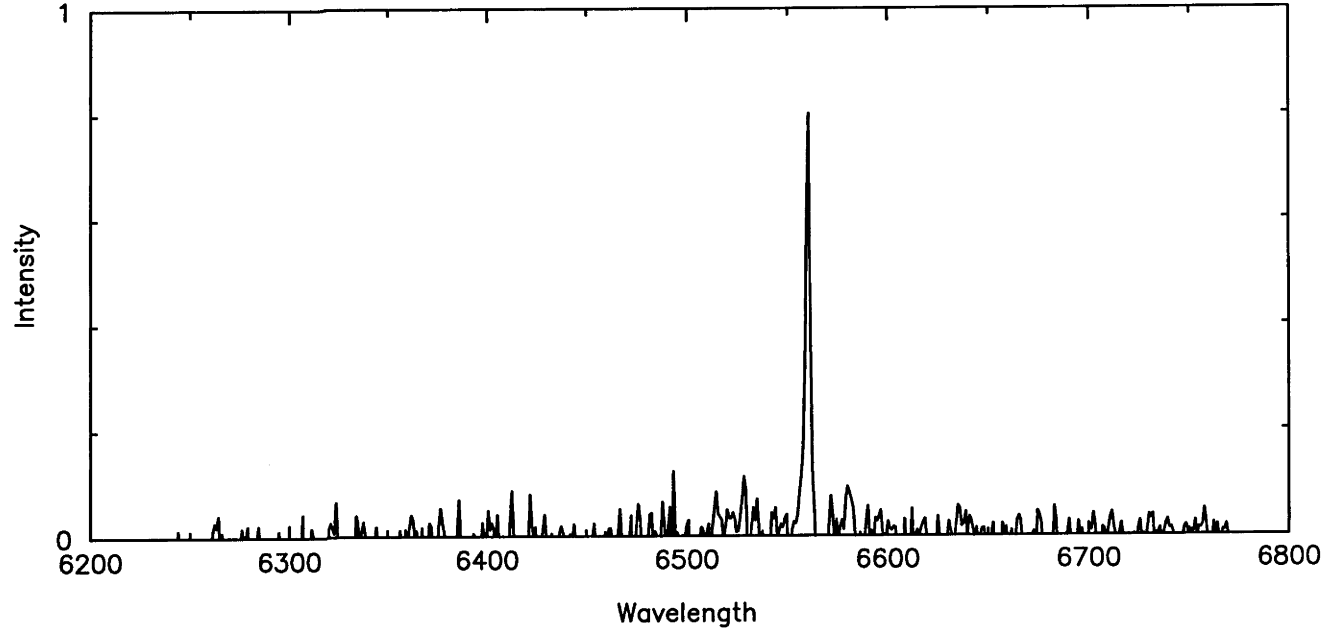

PN G343.9−05.8

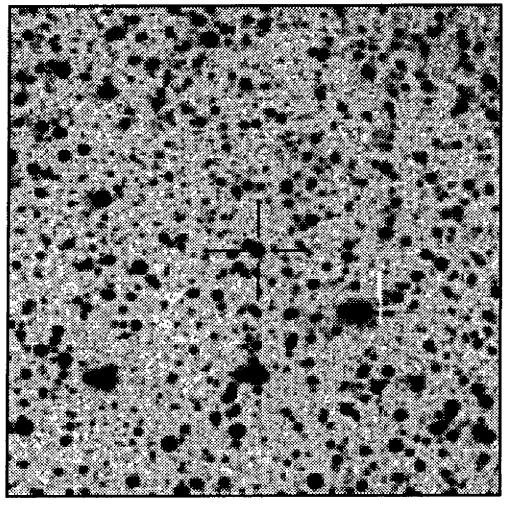

H_α

Cont

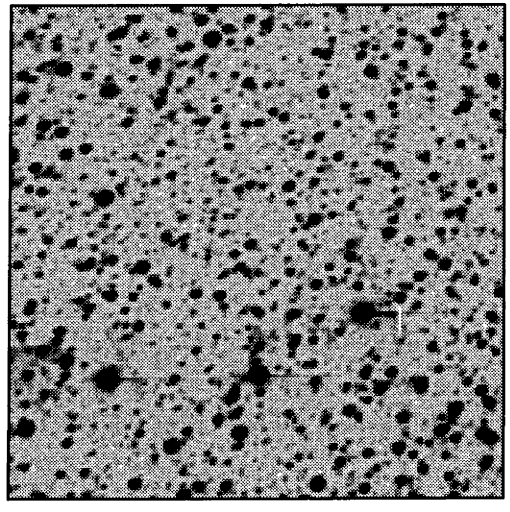

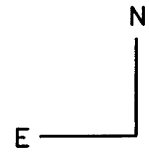

2'

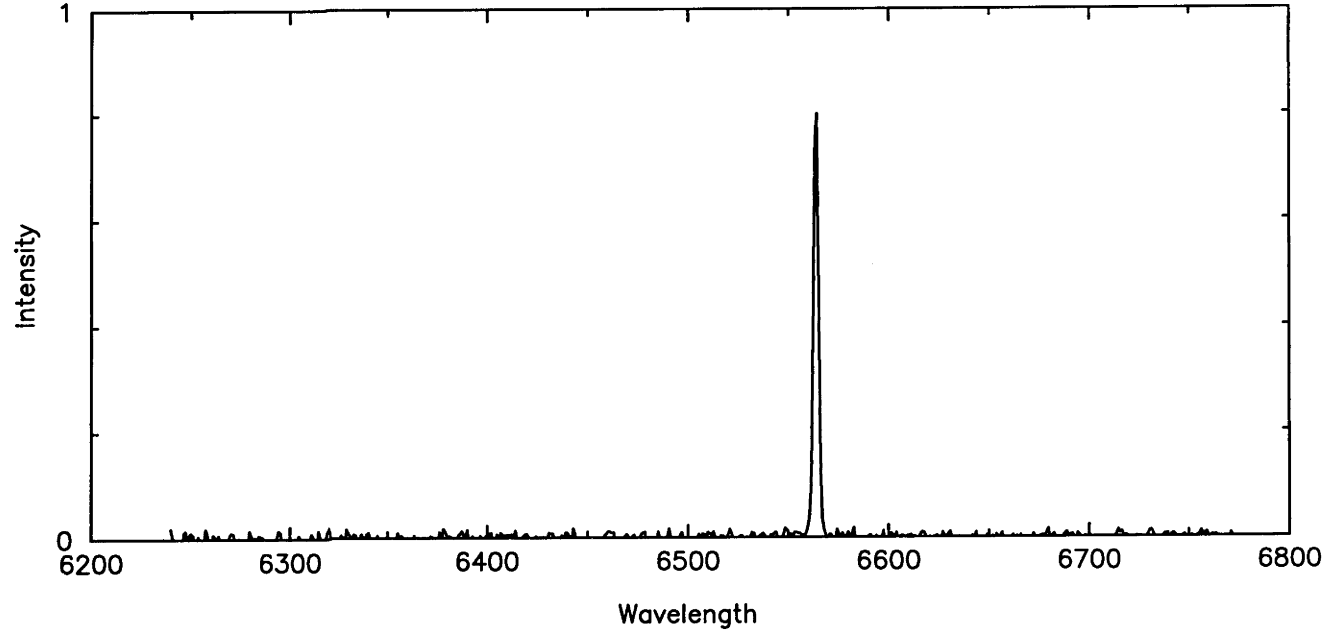

PN G347.9−06.0

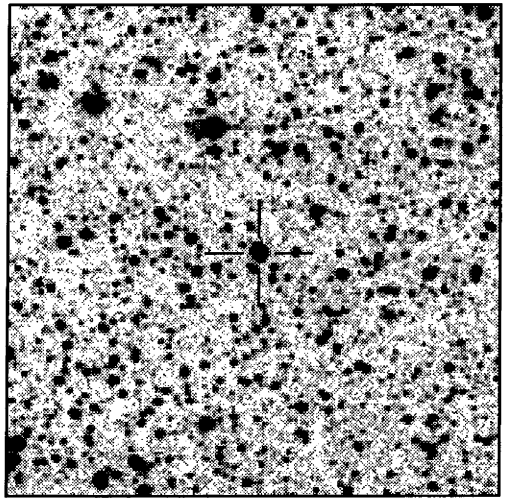

H_α

Cont

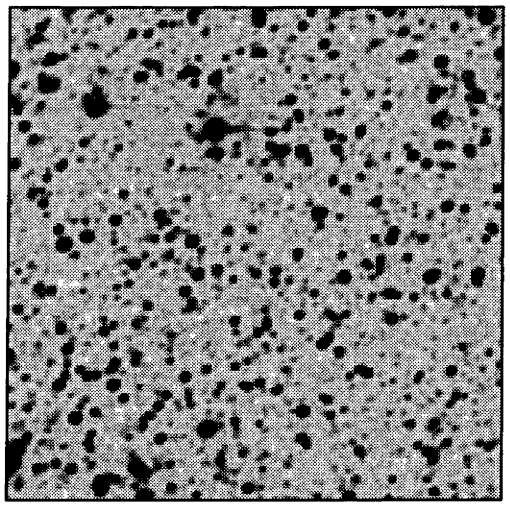

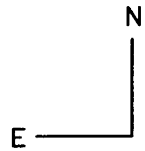

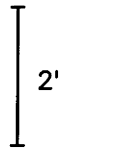

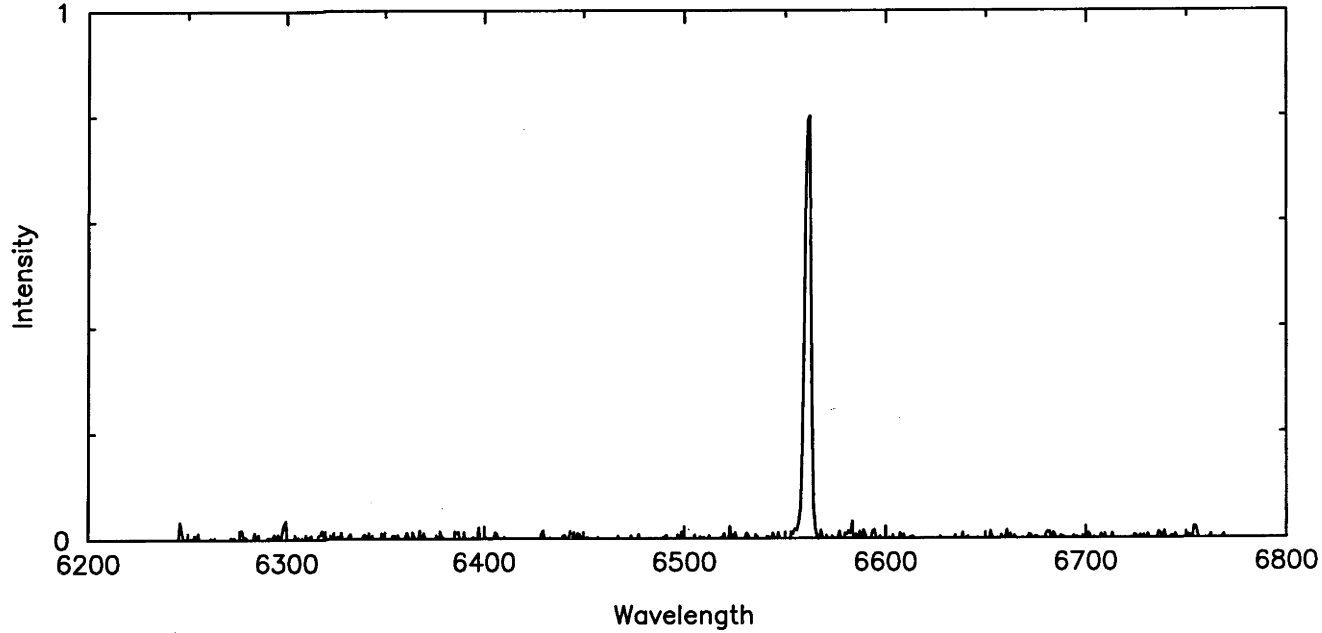

PN G349.7−09.1

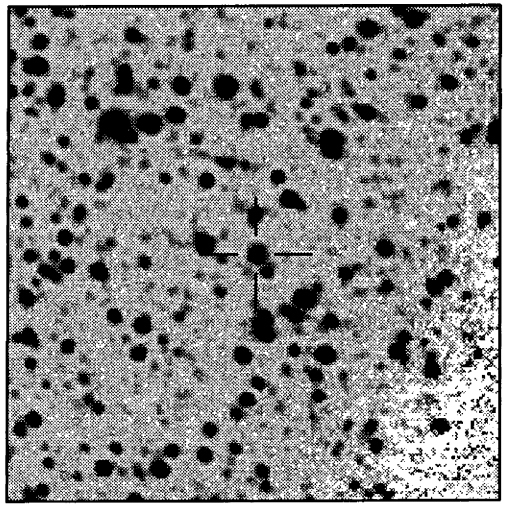

H_α

Cont

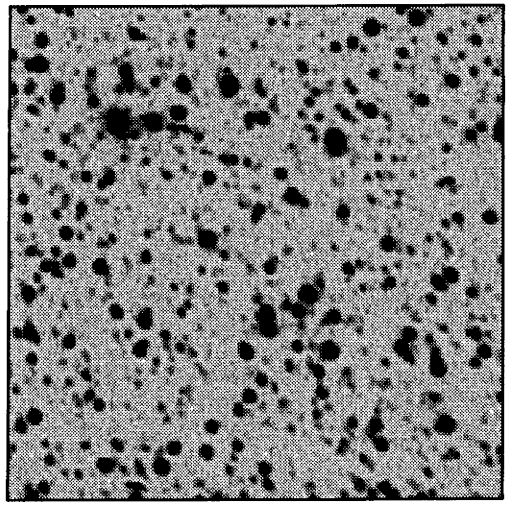

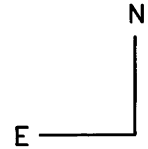

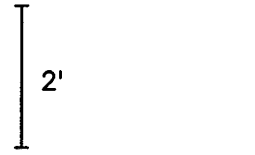

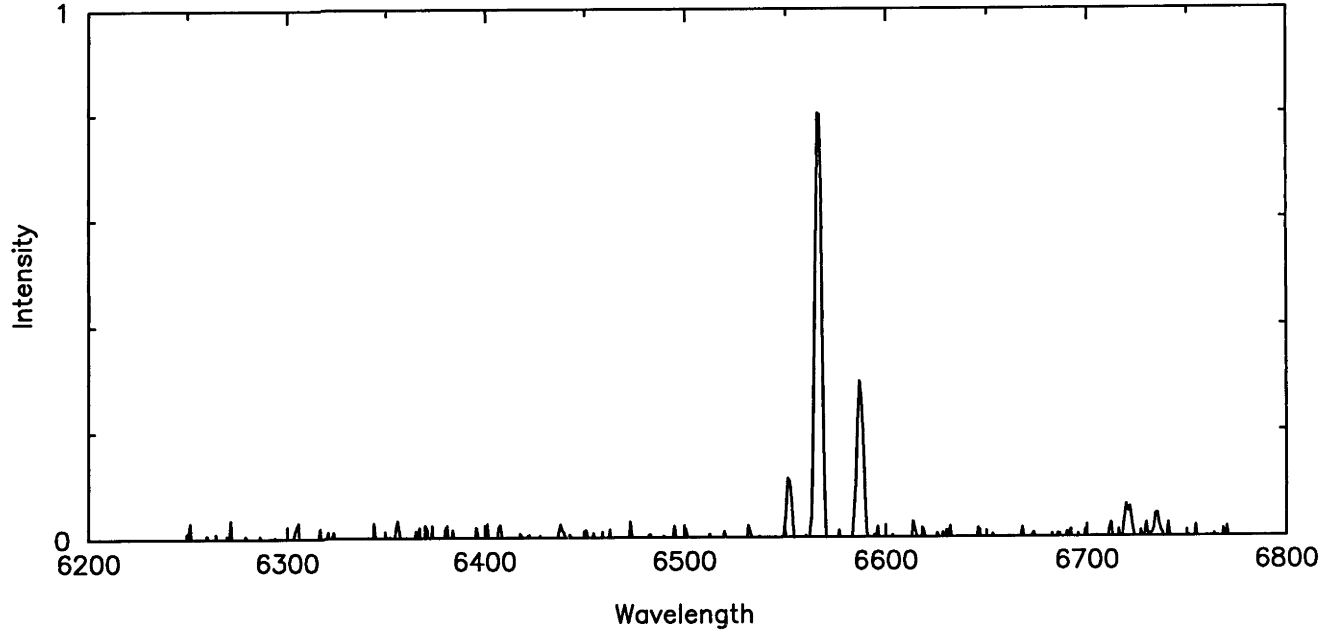

PN G351.2−06.3

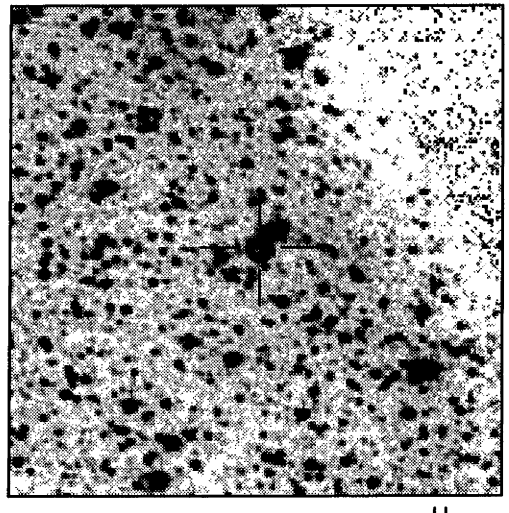

H_α

Cont

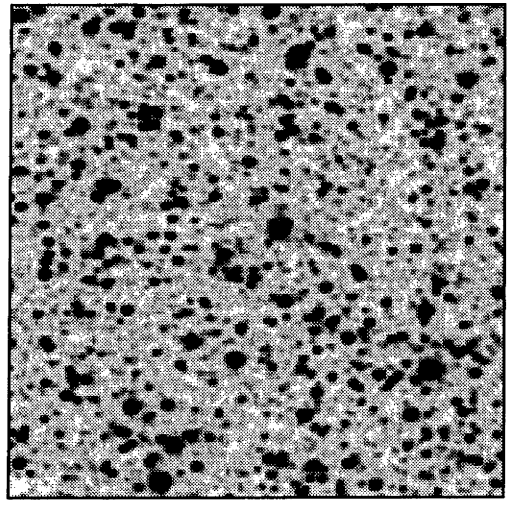

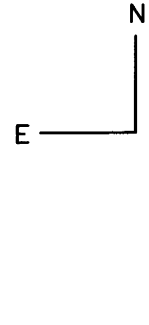

2'

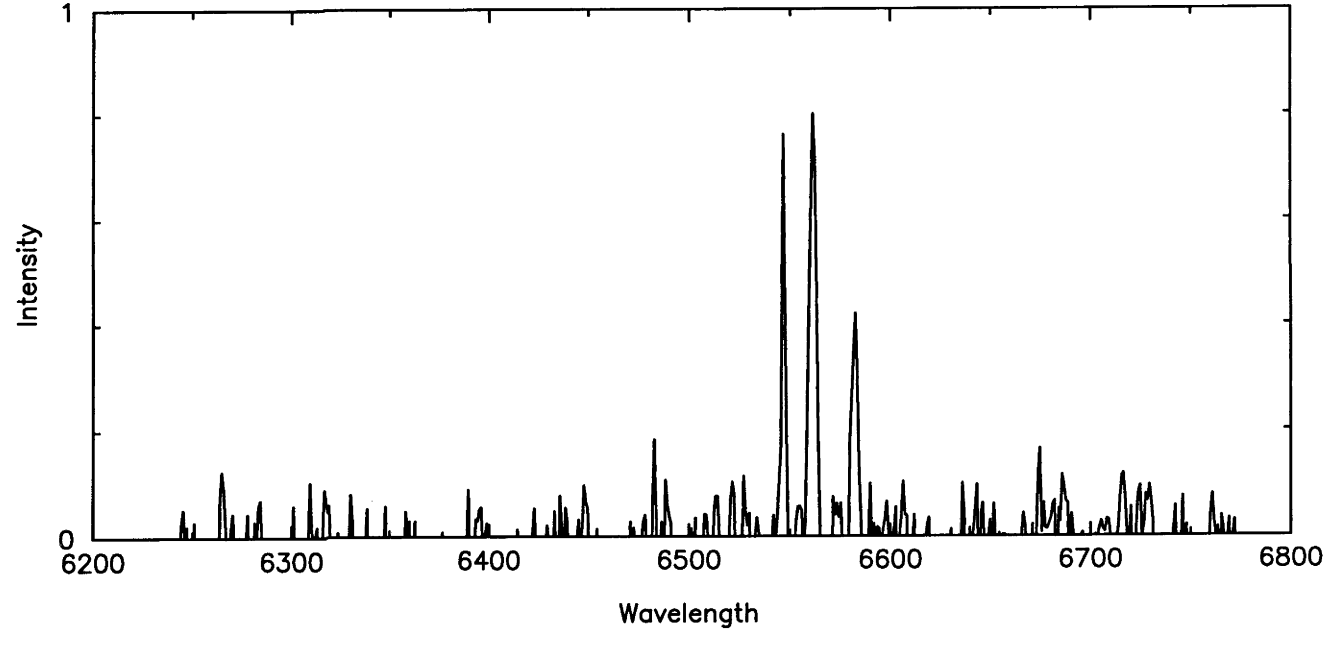

PN G351.5−06.5

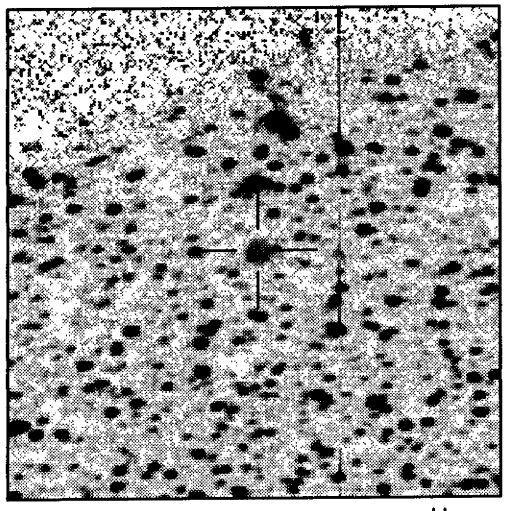

H_α

Cont

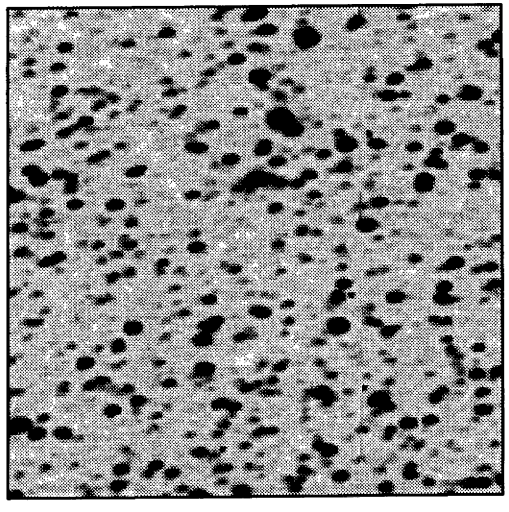

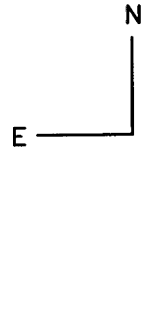

2'

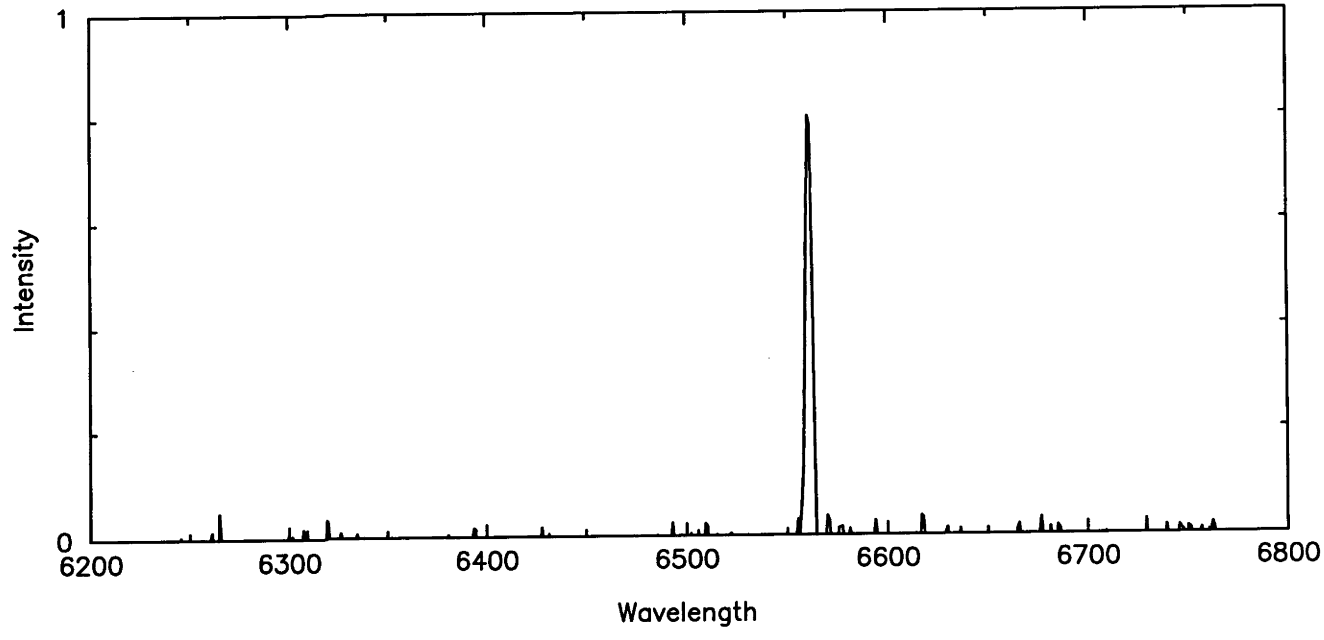

PN G351.7−06.6

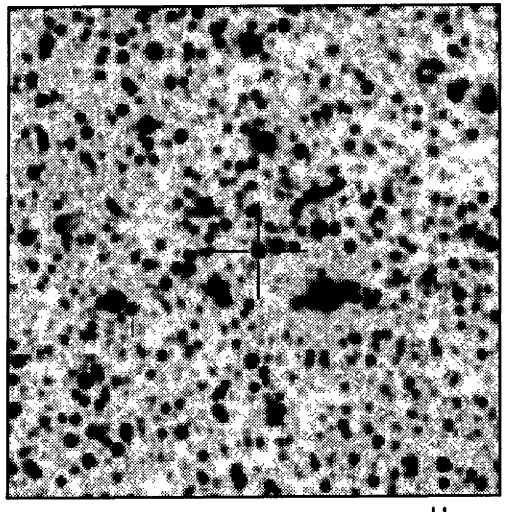

H_α

Cont

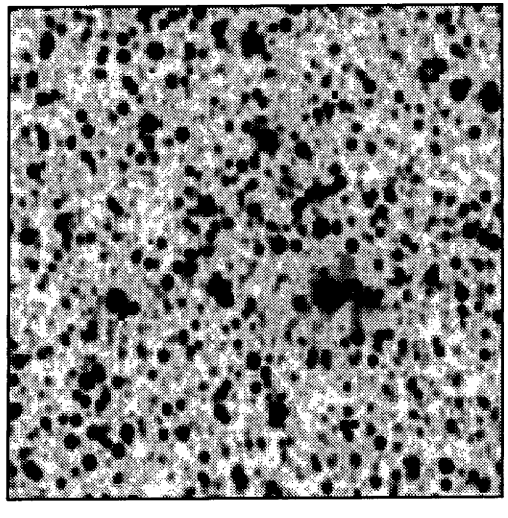

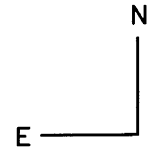

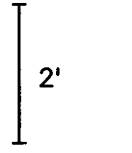

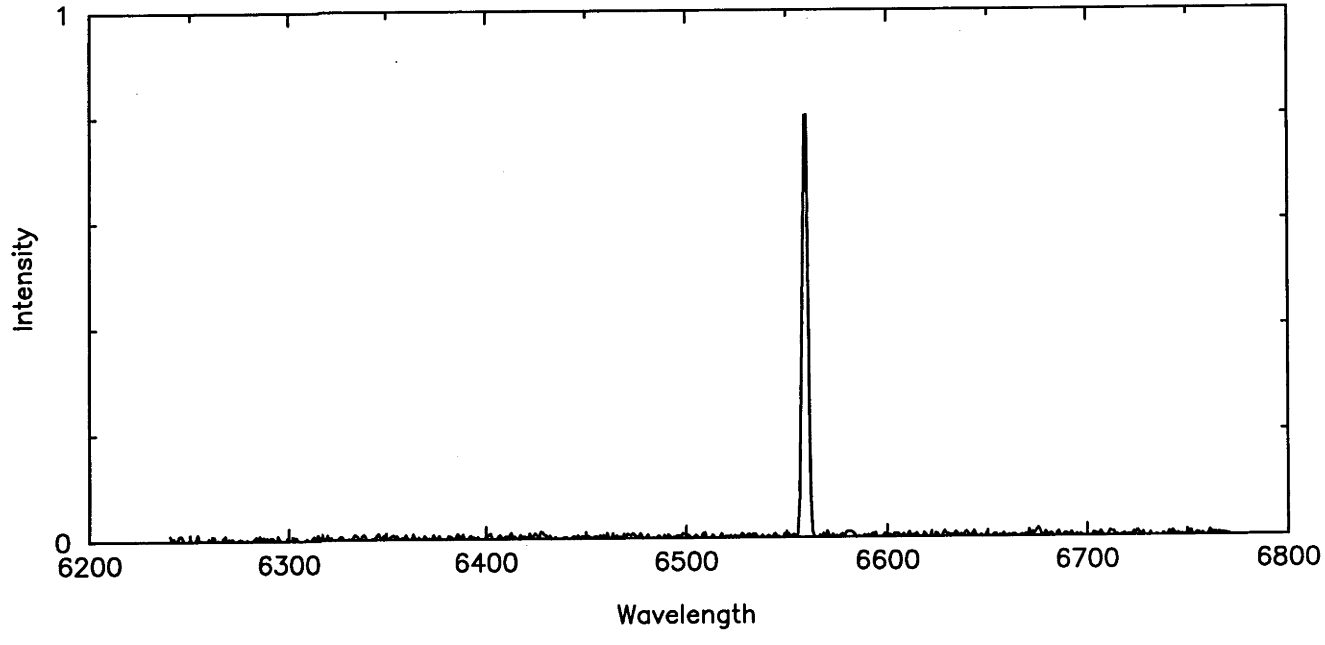

PN G352.0−06.7

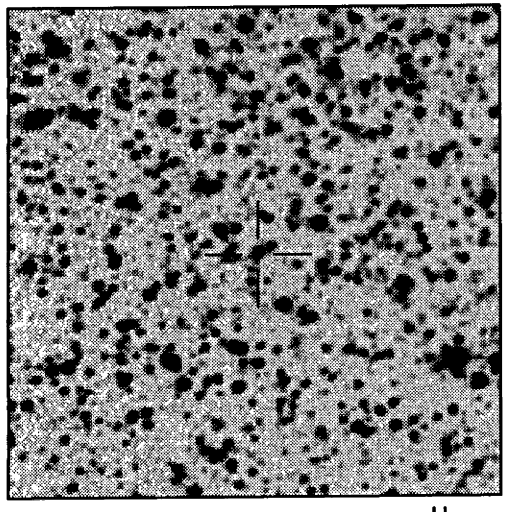

H_α

Cont

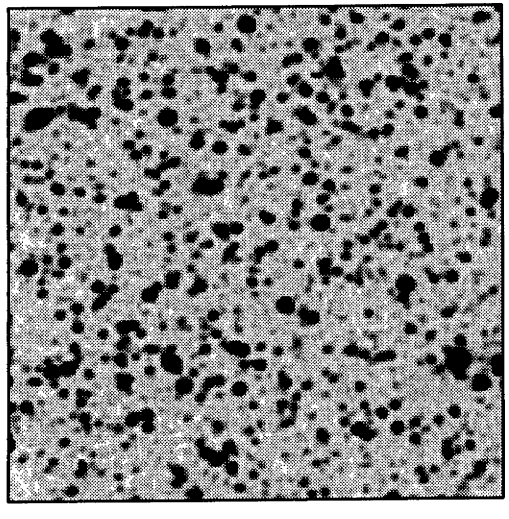

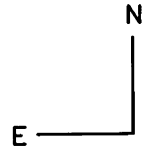

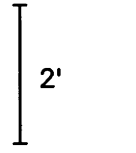

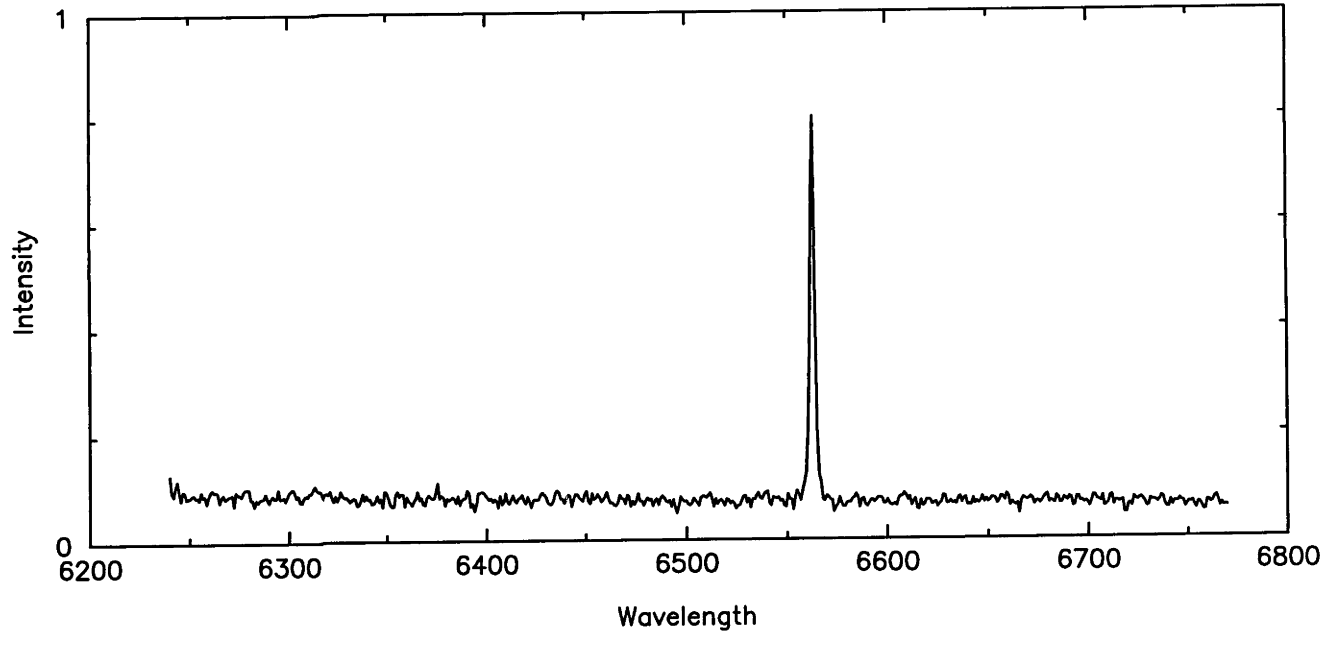

PN G352.6−04.9

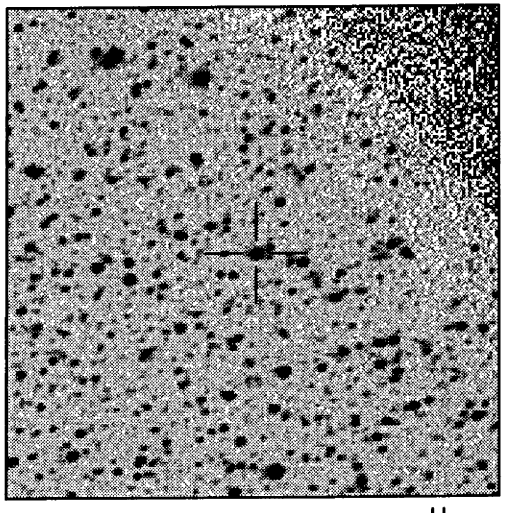

H_α

Cont

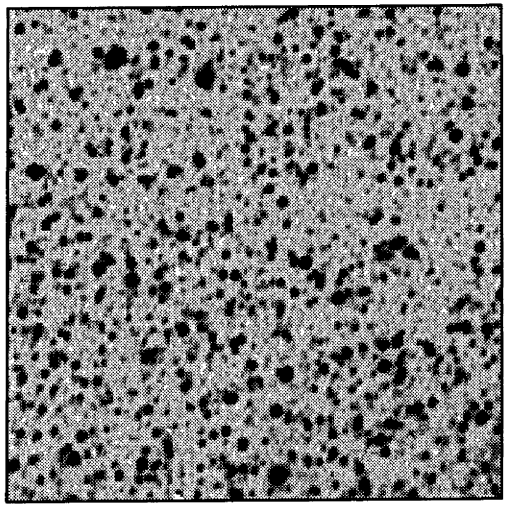

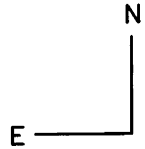

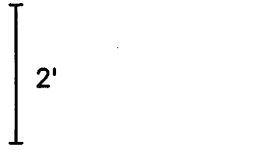

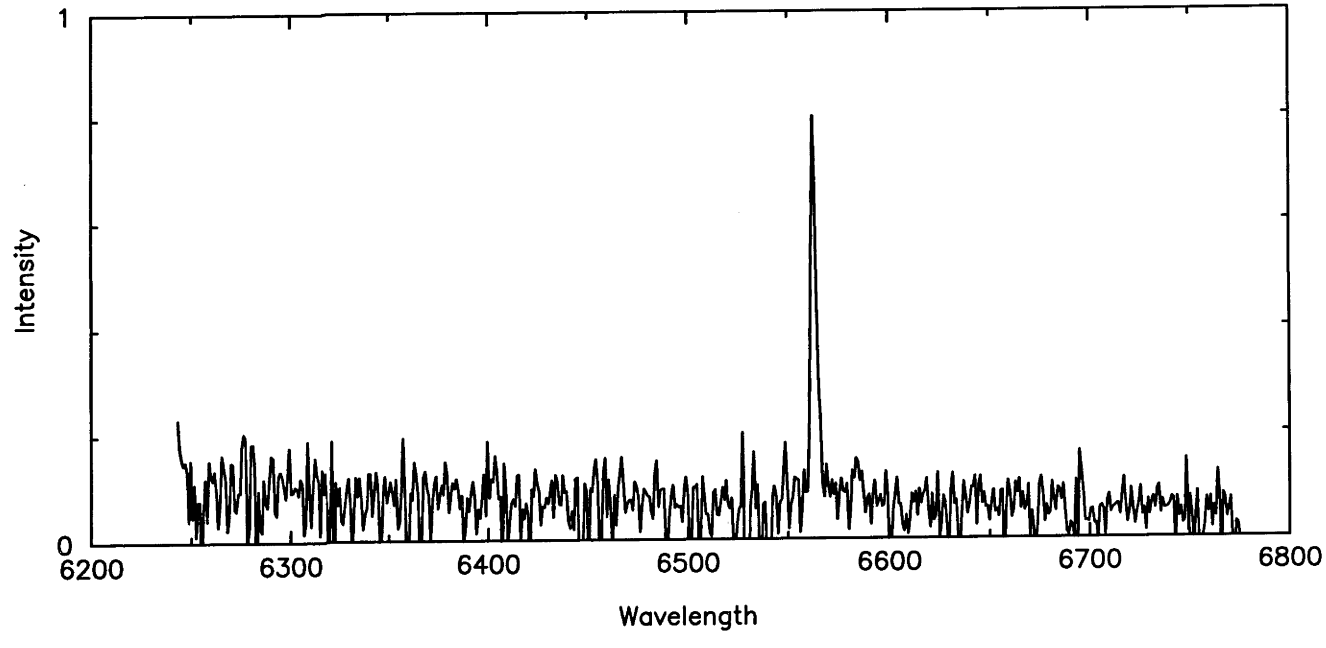

PN G352.7−08.4

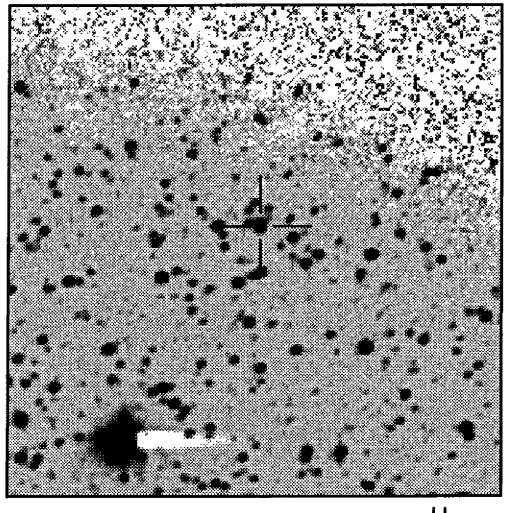

H_α

Cont

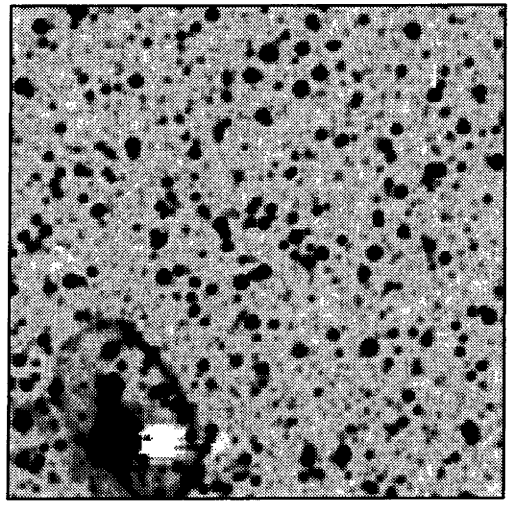

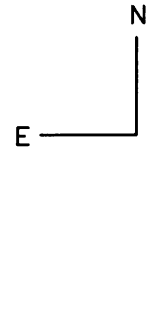

2'

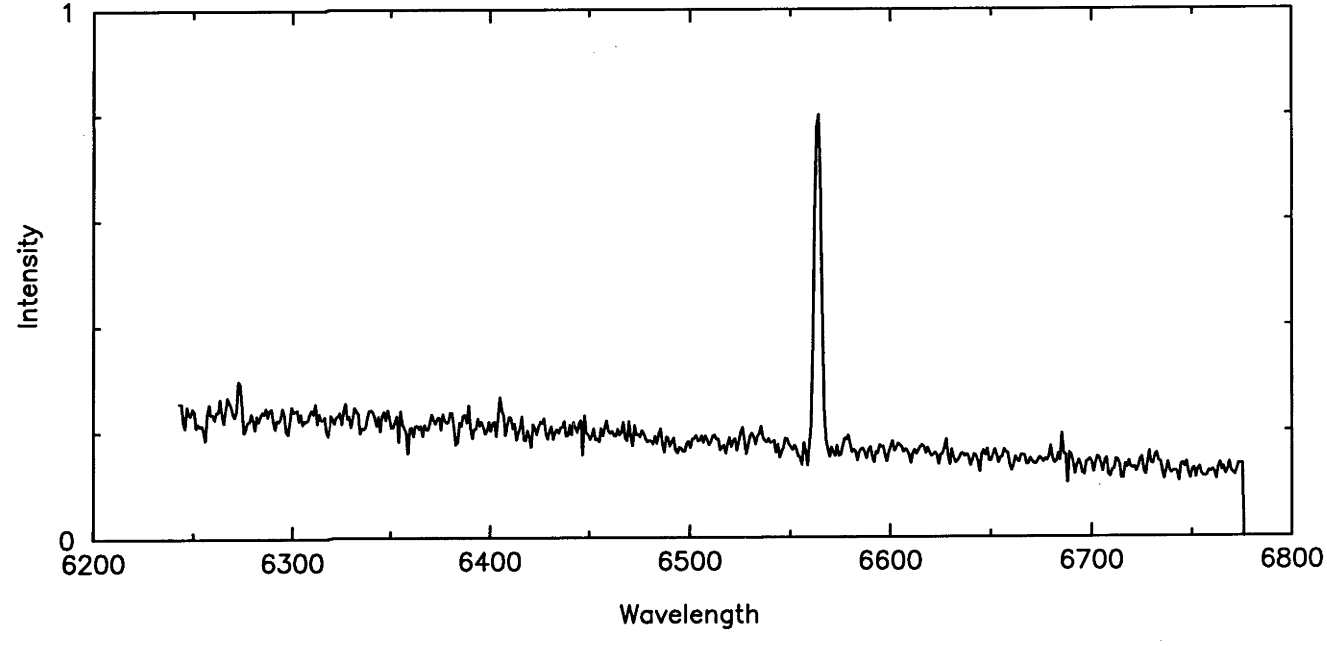

PN G353.3−08.3

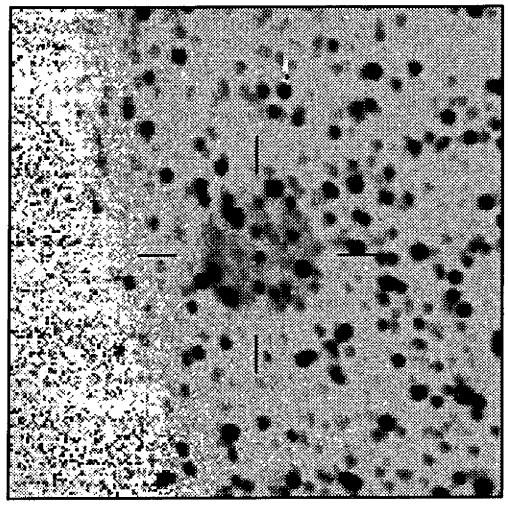

H_α

Cont

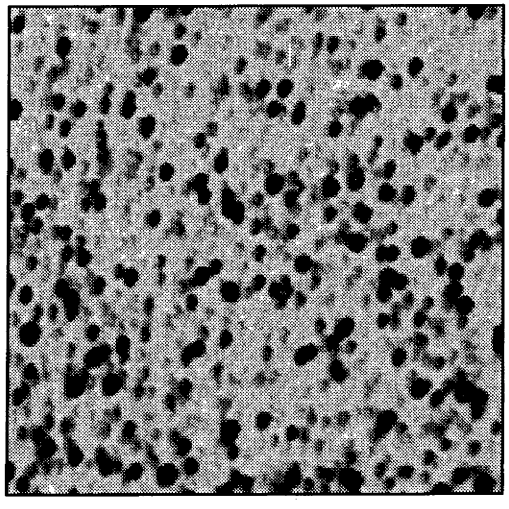

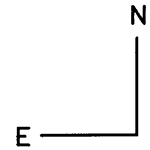

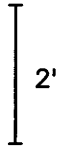

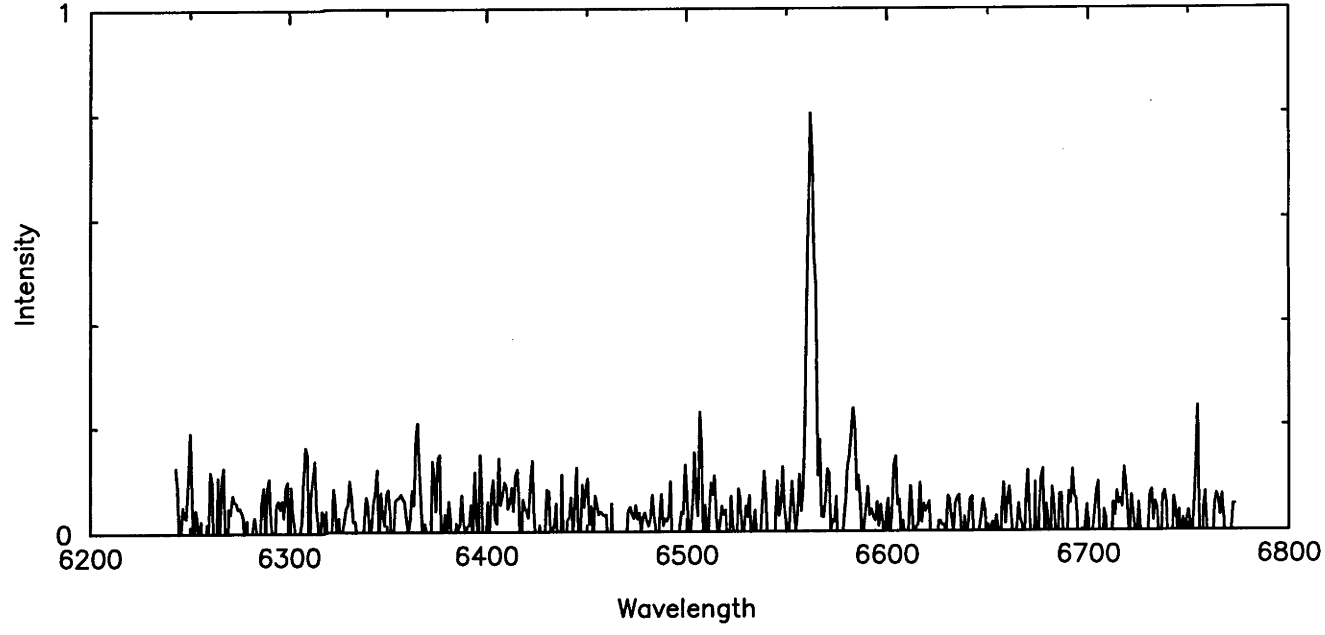

PN G354.7−07.2

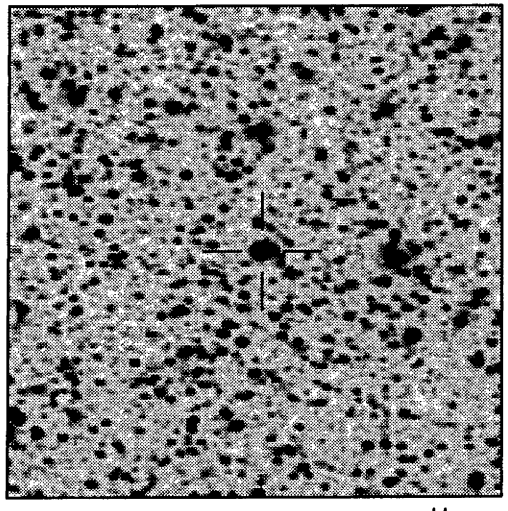

H_α

Cont

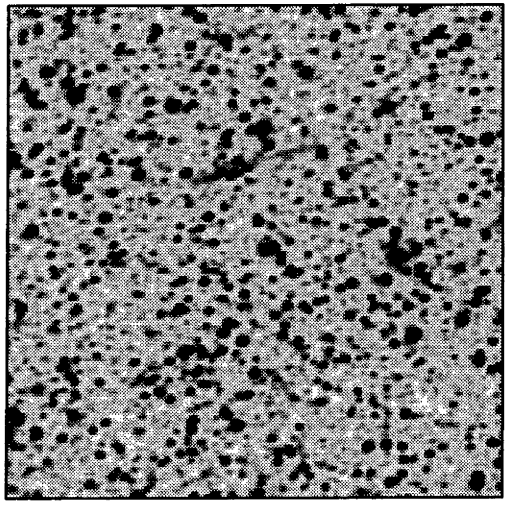

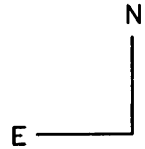

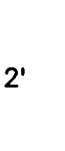

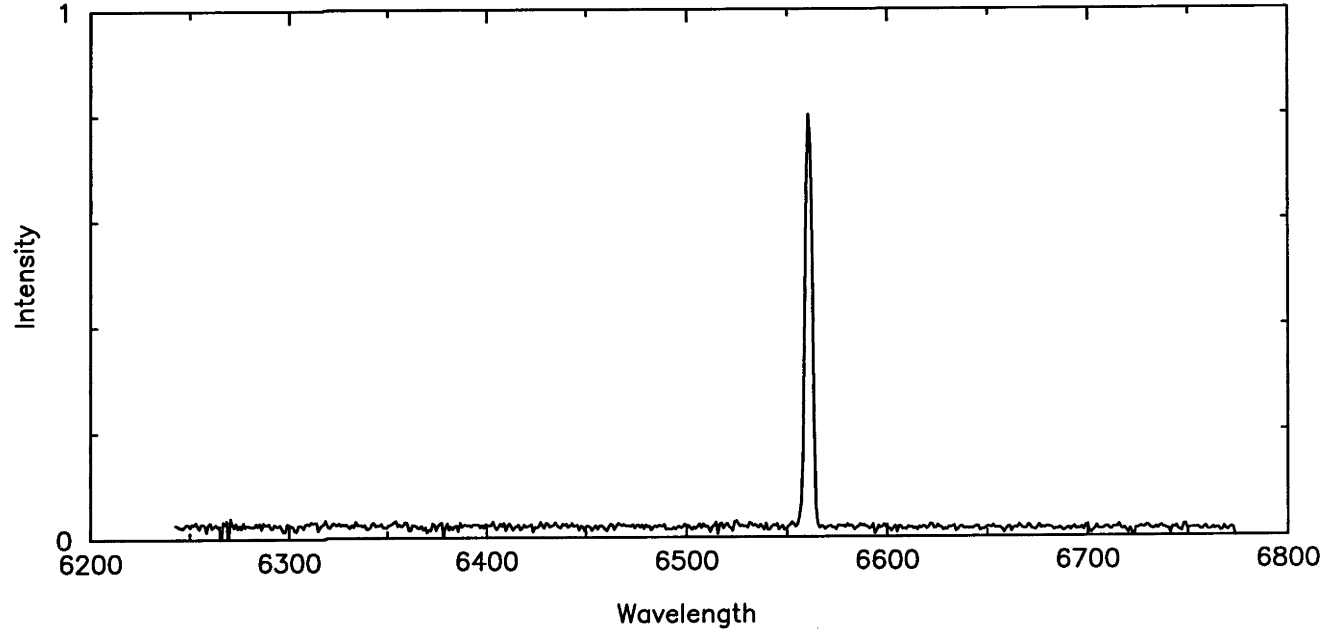

PN G354.7−10.0

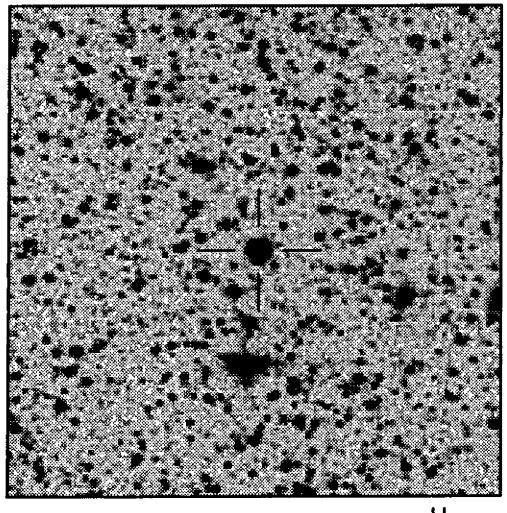

H_α

Cont

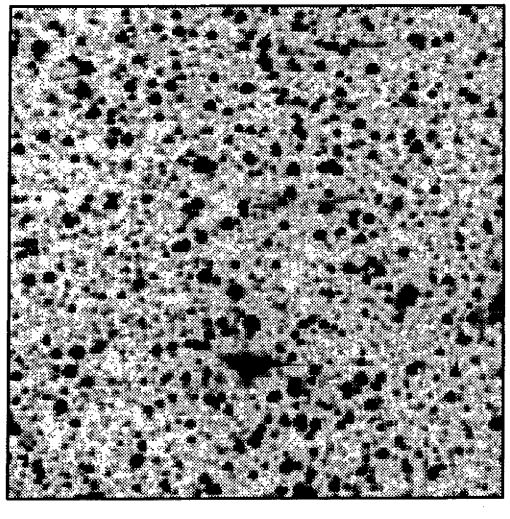

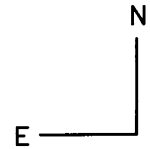

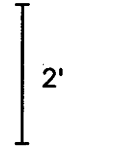

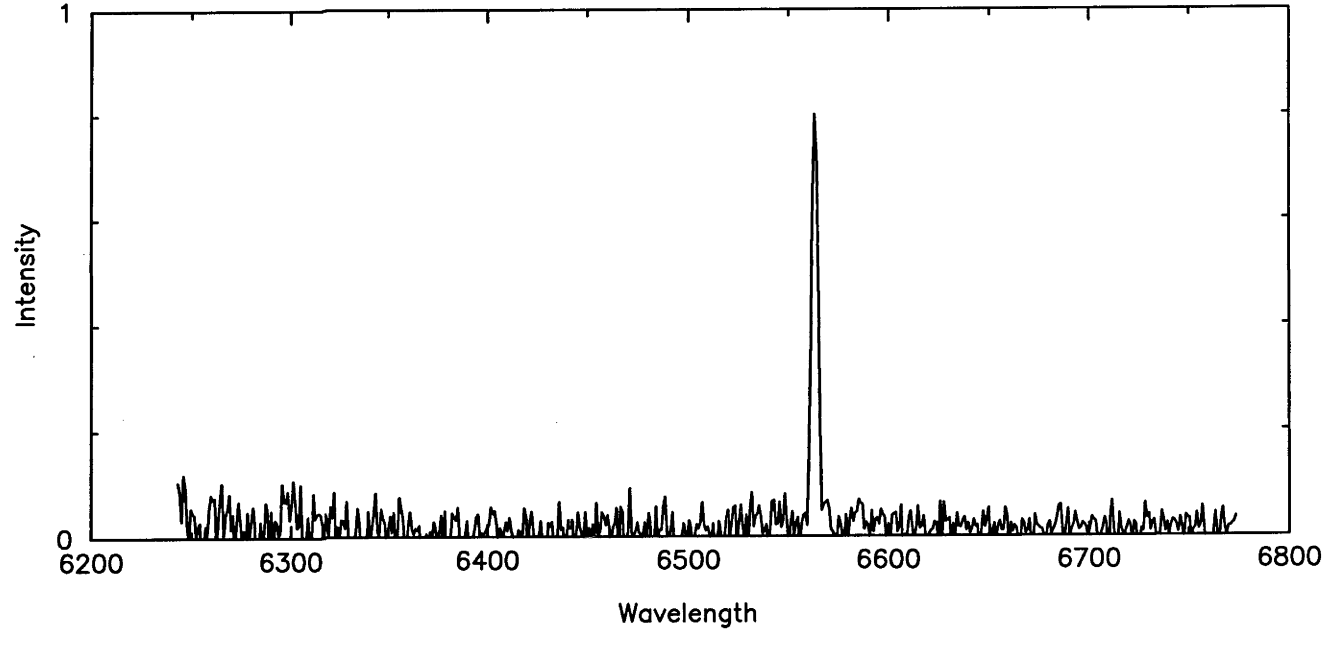

PN G355.3−07.5

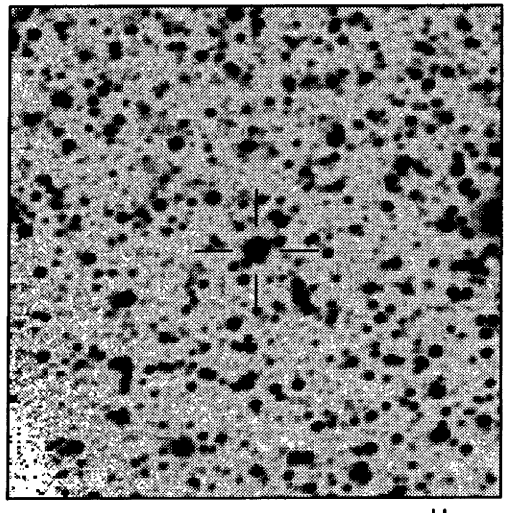

H_α

Cont

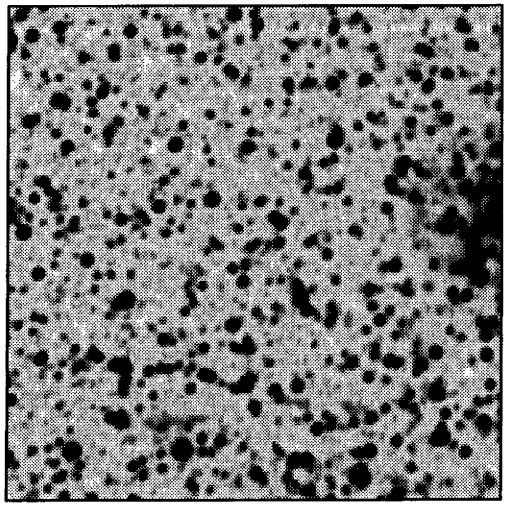

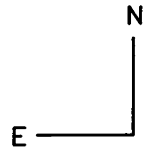

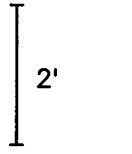

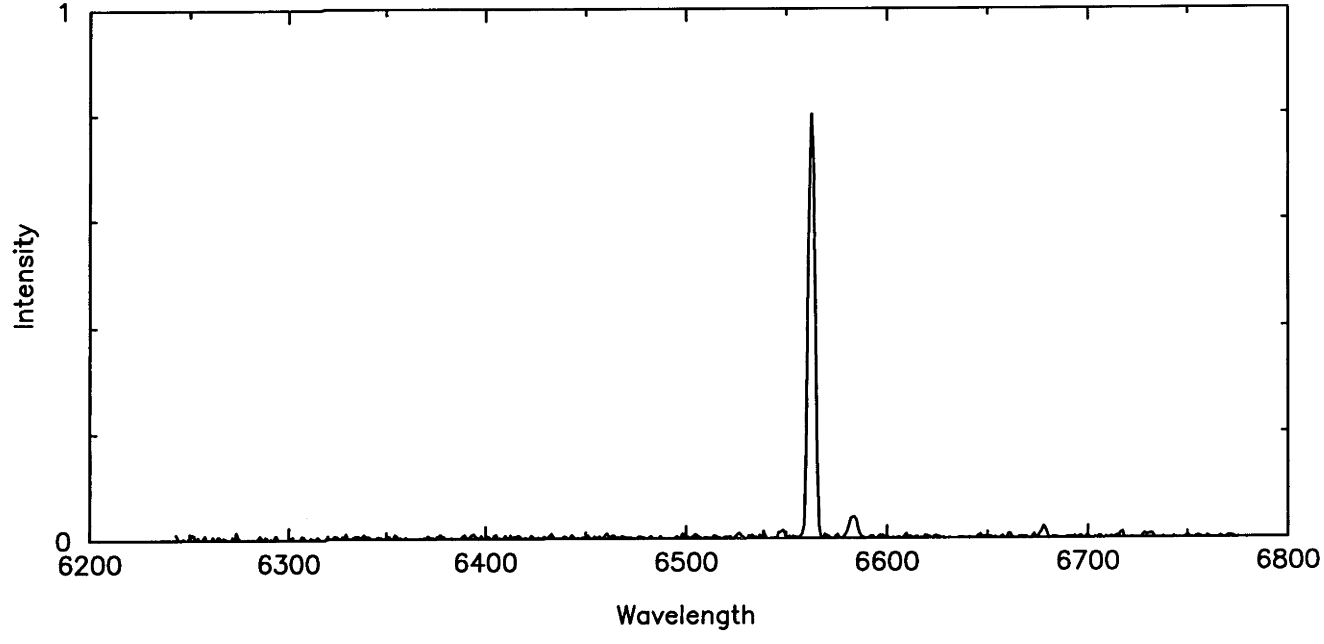

PN G355.8−08.7

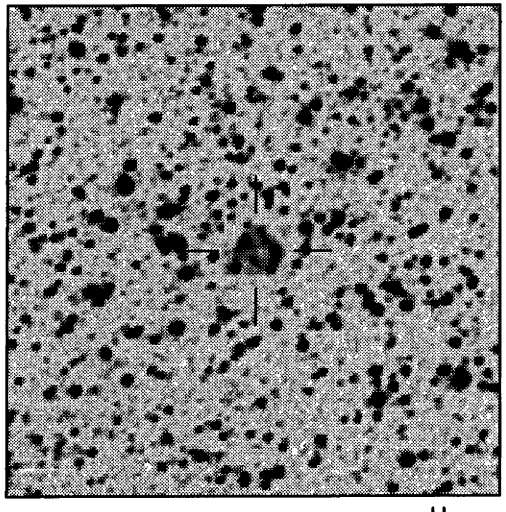

H_α

Cont

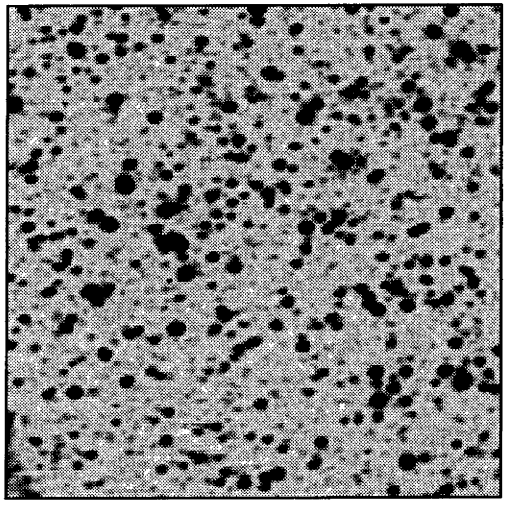

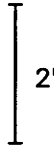

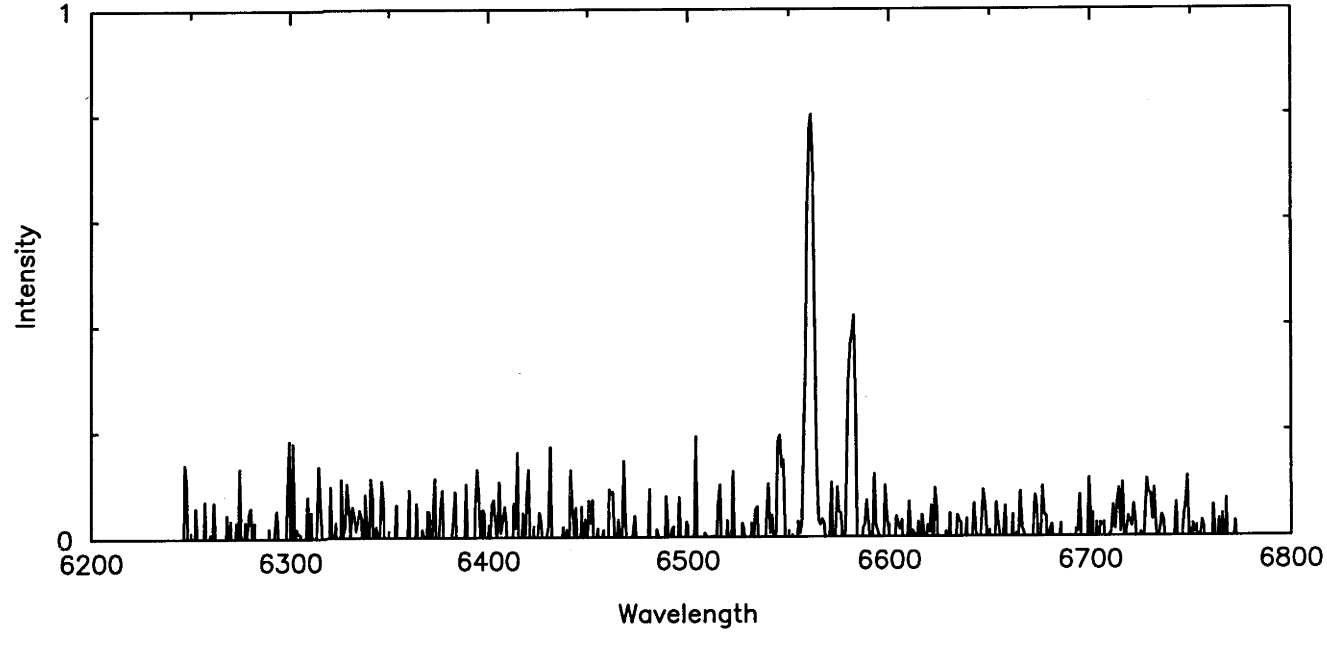

PN G356.0−07.4A

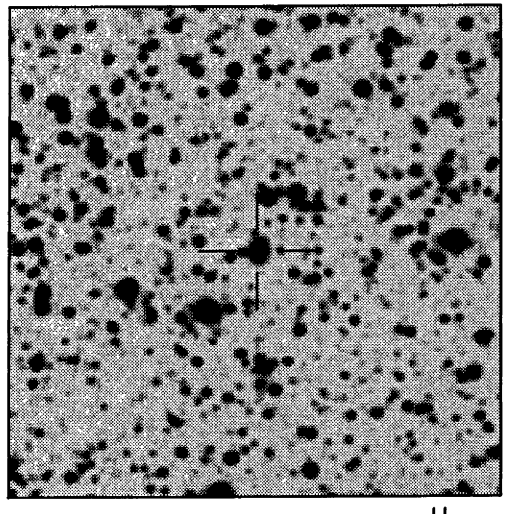

H_α

Cont

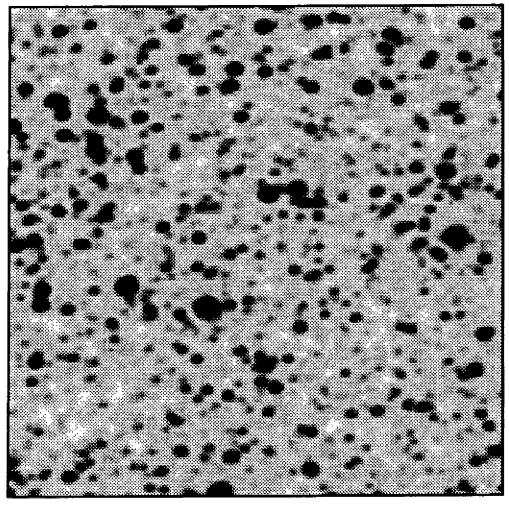

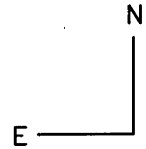

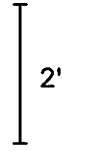

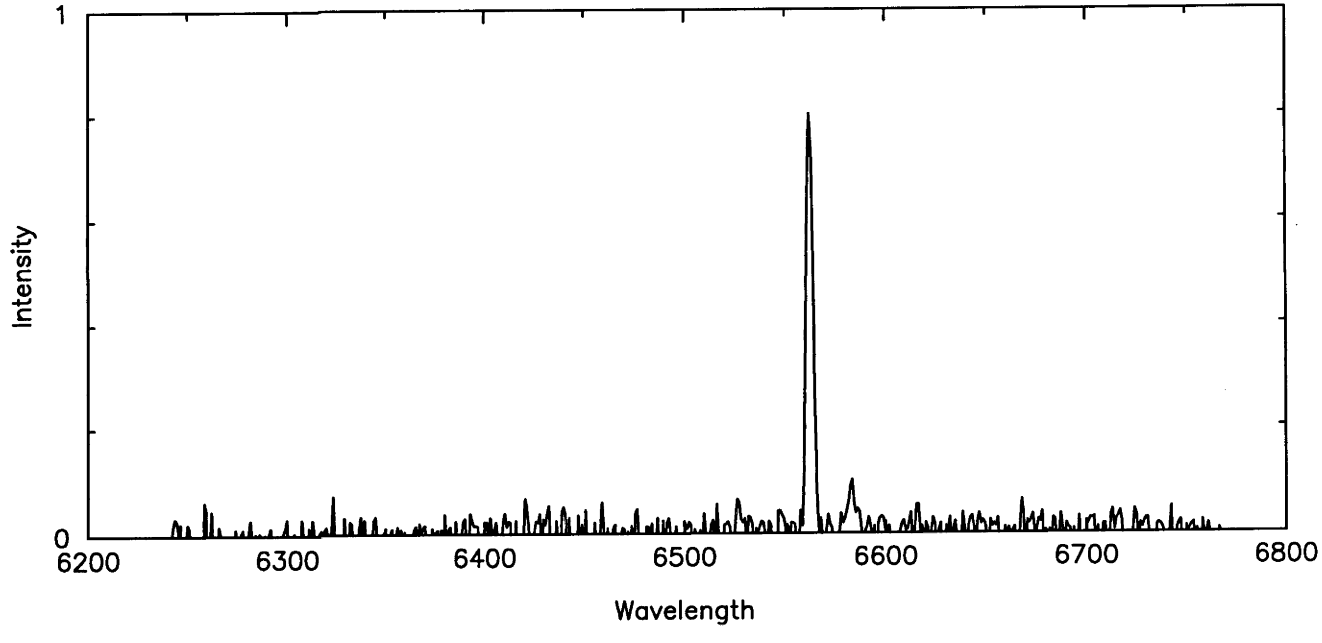

PN G356.0−07.4B

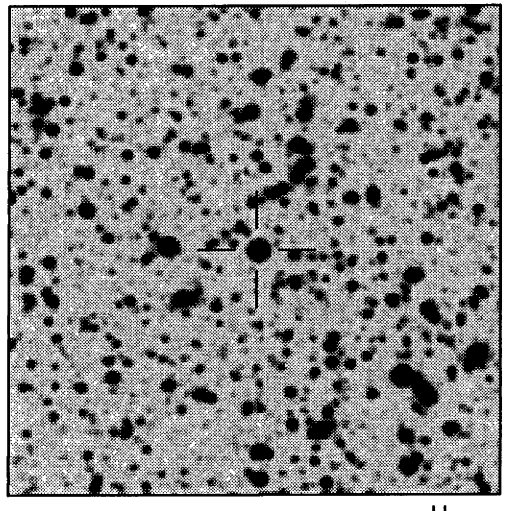

H_α

Cont

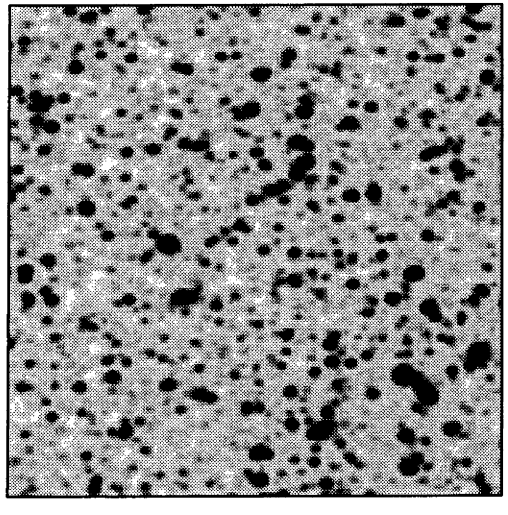

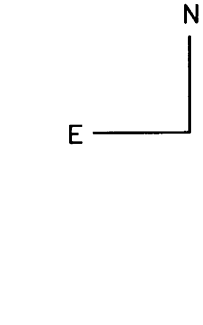

2'

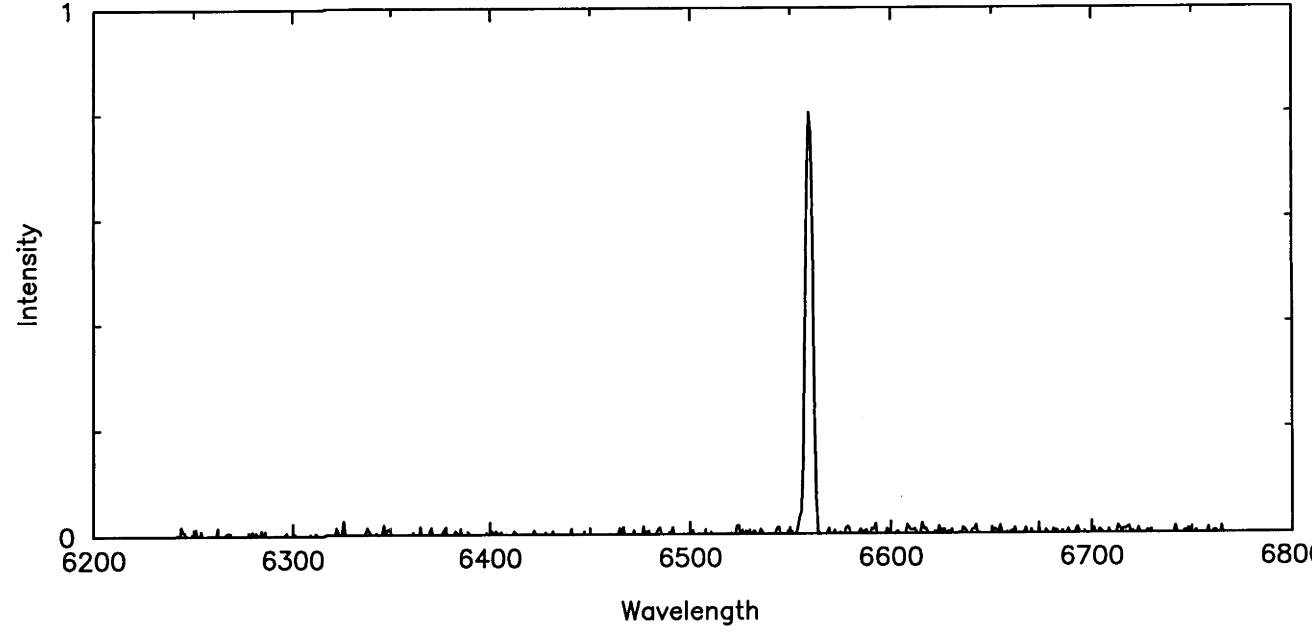

PN G356.1−08.6

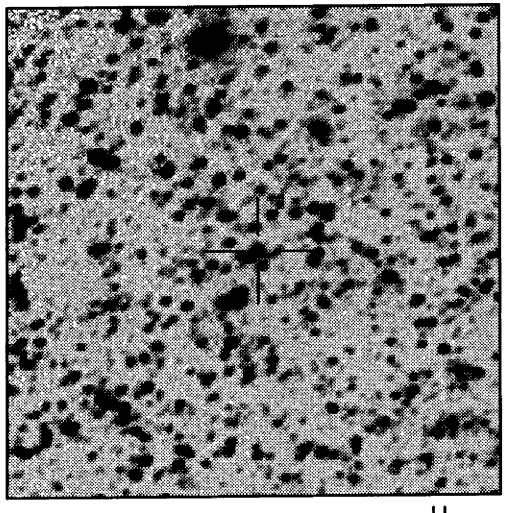

H_α

Cont